

GCC ER-80157

N66-10879

FEASIBILITY STUDY FOR AN
X-RAY BACKSCATTER AIR DENSITY SENSOR


8 April 1964

Prepared for
INSTRUMENT RESEARCH DIVISION
LANGLEY RESEARCH CENTER
NATIONAL AERONAUTICS AND SPACE ADMINISTRATION

Prepared under Contract NAS1-2306
by D. Hakewessell

GIANNINI CONTROLS CORPORATION
Control/Nucleonics Division
Duarte, California

Distribution of this report is provided in the interest of
information exchange. Responsibility for the contents
resides in the author or organization that prepared it.



Giannini Controls Corporation

GCC ER-80157

FEASIBILITY STUDY FOR AN
X-RAY BACKSCATTER AIR DENSITY SENSOR

8 April 1964

NAS 1-2306

FINAL Report

Prepared for
INSTRUMENT RESEARCH DIVISION
LANGLEY RESEARCH CENTER
NATIONAL AERONAUTICS AND SPACE ADMINISTRATION

Prepared under Contract NAS1-2306
by D. Hakewessell

GIANNINI CONTROLS CORPORATION
CONTROL/NUCLEONICS DIVISION
Duarte, California



FOREWORD


This report was prepared by Giannini Controls Corporation, Control/Nucleonics Division, Duarte, California on NASA Contract NAS1-2306, "Contract for Feasibility Study for an Air Density Sensor". The work was administered under the direction of the Instrument Research Division of Langley Research Center. Henry G. Reichle, Jr. and William D. Mace directed the project for the NASA.

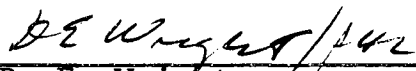
The studies presented began in October 1962, and were concluded in April 1964 and represent the joint effort of the Energy Management Group and Design Engineering Group of the Control/Nucleonics Division of Giannini Controls Corporation. Program Director, Energy Management Systems, D. B. Hakewessell, was responsible for the program and technical direction of work performed under this contract.


Major contributors to the effort at Giannini Controls Corporation were: D. E. Wright, Manager of Program Management and Systems Engineering;; E. Peterson, Electronic Design Engineer; S. Pontrelli, Mechanical Design Engineer; J. Brabec, Technician; and A. W. Conow, Supervisor of Radioisotope Laboratory.

Considerable assistance was obtained from Langley Research Center personnel in the design and flight testing of an experimental sensor. Major contributors were: J. Pride, C. Drummond, R. Kurtz, and R. Sherrill of FVSD; R. Reinhardt of AMPD; C. Laird R. Nelms, E. Clark, and H. Poole of IRD; and W. Brence and R. Long of Wallops Station. The cooperation of these people as well as many others particularly in the Mechanical Services Division was greatly appreciated.

This report has been reviewed and is approved by:


D. B. Hakewessell
Program Director
Energy Management Systems


D. E. Wright
Manager, Program Management
and Systems Engineering


R. W. Honebrink
General Manager,
Control/Nucleonics Division

ABSTRACT

10879

The study reported in this document pertains to the feasibility study for, and subsequent flight test of a free air density sensor suitable for use on vehicles operating at velocities up to 24,000 feet per second at altitudes up to 300,000 feet. The sensor operates on the principal that the intensity of backscattered X-radiation is related to the density of the free air being measured.

A handwritten signature, possibly reading "D. H. K.", is written in the bottom right corner of the page.

TABLE OF CONTENTS

	<u>Page</u>
1.0 INTRODUCTION	1
2.0 SENSOR TECHNICAL DESCRIPTION	2
3.0 SENSOR DESIGN & OPERATION	6
3.1 Theory	6
3.2 Component Description	10
3.3 Structural Design	39
3.4 Electrical Assembly	40
3.5 Calibration Procedure	40
4.0 PERFORMANCE	44
4.1 Calibration	44
4.2 Environmental Testing	50
4.3 Flight Test	54
4.4 System Accuracy	67
5.0 SOURCE HANDLING ASPECTS	76
6.0 GROWTH POTENTIAL	78
6.1 Further Radioisotope Flights	78
6.2 Flights Using X-Ray Tube as Source	78
7.0 APPLICABLE DOCUMENTS	
APPENDIX I STRUCTURAL & ENVIRONMENTAL DESIGN REQUIREMENTS	I-1
APPENDIX II GAMMA SCATTERING CLASSICAL THEORY	II-1
APPENDIX III PAYLOAD FLIGHT READINESS TEST DATA	III-1
APPENDIX IV FLIGHT DATA	IV-1

LIST OF ILLUSTRATIONS

		<u>Page</u>
Figure 1	AIR DENSITY SENSOR ASSEMBLY	3
Figure 2	BLOCK DIAGRAM AIR DENSITY SENSOR	4
Figure 3	SENSOR SCATTERING GEOMETRY	7
Figure 4	SOURCE CONFIGURATION	11
Figure 5	DECAY SCHEME CERIUM 144, PRASEODYMIUM-144	12
Figure 6	CERIUM 144 ENERGY SPECTRUM	13
Figure 7	SOURCE AZIMUTH RADIATION PATTERN	15
Figure 8	SOURCE ELEVATION RADIATION PATTERN	16
Figure 9	DETECTOR ASSEMBLY	20
Figure 10	MULTIPLIER PHOTOTUBE SCHEMATIC	21
Figure 11	PHOTOTUBE NOISE REFERRED TO MEASUREMENT PARAMETERS	22
Figure 12	DETECTOR AZIMUTH SENSITIVITY PATTERN	24
Figure 13	DETECTOR ELEVATION SENSITIVITY PATTERN	25
Figure 14	AMPLIFIER & LEVEL SELECTOR	26
Figure 15	MODULE, WELDED	27
Figure 16	MODULE, WELDED	28
Figure 17	PULSE SHAPER	29
Figure 18	EXPECTED COUNT RATES	30
Figure 19	SCHEMATIC - TEMPERATURE SENSORS & REFERENCE VOLTAGES	33
Figure 20	BATTERY PACK LIFE	35

LIST OF ILLUSTRATIONS (cont.)

		<u>Page</u>
Figure 21	POWER SUPPLY ASSEMBLY	36
Figure 22	PORTABLE TEST SET SCHEMATIC	37
Figure 23	PORTABLE TEST INSTRUMENT	38
Figure 24	ANTICIPATED & ACTUAL TEMPERATURE RISE OF INTERNAL PAYLOAD AT VARIOUS STATIONS	41
Figure 25	ADS-102 WIRING DIAGRAM	42
Figure 26	SENSOR RESPONSE TO DIRECT TRANSMISSION	45
Figure 27	SENSOR DENSITY CALIBRATION IN ALTITUDE SPHERE	47
Figure 28	SENSOR SCALE FACTOR SHIFT DUE TO TELEMETER RF	48
Figure 29	CERIUM-144 ENERGY SPECTRUM	49
Figure 30	THERMISTOR TEMPERATURE SENSOR CALIBRATION	51
Figure 31	TEST VOLTAGE CALIBRATION TELEMETER CHANNEL	52
Figure 32	NIKE-APACHE ON LAUNCHER	55
Figure 33	AIR DENSITY SENSOR FLIGHT UNIT	56
Figure 34	AIR DENSITY SENSOR FLIGHT UNIT	57
Figure 35	DUMMY SOURCE	58
Figure 36	AUXILIARY TELEMETER DATA	60
Figure 37	TELEMETRY COUNT DATA PLOTTED AS A FUNCTION OF ALTITUDE	61
Figure 38	AIR SCATTER DATA, DETECTOR #1	63
Figure 39	AIR SCATTER DATA, DETECTOR #2	64
Figure 40	AIR SCATTER DATA, DETECTOR #1	65

LIST OF ILLUSTRATIONS (cont.)

		<u>Page</u>
Figure 41	AIR SCATTER DATA, DETECTOR #2	66
Figure 42	METEOROLOGICAL SOUNDING DATA	68
Figure 43	METEOROLOGICAL SOUNDING DATA	69
Figure 44	INTEGRAL SPECTRUM, COSMIC BACK- GROUND DATA	71
Figure 45	AIR SCATTER DATA	75

LIST OF TABLES

		<u>Page</u>
Table I	TELEMETRY REQUIREMENTS	32
Table II	ENVIRONMENTAL TESTING SUMMARY	53

1.0 INTRODUCTION

This report discusses the theoretical and experimental work performed in the feasibility study for, and subsequent flight tests of a free air density sensor, operating on the principle that the amount of backscattered X-radiation is related to air density. This work was sponsored by the Instrument Research Division, Langley Research Center, National Aeronautics and Space Administration.

The program included a literature survey and analytical studies relating to the basic feasibility, experimental work to obtain basic design data and verify the theoretical analyses, development of a sensor suitable for flight on the Nike-Apache boost system, flight test of the sensor, analyses of the flight data, and studies relating the measurement to other flight vehicles.

The notable results of this program were to verify on an experimental basis the sensor concept using practical hardware. Techniques of handling the high strength radioisotope source were developed. Flight hardware was developed capable of providing the density measurement under the extreme environments imposed by the launch vehicle. Electronics were designed and packaged to provide signal conditioning of the sensor outputs. A telemetry system was designed, and data processing methods established to complete a data acquisition and reduction system for the measurement of atmospheric density at high altitudes from high velocity vehicles.

These results have laid the groundwork for an advanced sensor utilizing an X-ray tube as the source of radiation, reducing the safety and handling procedures necessary with the radioisotope source, and increasing the altitude capability of the measurement.

2.0 SENSOR TECHNICAL DESCRIPTION

The sensor package developed in this program is illustrated in Figure 1. The system design is illustrated in the block diagram of Figure 2. Low energy gamma radiation, 134 Kev, emanating from the Cerium-144 radioisotope source is scattered by the air surrounding the vehicle into detectors 1 and 2. The amount of radiation scattered into the detectors is proportional to the air density. Direct transmission of the radiation from the source to the detectors is eliminated by a lead shield. The purpose of the dual detector arrangement is to provide measurements at high altitudes where cosmic background constitutes a large portion of the detected radiation. The radiation from one side of the source is attenuated by a small tungsten shield oriented such that detector 2 senses only a small portion of the air scattered radiation. Under these conditions detector 2 is measuring primarily the cosmic background. This measured background level is subtracted from detector 1 in the data reduction process to provide the air scatter measurement of density. At low altitudes the scattered signal is high and background can be neglected.

The detectors transform the impinging radiation into electrical pulses proportional to the energy deposited by gamma photons. These electrical pulses are selected on a pulse height basis by the discriminators. Signals below the base level representing background and noise are rejected and pulses above the inhibit level representing high energy background are rejected. Those pulses falling within the desired window are shaped and passed on to a series of flip-flops.

The flip-flops divide the pulse rate to a rate capable of being telemetered to the ground station. The flip-flop outputs are shaped by the pulse shapers to provide the proper signals for modulating the subcarrier oscillators of the telemetry system.

These pulses are transmitted via the FM-FM telemetry system to the ground station where they are received and recorded. The pulse rate as a function of time is compared with the altitude versus time profile acquired from tracking radar data to provide the measure of density as a function of altitude. Additional data measured and transmitted to the ground are:

1.

OTA
ZERO

OTA
7.75

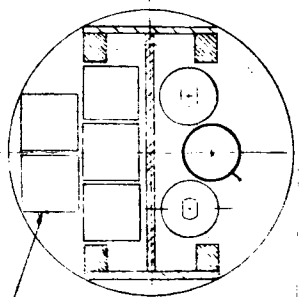
OTA
7.610

DETECTOR ASSY X3042560
CAP SCREW MS 4990-10 10-32
1 REQ WASHER X 108000176 10-32
WASHER PLAT MS 5795-303 1/4

NEOPRENE CUSHION 1/8 THK

RADIATION SHIELD
SN 13-1374-72

LEAD SHIELD

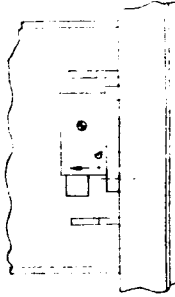
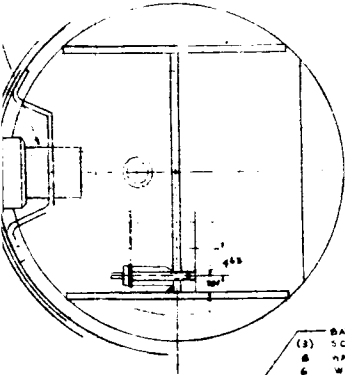


X3041840 MODULE 1/2 INCH
X3041840 MODULE 1/2 INCH
X3041840 MODULE PULSE SHAPER 5/8
SCREW MS 55223-10 2 5/16 1/2 10-32
WASHER PLAT MS 5745-303 1/4
1/4 INCH 10-32 THD 100 1.000 DEEP
DO NOT BREAK THRU

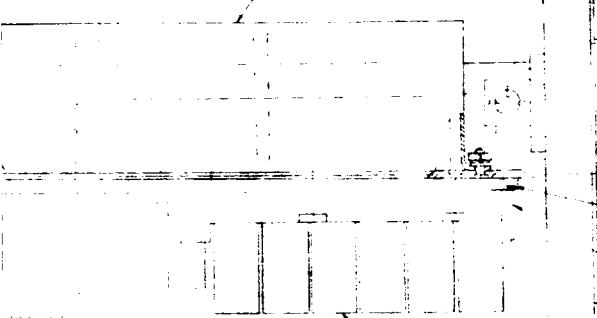
FD
500

3.

MS 4995-2 CAPSCREW 2-56 X 1/2 - 2 PLACES
 MS 5195-302 WASHER LOCK #2 - 3 PLACES
 MS 5195-303 WASHER LOCK #2 - 3 PLACES



BATTERY PACK X3041857
 (2) SCREW CAP MS1875-307 #4
 6 WASHER LOCK MS55537-80 #5
 (3) NUT NER MS38647-84 #5



X3041867 INSULATOR

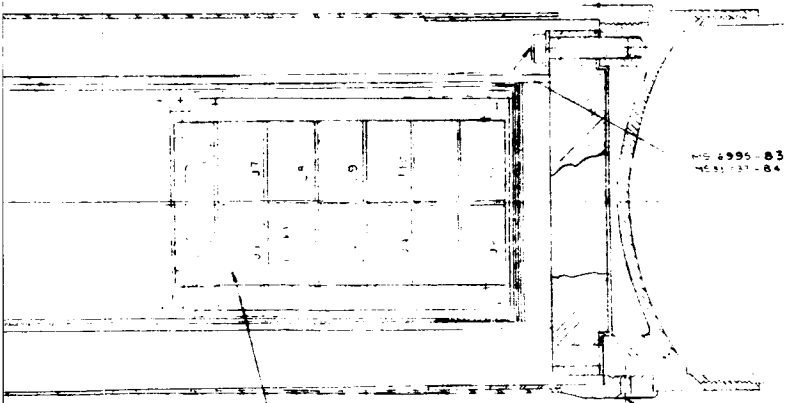
4 X 4 WICKER SP GASKET

X3041856 RF COVER
 4 X 4 WICKER SP GASKET
 MS 5175-303 WASHER LOCK #2 - 3 PLACES
 MS 5175-302 WASHER LOCK #2 - 3 PLACES
 STA 580

ORSA TRANSMITTER
 MS100-4 ATTACHMENT
 IS. 8-31 X 3/4
 TSHIR
 CREW 8 3/2 X 1/2
 WASHER FLAT
 WASHER LOCK

X3041857 CONN MS37
 TJS 512 CONN MS37
 TOL 308 OSCILLATOR CO. RECD
 MS 5175-303 WASHER LOCK #2 - 3 PLACES
 MS 5175-302 WASHER LOCK #2 - 3 PLACES

STA 57115



MS 4995-83 SCREW CAP 2-56 X 1/2
 MS 5175-303 WASHER LOCK #2 - 3 PLACES

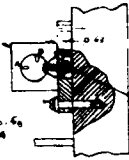
TAG 305 AMPLIFIER

2.750R

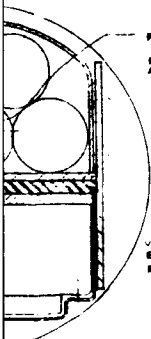
ACCELEROMETER
 (DIAGN.) 24195

FEED THRU LERCO 6084
 OR EQUIV 2.4600
 LOCATION OFF IN THIS
 AREA

INSULATOR X3041848 -
 SCREW MS55537-80 #5
 4 PLACES
 WASHER LOCK MS55537-80 #5
 WASHER FLAT MS1875-307



MS 4995-2 CAPSCREW 2-56 X 1/2
 MS 5175-303 WASHER LOCK #2 - 3 PLACES
 MS 5175-302 WASHER LOCK #2 - 3 PLACES

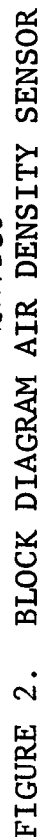


VIEW LOOKING AFT SHOWING
 BATTERY PACK TRANSMITTER
 RF COVER 5 GASKET

REVISIONS		DATE	APPROVAL
	DESCRIPTION		
X1	FIRST ISSUE MIL-STD-883 WAS MISLabeled TO (GARY)	5-6-68 7-1-68	John
X2	DESIGN CHECK PER DATA REQUEST, SEE DATA DWG 80494, FOR PREVIOUS CHANGES SEE RECD BOWLING	3-10-68 3-11-68	John

X3041810 X2

QTY	REQD	SYS.	NOMENCLATURE OR DESCRIPTION	CONE CODE	PART OR IDENTIFYING NO.	SPECIFICATIONS	MATERIAL OR SIZE	UNIT REQD	TOTAL REQD
LIST OF MATERIAL									
UNLESS OTHERWISE SPECIFIED									
ALL DIMENSIONS ARE IN INCHES DO NOT SCALE DRAWINGS PART TO BE FREE OF BURRS RINSE SHARP EDGES ALL THREADS PER MIL-S-778			DRAWN <i>[Signature]</i>		<i>[Initials]</i>				
			CHECKED <i>[Signature]</i>						
			APPR. <i>[Signature]</i>						
			DATE 9/1/69						
TOR .X2 = .XXX = ANG 9									
SURFACE REQUIREMENTS PER MIL-D-1170 ✓									
MATERIAL									
NEXT REV USED ON APPLICATION			APPROVAL		AIR DENSITY SENSOR				
			APPROVAL		CONE HEAD NO. 14905				
					SIZE X3041810 X2				
					SCALE 1/1				
					UNIT				
					PRINT				



- 1) longitudinal acceleration
- 2) power supply voltages
- 3) temperature of the payload base
- 4) temperature of the transmitter heat sink
- 5) temperature of the discriminators
- 6) temperature of the power supply

An accelerometer provides the acceleration data and thermistors provide temperature data.

Power is supplied to the system by a 28-volt battery pack and DC-DC converter. Auxiliary ground power can be switched to the system through a set of ground interface relays and an umbilical connector. Several test signals are available through this interface for ground checkout of the system operation. The battery is also charged through this interface.

Details of the mechanical assembly of the payload are illustrated in Figure 1. The internal structure consists of four aluminum beam sections on which system components are mounted. The cylindrical section at Station 42 provides structural support and yet allows electrical clearance for antenna flanges. The detector assembly is attached to the forward end of the internal beam structure. The internal structure is bolted to the Apache head cap and is insulated thermally from the head cap by 1/16 inch thick silicone glass fiber insulation.

The external structure consists of an Inconel fuselage, a fiberglass nose cone containing the lead shield, and a stainless steel nose piece supporting the source. This whole assembly is threaded together and to the Apache head cap. A bearing support between the inner and outer structure is made by a close concentric fit at Station 37.

Alignment in roll between the various payload members is made at assembly of each individual payload. The threaded sections must be seated and the source, detector, umbilical, and fuselage aligned. To perform this, the umbilical mounting hole and source orientation fixture are located at assembly.

3.0 SENSOR DESIGN AND OPERATION

This section provides the theoretical basis and the structural and environmental requirements used in the design of the air density sensor flight package. The theory presented is based on data acquired by testing an experimental package in a large altitude sphere. The structural and environmental design requirements were provided by the Flight Vehicle and Systems Division at LRC, NASA. These requirements are presented in Appendix I.

3.1 Theory. Appendix II presents the basic theory relating the classical scattering equations to this application. It provides the scattering cross section of air as 1.2×10^{-2} cm²/gm/steradian for the photon energies of interest and provides a basis for the following simplifying assumptions.

(1) Scattering in this energy region is the result of interaction with electrons.

(2) The probability of scattering is approximately equal in all directions.

(3) Absorption is negligible in the scattering region.

Figure 3 illustrates the sensor scattering geometry for which theoretical estimates of the sensor sensitivity are derived. This derivation is given below.

Let:

I_o = source strength in photons per second emitted isotropically.

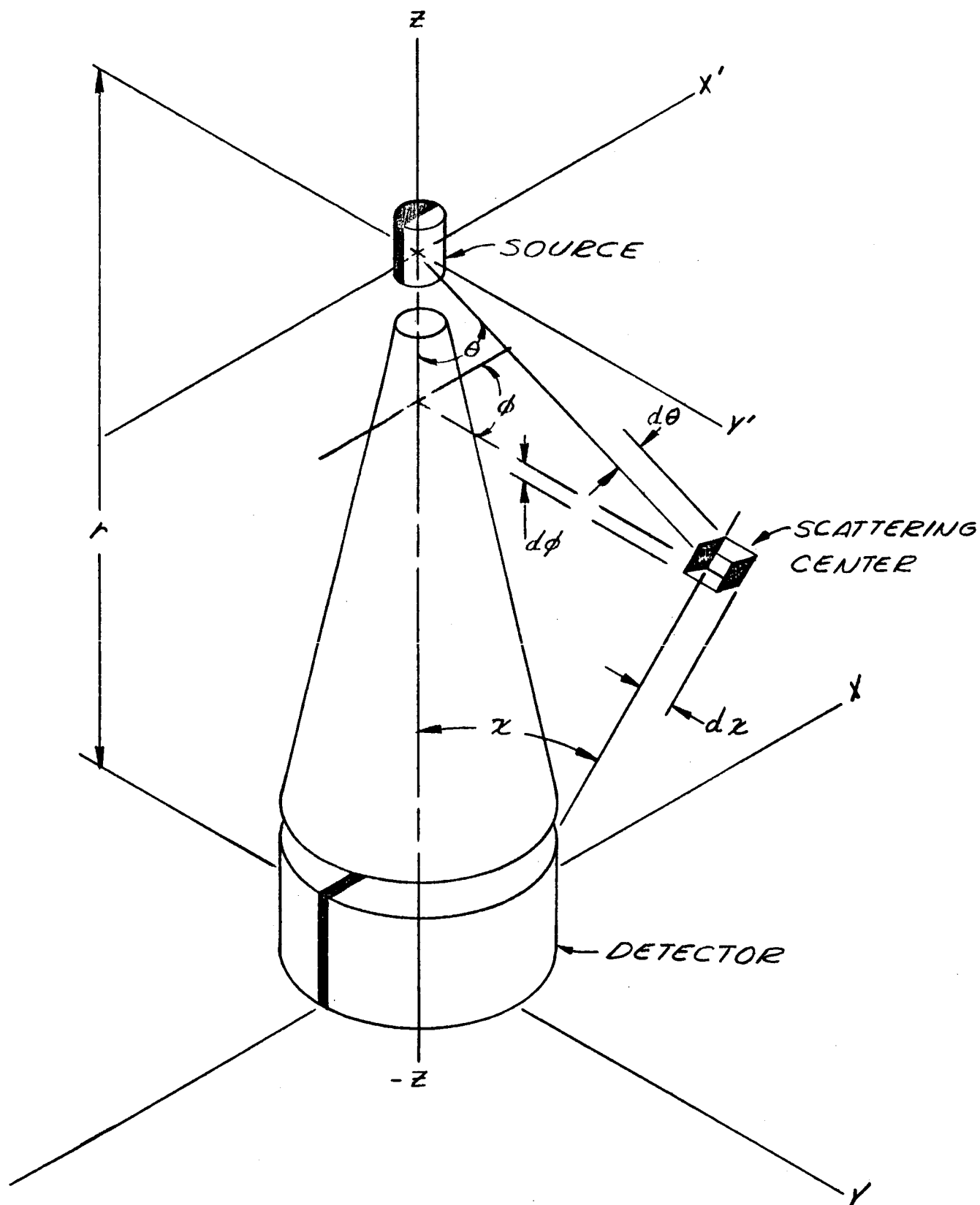
A_D = detector area presented normal to the y axis, cm²

r = source-detector separation, cm

K = scattering cross section for air, cm²/gm/steradian

ρ = air density, gm/cm³

θ = angle from the -Z axis to the line from source to scattering center



SENSOR SCATTERING GEOMETRY

FIGURE 3

ψ = angle from the +Z axis to the line from detector to scattering center

ϕ = angle about the Z axis to the scattering center measured from the X-Z plane

s = linear distance from source to scattering center

t = distance from detector to scattering center

The effect of shielding and self-absorption of the source acts to modify the source strength as a function of angle. This function is closely related to the surface area of the source presented at any angle. This gives a source strength as:

$$I_0 \sin \psi \frac{1 + \sin \phi}{2} \quad (1)$$

The detector sensitivity also is closely related to the surface area of the crystal presented to the scattering center. This gives a detector pattern as:

$$A_D \sin \psi \frac{1 + \sin \phi}{2} \quad (2)$$

for detector #1 and:

$$A_D \sin \psi \frac{1 - \sin \phi}{2} \quad (3)$$

for detector #2.

For the purpose of this analysis the scattering center can be considered a point source whose strength is the product of the flux passing through the scattering center and the scattering cross section of the scattering media.

The flux passing through the differential scattering center is:

$$I_0 \sin^2 \psi \frac{1 + \sin \phi}{2} d\psi d\phi \quad (4)$$

The equivalent source is thus this flux times the scattering cross section, density, and differential length or:

$$I_S = I_0 K \rho \sin^2 \theta \frac{(1 + \sin \phi)}{2} \frac{t d\gamma d\theta d\phi}{\sin(\theta + \gamma)} \quad (5)$$

The sensitivity of detector #1 to this equivalent source is:

$$I_{D1} = \frac{I_S A_D \sin \gamma}{4 \pi t^2} \frac{1 + \sin \phi}{2} \quad (6)$$

combining and relating t to r gives:

$$I_{D1} = \frac{I_0 K \rho A_D}{16 \pi r} \sin \theta \sin \gamma (1 + \sin \phi)^2 d\theta d\gamma d\phi \quad (7)$$

The total detected count rate in detector #1 is then this expression integrated over the entire scattering volume.

$$I_{D1} = \frac{I_0 K \rho A_D}{16 \pi r} \iiint \sin \theta \sin \gamma (1 + \sin \phi)^2 d\theta d\gamma d\phi \quad (8)$$

Integrating ϕ from 0 to 2π yields:

$$I_{D1} = \frac{3 I_0 A_D K \rho}{16 r} \iint \sin \theta \sin \gamma d\theta d\gamma \quad (9)$$

Integrating γ from 0 to $\pi - \theta$ yields:

$$I_{D1} = \frac{3 I_0 A_D K \rho}{16 r} \int (1 + \cos \theta) \sin \theta d\theta \quad (10)$$

Integrating θ from 0 to π yields:

$$I_{D1} = \frac{3 I_0 A_D K \rho}{8 r} \quad (11)$$

The expression for detector #2 is arrived at in the same manner giving:

$$I_{D2} = \frac{I_0 A_D K \rho}{16 \pi r} \iiint \sin \theta \sin \gamma (1 + \sin \phi)(1 - \sin \phi) d\theta d\gamma d\phi \quad (12)$$

Again integration gives:

$$I_{D2} = \frac{I_0 A_D K \rho}{8 r} \quad (13)$$

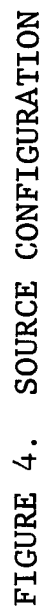
Equations (11) and (13) provide the basis for the design of the sensor by predicting the count rates as a function of density for the particular geometrical configuration.

3.2 Component Description. Component designs for the Air Density Sensor are presented below along with design analyses and functional data.

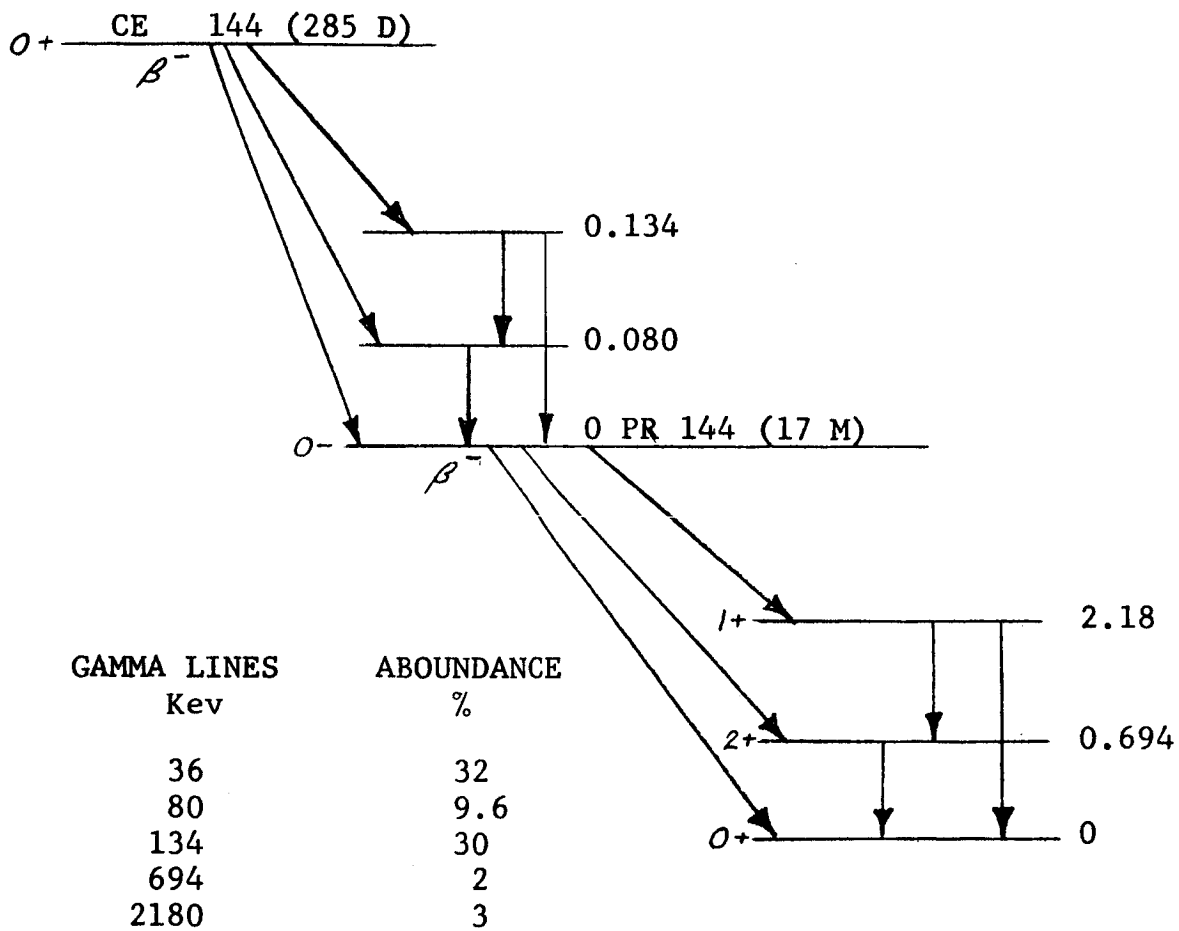
3.2.1 Source. The source configuration is illustrated in Figure 4. The source material is Cerium-144 and its daughter Praseodymium-144. The decay scheme for the isotope is illustrated in Figure 5. Beta and gamma emissions and their abundance are listed in Figure 5. The 134 Kev gamma emission is the one of interest for the scattering experiments. Bremsstrahlung radiation resulting from absorption of the beta emission in the capsule walls also contributes some useful low energy gamma radiation. The few percent of high energy gamma radiation from the Praseodymium-144 daughter are undesirable since they increase the shielding required between the source and detector. Several other sources were considered for this application which did not have this undesirable high energy gamma component. However, the specific activity of these sources was low compared to that attainable with Cerium-144 so that for equivalent strengths in curies sources of large physical size were required. For reasonable source geometries self absorption became significant and limited the low energy gamma outputs. These factors were traded off against the shielding required to reduce the high energy gamma components. It was decided that the shielding problem was less severe than obtaining a small, high strength source with no high energy components.

The gamma spectrum of a 5 microcurie calibration source with a 546 mg/cm² beryllium window was measured with a 1-inch diameter 1-inch long NaI(Tl) crystal detector and is shown in Figure 6A. The predominant gamma peaks are evident. The beta output was absorbed in the beryllium window, air, and aluminum detector housing, all low Z materials with very little resultant Bremsstrahlung radiation.

The gamma spectrum of a 0.5 curie test source of the configuration of Figure 4 was measured with the same detector giving the spectrum of Figure 6B. The Cerium-144 was mixed with a cerium oxide filler material to obtain the same self



1. Source shall be oriented as shown.
2. End tab of outer container shall press onto inner container so inner container shall not move.
3. Tungsten can be spot welded or silver soldered to inner container. Keep solder away from end to be welded.
4. Engrave .090 high x .01 deep (maximum) characters on outer container approximately as shown. Engrave "Caution - Radioactive Material" and insignia only.
5. Fill engraving with red ink (1000°F high temp.) made by Mark Tex Corporation, 163 Coolidge, Englewood, N.J. or



DECAY SCHEME
CERIUM 144, PRASEODYMIUM - 144

FIGURE 5

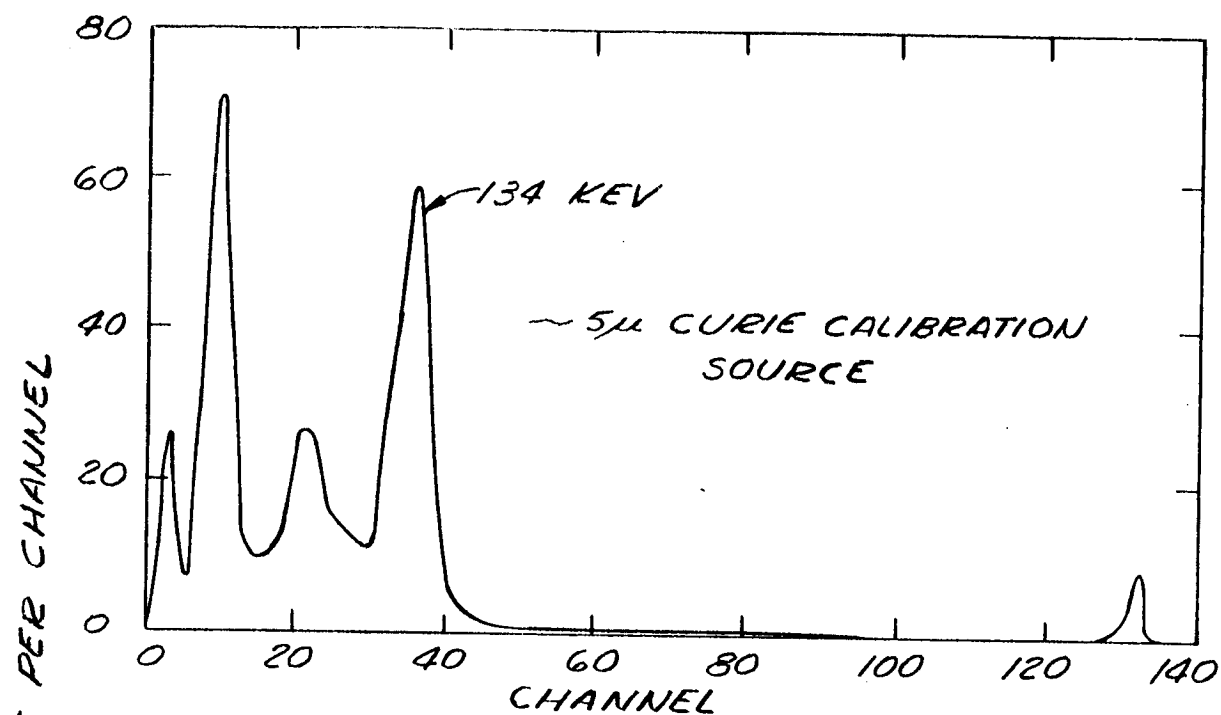


FIG. 6A

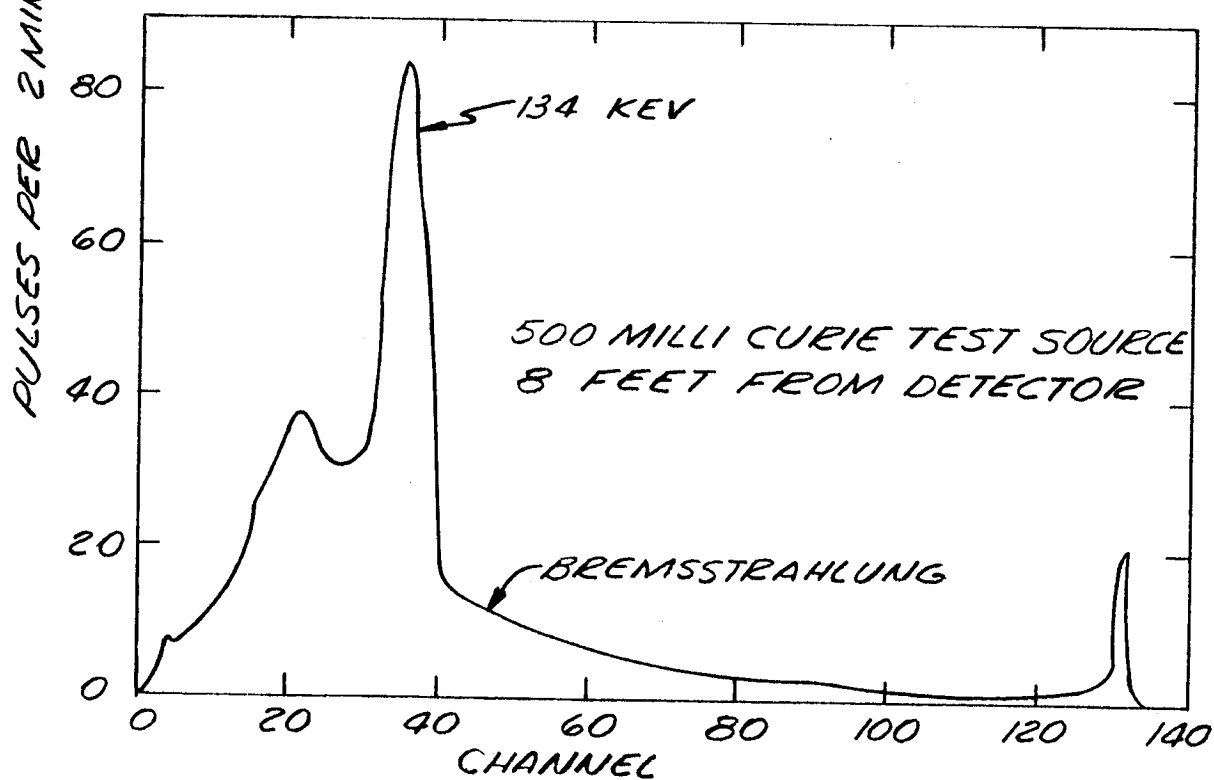


FIG. 6B

CERIUM 144 ENERGY SPECTRUM
1x1 NaI(Tl) DETECTOR

absorption characteristics as the flight source. This test source was placed in the 1/4 inch thick fiberglass nose cone in the flight position. In this case the low energy gammas are absorbed by the 800 mg/cm² double steel capsule and the 1100 mg/cm² fiberglass nose cone. The betas are absorbed in the cerium oxide and steel capsule giving rise to some Bremsstrahlung radiation.

The azimuth radiation pattern of the source was measured and is shown in Figure 7. A tungsten shield attenuates the radiation on one side of the source. The theoretical estimate of this pattern given by equation (1) is shown dashed. The measured pattern indicates more radiation to the sides and back of the source than was estimated.

The elevation pattern of the source is shown in Figure 8. The theoretical estimate of this pattern given by equation (1) is shown dashed. The measured pattern is shown skewed forward of the theoretical. This is for the most part a result of the attenuation afforded by the conical skin.

The source capsule stud is pinned in the nose piece in a way which allows free rotation of the capsule about its axis. As the nose piece and source are screwed into the nose cone, an orientation tab on the source capsule picks up a locating slot in the nose cone providing positive orientation of the azimuth radiation pattern with respect to the detectors.

The peak intensity of the source patterns is computed below.

Let:

S = source strength in curies

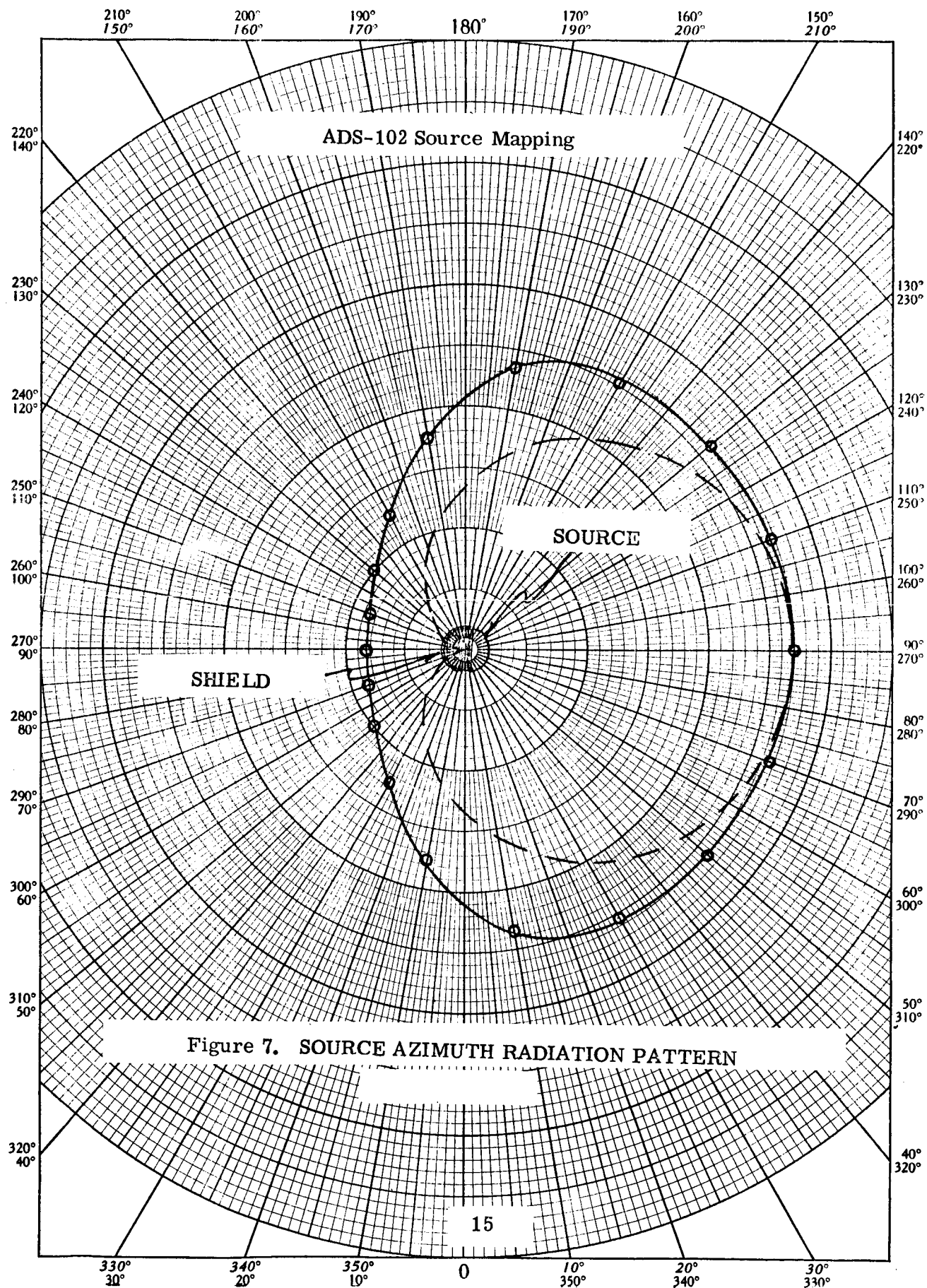
ϵ_1 = self-absorption

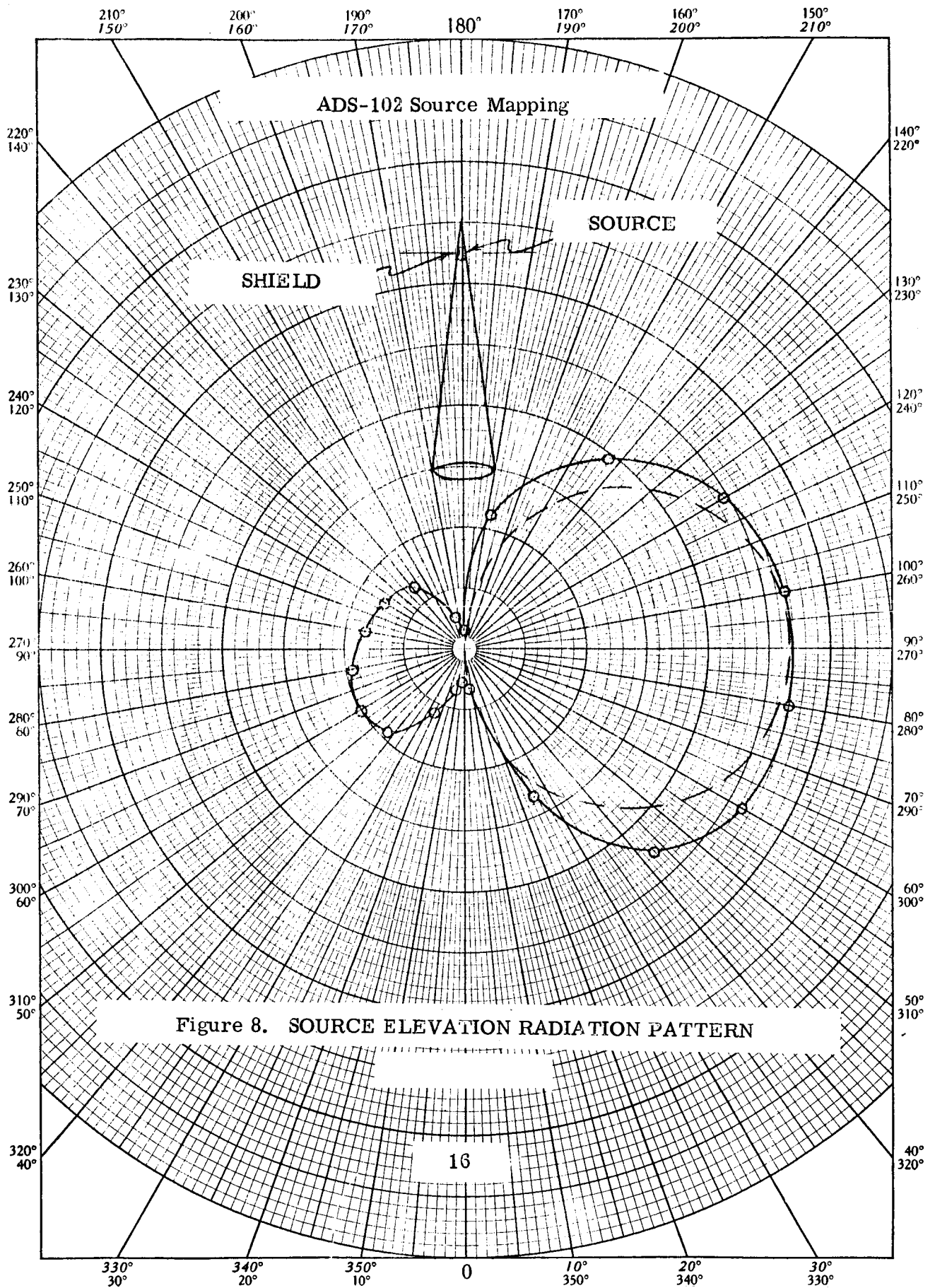
ϵ_2 = absorption in capsule walls

ϵ_3 = absorption in skin

ϵ = abundance of 134 Kev gammas

I_0 = effective source strength in pulses/second





The effective source strength is,

$$I_o = 3.7 \times 10^{10} \text{ S } \epsilon_1 \epsilon_2 \epsilon_3 \quad (14)$$

The self-absorption is given by:

$$\epsilon_1 = \frac{1}{\mu d} (1 - e^{-\mu d}) \quad (15)$$

For 134 Kev gammas in cerium oxide,

$$\mu = 2 \text{ cm}^{-1}$$

and the source of Figure 4,

$$d = .45 \text{ cm}$$

$$\epsilon_1 = \frac{1}{2 (.45)} (1 - e^{-2(.45)}) = .66$$

The capsule wall absorption ϵ_2 is given by:

$$\epsilon_2 = e^{-\mu x} \quad (16)$$

where for steel $\mu = 2 \text{ cm}^{-1}$ and the thickness $x = .1 \text{ cm}$

$$\epsilon_2 = e^{-.2} = .82 \text{ (measured } \epsilon_2 = .78)$$

The one way skin absorption ϵ_3 is given by,

$$\epsilon_3 = e^{-\mu x} \quad (17)$$

where for the fiberglass $\mu = .27 \text{ cm}^{-1}$ and the thickness $x = .63 \text{ cm}$:

$$\epsilon_4 = e^{-0.17} = 0.84 \text{ (measured } \epsilon_4 = .85)$$

The abundance of the 134 Kev gammas is,

$$\epsilon = .030$$

The effective source strength is thus:

$$I_o = 3.7 \times 10^{10} \text{ S } .66 \times .82 \times .84 \times .30 =$$

$$I_o = 3.7 \times 10^{10} \text{ S } 0.136 \text{ pulses/second/}4\pi \text{ steradians, } (18)$$

3.2.2 Shield. A 15-inch long truncated cone of lead provides shielding against the direct transmission of radiation from source to detector. The low energy gamma radiation, beta radiation, and resulting Bremsstrahlung radiations are easily absorbed by the lead. A possible 3% abundance of 2.18 mev gammas presents the most severe shielding problem. The 15 inches of lead attenuates this radiation to the point where less than two photons per second reach the scintillation counter. This value is arrived at theoretically. No practical means of measuring the amount of direct transmission has been attempted thus far. The direct transmission calculation is given below:

$$I_T = \frac{I_o A_D}{4\pi r^2} D e^{-\mu r} \quad (19)$$

where:

I_T = transmittal flux, pulses per second

I_o = source strength - for 25 curies and 3% abundance

$$I_o = 25 \times 3.7 \times 10^{10} \times .03 = 2.77 \times 10^{10} \text{ pulses/sec.}$$

A_D = detector area which is 31 cm^2

r = source-detector separation and length of lead = 38 cm

μ = absorption coefficient of lead for 2.18 mev gamma = $.51 \text{ cm}^{-1}$

D = dose buildup factor for 2.18 mev gammas in lead with $\mu r = 19.4$, $D = 8$

then:

$$I_T = \frac{2.77 \times 10^{10} \times 31}{4\pi (38)^2} 8 e^{-19.4}$$

$$I_T = 1.33 \text{ pulses/second}$$

A second function of the lead shield is to provide a degree of shaping to the source radiation pattern and detector sensitivity pattern such that little scattering will occur within the vehicle shock layer.

3.2.3 Detector. The detector assembly is illustrated in Figure 9. It consists of two half cylinders of thallium-activated sodium iodide crystal separated by a thin tungsten shield. Each of these crystals is optically coupled with a clear RTV Silastic to an RCA 4441 photomultiplier tube. Each tube is shielded both magnetically and electrostatically. The electrostatic shield also serves to hold the tube envelope at the photocathode potential. The tubes are operated electrically as illustrated in Figure 10. The output pulses corresponding to the 134 Kev gammas detected are approximately 30 millivolts high and 0.5 microsecond wide into the 1000 ohm discriminator load.

With a -1000 volt supply the phototube current gain is approximately 6×10^5 and the equivalent anode dark current is about 1.6×10^{-2} microamperes at 25°C. This dark current or phototube noise is plotted as count rate versus the equivalent gamma energy scintillation input to the detector in Figure 11. It is seen that the noise is low compared to the discriminator threshold. The noise level increases rapidly with temperature. With the phototube at 60°C the noise level may increase 100 times possibly causing a significant noise level. In this application the insulation properties of the vehicle skin and detector housing and short duration of the flight keep the detector temperature rise small.

The low value dynode resistors in the divider string, 100K each, allow relatively large average dynode currents without significant changes in dynode voltage. The .01 μ f capacitors on the last three dynodes allow large peak currents without significant changes in dynode voltage. This allows a large dynamic range of count rates with coincidence loss due to the 0.25 μ sec scintillator decay characteristics being the only limiting factors in detector count rate linearity.

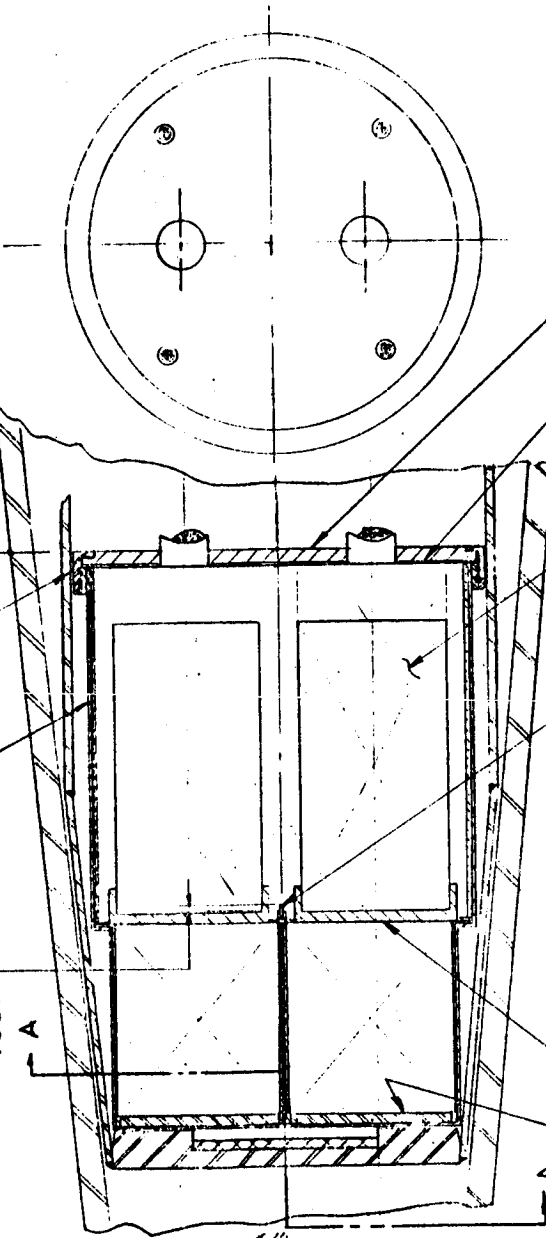
THREADED RETAINING RING X3042561

HOUSING X3042564

STA 29.326

X3042566 SCINTILLATOR
NEOPRENE CUSHION 1/8 THK
2 PLACES

030
1020



SECT A-A

X3042565 TUBE RETAINER

NEOPRENE

X3042562 RETAINING PLATE

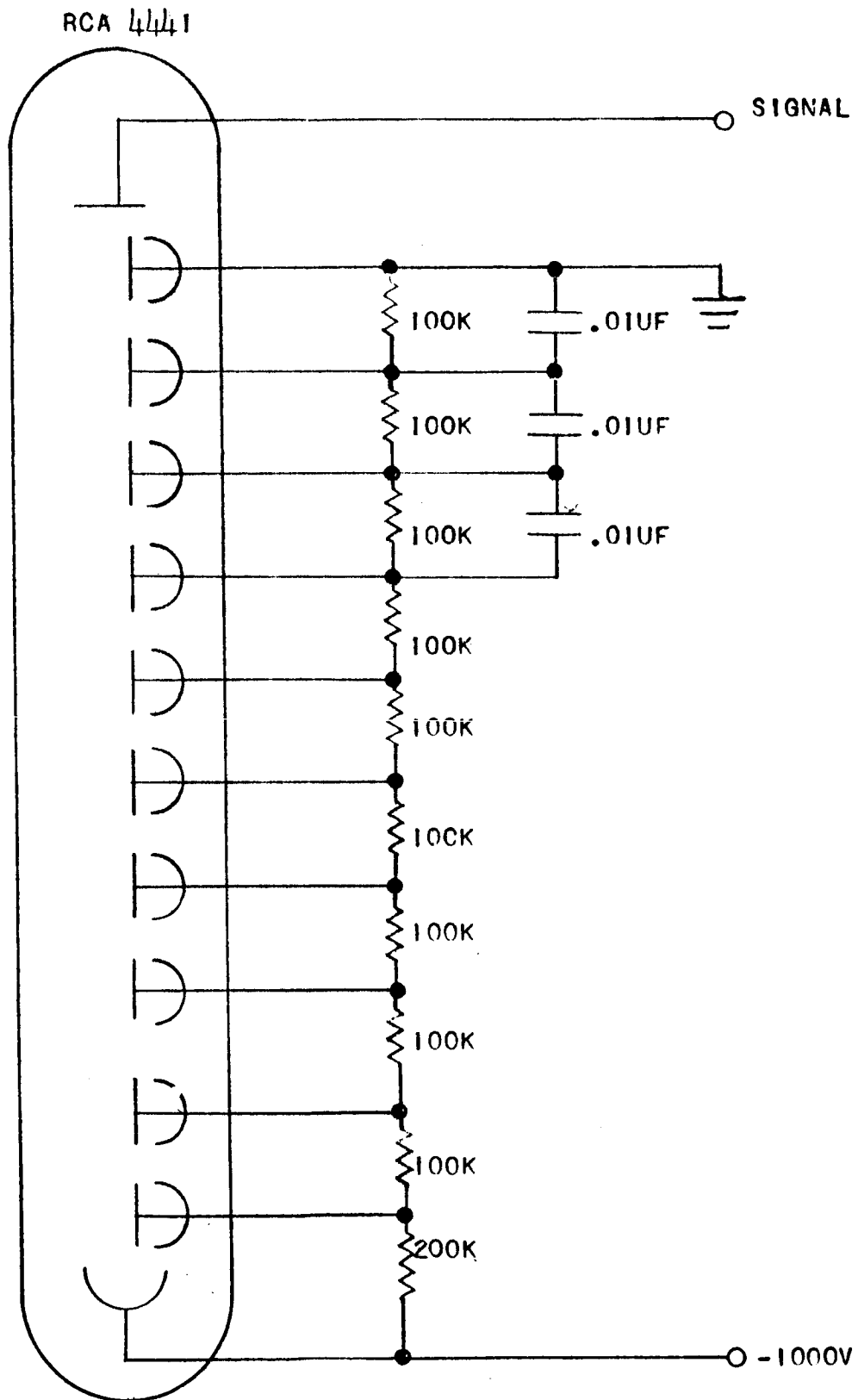
X3042563 HYPERNON SPACER

DETECTOR ASSY.

14905 X3042560 X1

X3042832 PHOTOMULTIPLIER TUBE ASSY
2 REQD
X3042568 SHIELD ASSY

FIGURE 9. DETECTOR ASSEMBLY



MULTIPLIER PHOTOTUBE SCHEMATIC

FIGURE 10

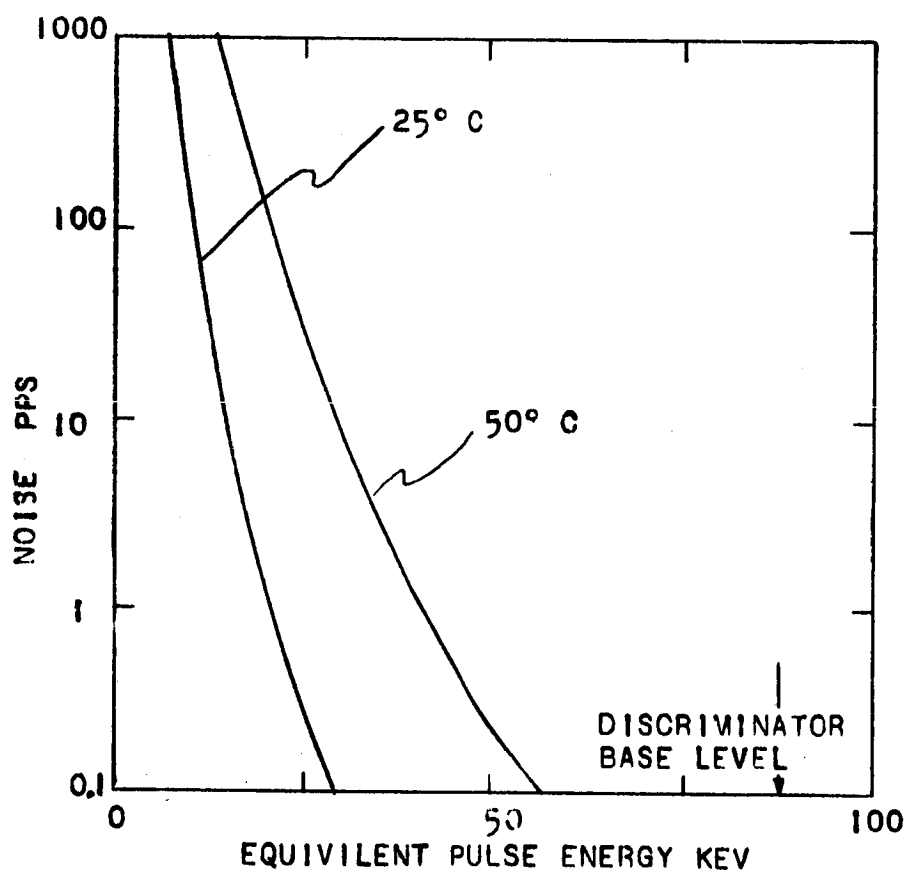


PHOTO TUBE NOISE REFERRED
TO MEASUREMENT PARAMETERS

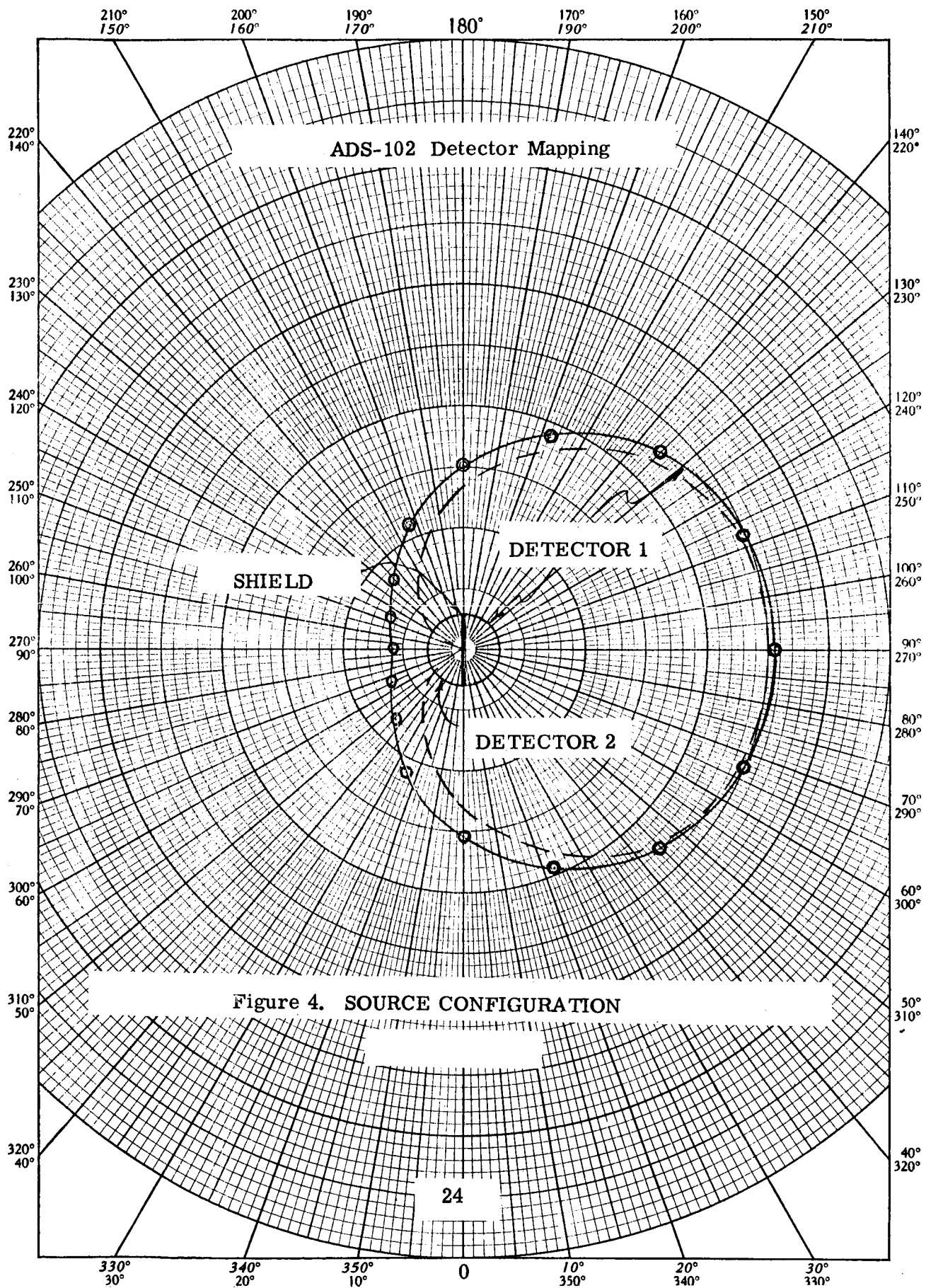
FIGURE 11

The sensitivity pattern of each detector in azimuth and elevation are given in Figures 12 and 13. These measured patterns follow closely the predicted patterns of equation 2 shown dashed. The detectors are aligned with respect to the source such that the angle of maximum sensitivity of detector #1 corresponds to the angle of maximum flux from the source.

3.2.4 Discriminators. The discriminator circuitry is illustrated in Figure 14. The phototube output passes to a video amplifier with a voltage gain of 50 and flat response to 2 mcs. The amplified signals are passed to a base level selector and an inhibit level selector. The base level selector using a tunnel diode triggering circuit provides output pulses for all input pulses greater in amplitude than the desired base level. The inhibit level selector using a similar circuit provides an inhibit pulse for each input pulse greater than the desired inhibit level. Pulses from the base level selector are delayed such that when they occur coincident with an inhibit pulse they are blanked out completely. With no inhibit pulse they occur as output pulses. The output pulses as a result occur only when the input pulse is above the base level and below the inhibit level. Adjustment of these levels is provided by selection of series resistors controlling the current pulse to the tunnel diodes.

The discriminator output pulses are 10 volts in height and 0.2 microsecond in width. The base level circuitry operates up to 2×10^6 pulse per second rates and the inhibit circuitry operates up to 0.2×10^6 pulse per second rates. The discriminators are packaged on circuit boards and potted in aluminum cases.

3.2.5 Signal Conditioning Electronics. The signal conditioning electronics is comprised of a series of flip-flops and pulse shapers. Each unit is fabricated as a welded module as illustrated in Figures 15, 16 and 17. The pulse shapers provide pulses of widths compatible with the telemetry bandwidths. These pulse widths are adjusted by selection of an external resistor and capacitor. An emitter follower circuit is included in each pulse shaper output to drive pulse signals through long monitoring cables prior to launch. The expected pulse rates out of the detectors and pulse shapers are plotted in Figure 18. The pulse widths are nominally 50 microseconds, 100 microseconds, and 500 microseconds out of the three pulse shapers. The frequency limitations of these pulse shapers are 10,000, 5,000 and 1,000 pulses per second respectively.



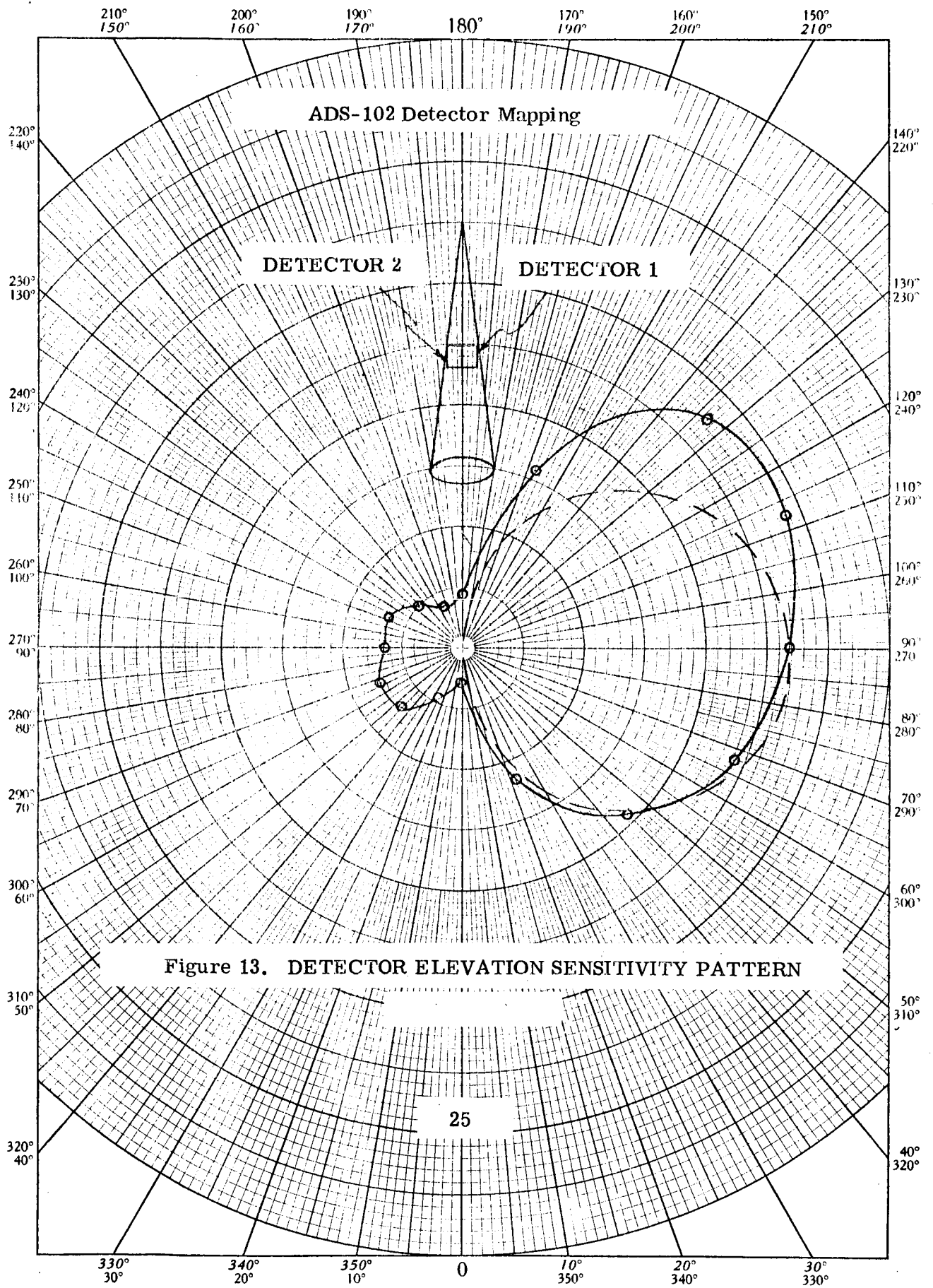
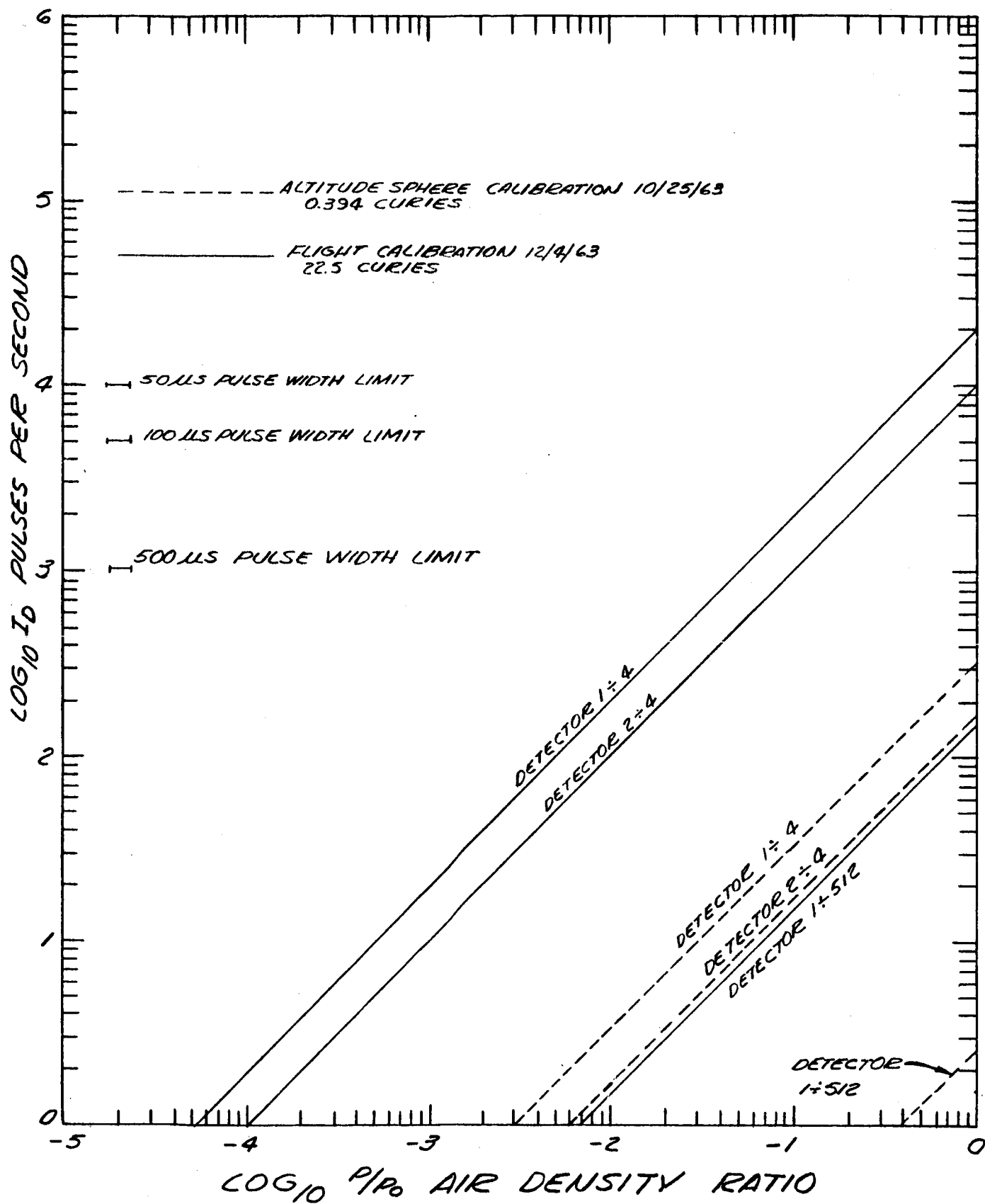


FIGURE 17. PULSE SHAPER



EXPECTED COUNT RATES ADS-102
 FIGURE 18

Referring to Figure 18, at sea level density with the 0.5 curie test source, all channels operate without saturation. At sea level density with the 25 curie flight source, only the divide by 512 channel of detector #1 is operating. The two divide by four channels are saturated. At a low altitude, the second detector becomes operative through the divide by four channel and soon after, all channels are operating. This allows complete calibration with the test source, complete coverage from sea level with one detector, and earliest operation of both detectors. The divide by four channels provide accurate reproduction of low count rates expected at high altitudes without long intervals between pulses contributing to velocity error.

3.2.6 Auxiliary Sensors. The auxiliary sensors included in this payload are an accelerometer and four temperature sensors. The accelerometer is a GCC Model 24155 with a range of -20 to +80 g and a potentiometer output. The temperature sensors are thermistors. The resistive networks and supply voltage regulators for the thermistors and accelerometer are illustrated in Figure 19. An additional test voltage is supplied by this network which indicates the condition of the battery pack and power supply. As the battery pack weakens, this voltage will drop and if the DC-DC converter fails, a step drop in voltage will occur.

3.2.7 Telemetry. FM-FM telemetry is used in this payload to transmit data to the ground station. The transmitter is a United Electrodynamics Model TR-16A with a 2-watt output minimum and carrier frequency of 244.3 megacycles per second.

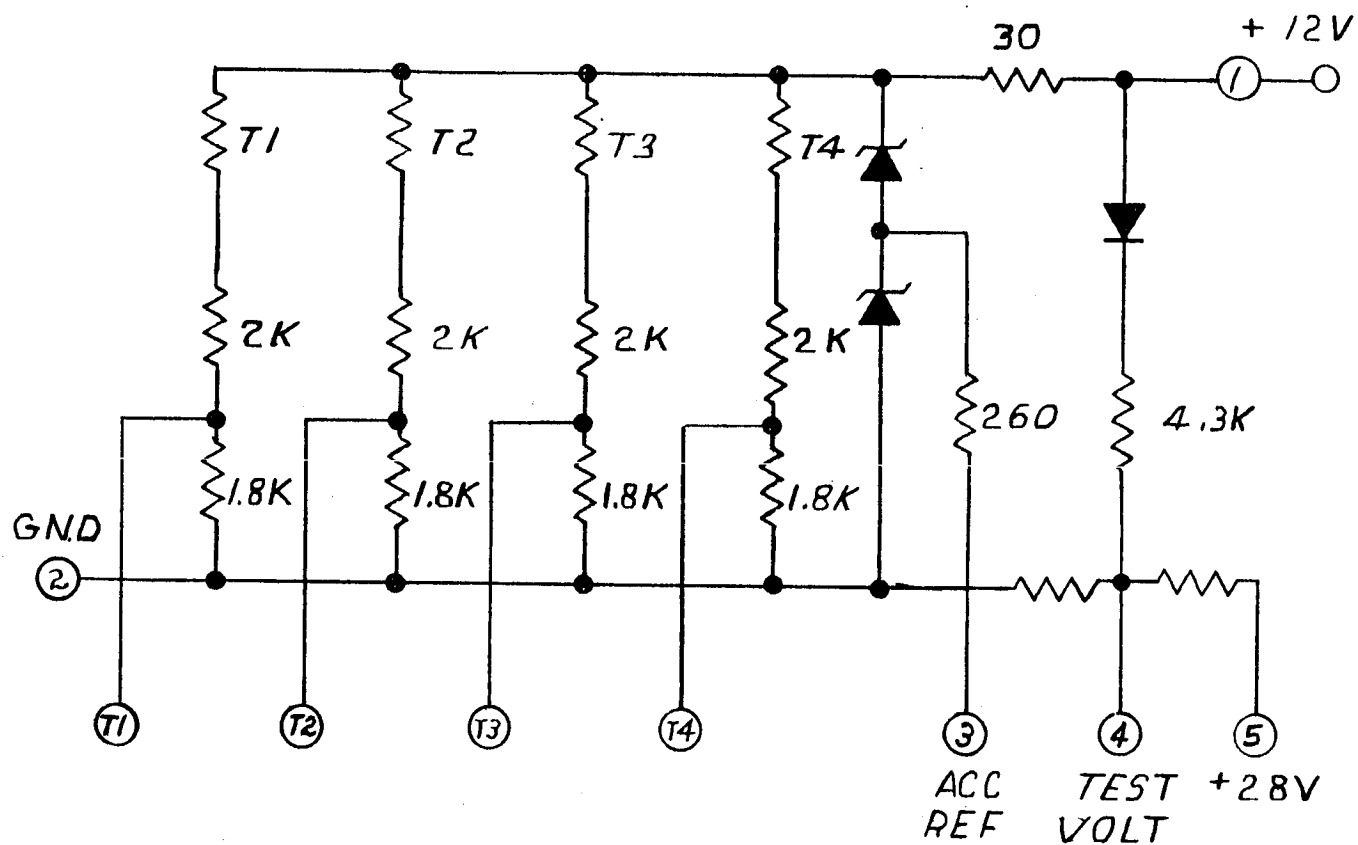
Ten Bendix Model TOE-305 Voltage Controlled Oscillators and Model TAA-305 Composite Signal Amplifier are used to modulate the transmitter. Standard IRIG subcarrier channels are used. Channels 7 through 13 carry low bandwidth or DC information. Channels 14, C, and E carry pulse data. Table I gives the telemetering requirements.

The antenna is the cylindrical portion of the payload section. Figure 1 illustrates the split Inconel fuselage and alumina insulation.

TABLE I

TELEMETRY REQUIREMENTS

IRIG Channel	Data	Data Form	SC0 Center Frequency cps	Frequency Deviation %	Deviation Ratio	Intelligence Frequency cps
E	Detector 2:4	50 μ s Pulse	70,000	± 15	1	10,000
C	Detector 1:4	100 μ s Pulse	40,000	± 15	1	5,000
14	Detector 1:512	500 μ s Pulse	22,000	± 7	1	1,000
13	Acceleration	dc - 100 cps	14,000	± 7	5	100
12	Test Voltage	dc	10,500	± 7	5	dc
11	Spare		7,350	± 7	5	
10	Temperature 4	dc	5,400	± 7	5	dc
9	Temperature 3	dc	3,900	± 7	5	dc
8	Temperature 2	dc	3,000	± 7	5	dc
7	Temperature 1	dc	2,300	± 7	5	dc



SCHEMATIC
TEMPERATURE SENSORS AND
REFERENCE VOLTAGES

FIGURE 19

An RF shielding cover and gasket are placed over the entire telemetry section to minimize noise in the sensor. All electrical connections through this cover are made through Allen Bradley SMFB-A2 low pass filters to minimize RF noise on lines.

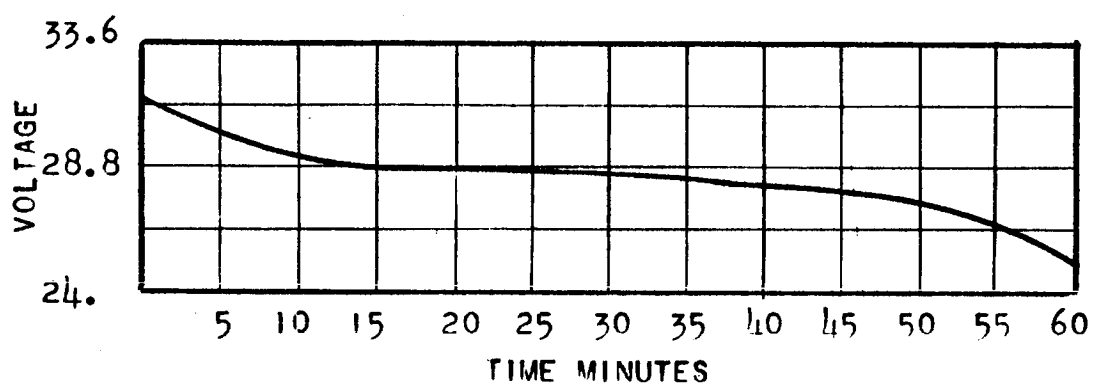
3.2.8 Power. Primary power for the payload package is derived from a battery pack of 24 Gould National Nickel Cadmium rechargeable batteries, Model 2.3SC. The total payload requires 1.8 amperes of 28 volts DC current. Figure 20 shows battery life at this rate to be 40 minutes at 25°C. The recharge rate is 230 milliamperes for 14 hours with a 36-volt limit on the charging voltage.

Power is converted to several voltage levels by the DC-DC converter, Figure 21. Minus 1.5 volts, -1,000 volts, +12 volts, and +28 volts are required by the electronics. The unit is packaged as a welded module. External resistors are employed in the regulation loop for adjustment of the -1,000 volts during system calibration.

3.2.9 Ground Interface. During calibration and checkout prior to launch external power is supplied and sensor outputs are monitored via an umbilical connector, cabling, and test set. The schematic and assembly drawing of this test set are shown in Figures 22 and 23. Interlock circuitry is provided which prevents any voltages from being present on either connector until the two are properly mated. A set of six two-pole double throw crystal can size latching relays (Clare LF110S) perform this deactivation of the umbilical in the payload as well as switch battery power to the sensor electronics and telemetry equipment. Two relays are used in parallel to switch the power in order to improve the reliability of this critical function.

The functions of the test set are listed below:

- 1) Provide ground power to the sensor and display current.
- 2) Provide ground power to the telemetry packages and display current.
- 3) Provide battery charging function and display charging current.
- 4) Switch from ground power to battery power and vice versa.



BATTERY PACK LIFE

FIGURE 20



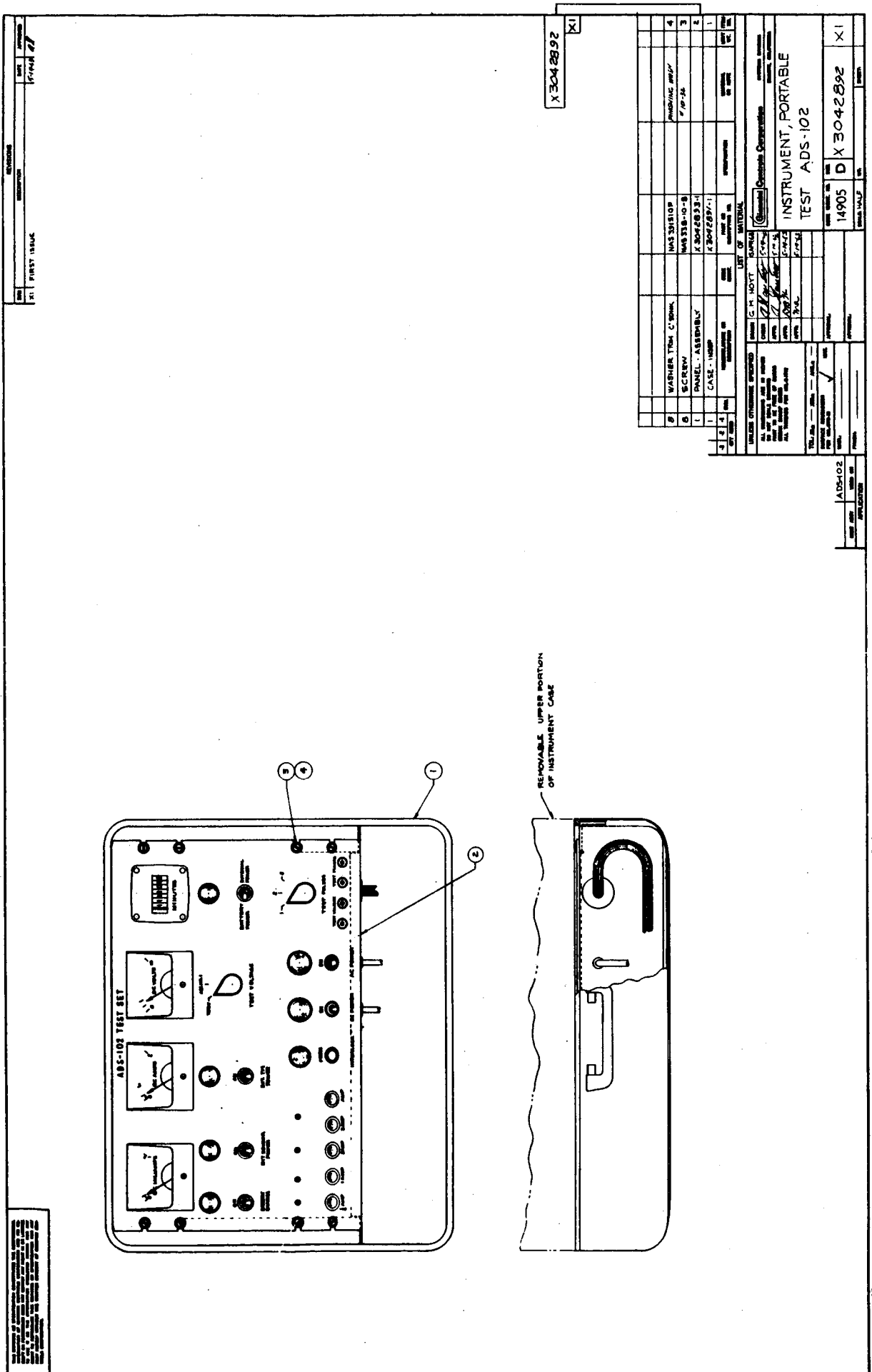


FIGURE 23. PORTABLE TEST INSTRUMENT

- 5) Measure and display elapsed time accumulated on battery power.
- 6) Actuate interlock.
- 7) Provide lights to indicate above operation being performed.
- 8) Present pulse signals from channel 1 divided by 4 and 512.
- 9) Present pulse signals from channel 2 divided by 4.
- 10) Measure test voltage and accelerometer output.

Power required by the test set is 115 volts 60 cycles, and 28-36 volts, 3 amperes of DC. Variable DC is required for battery charging and to adjust for voltage drop through long cables.

3.3 Structural Design. The internal structure and skin structure each are designed to the stress requirements established in Appendix I. The internal structure beam is a weldment of 6061 aluminum heat-treated to a T6 condition. Bakelite strips were added to the flanges on the beam between stations 29 and 37 to provide damping to a vibration resonance. Bakelite stiffeners were also added between stations 40 and 44 to help damp a longitudinal structural resonance.

A fiberglass insulator is placed at the mounting point to the Apache head cap and a heavy aluminum base plate is used as heat sink. This reduces the temperature rise of the internal structure due to heat transfer from the Apache booster. The nose cone is fabricated of LD-91 Phenolic fiberglass covered with a teflon blanket. This provides ablative cooling of the nose cone and extremely good insulation. The Inconel fuselage has an insulation blanket attached to its inner surface. As a result the internal structure and instrument packages are affected little by the extreme temperature environments during ascent and re-entry of the payload package.

An aluminum heat sink is also added to the structure under the transmitter to minimize self-heating during warm-up and checkout of the payload package prior to launch. The thermal characteristics of the payload were simulated on an analog computer to determine the expected sensor temperatures. The resultant temperature curves are shown in Figure 24. The actual temperature rise from flight data is shown dashed.

3.4 Electrical Assembly. The wiring diagram of the payload package is presented in Figure 25. As far as possible, shielded wiring and single point grounding are employed to minimize the possibility of noise interference. The majority of shields are picked up at the forward header and carried to the ground bus. All leads passing through the shielding cover to the telemetry deck have their shields grounded to the cover.

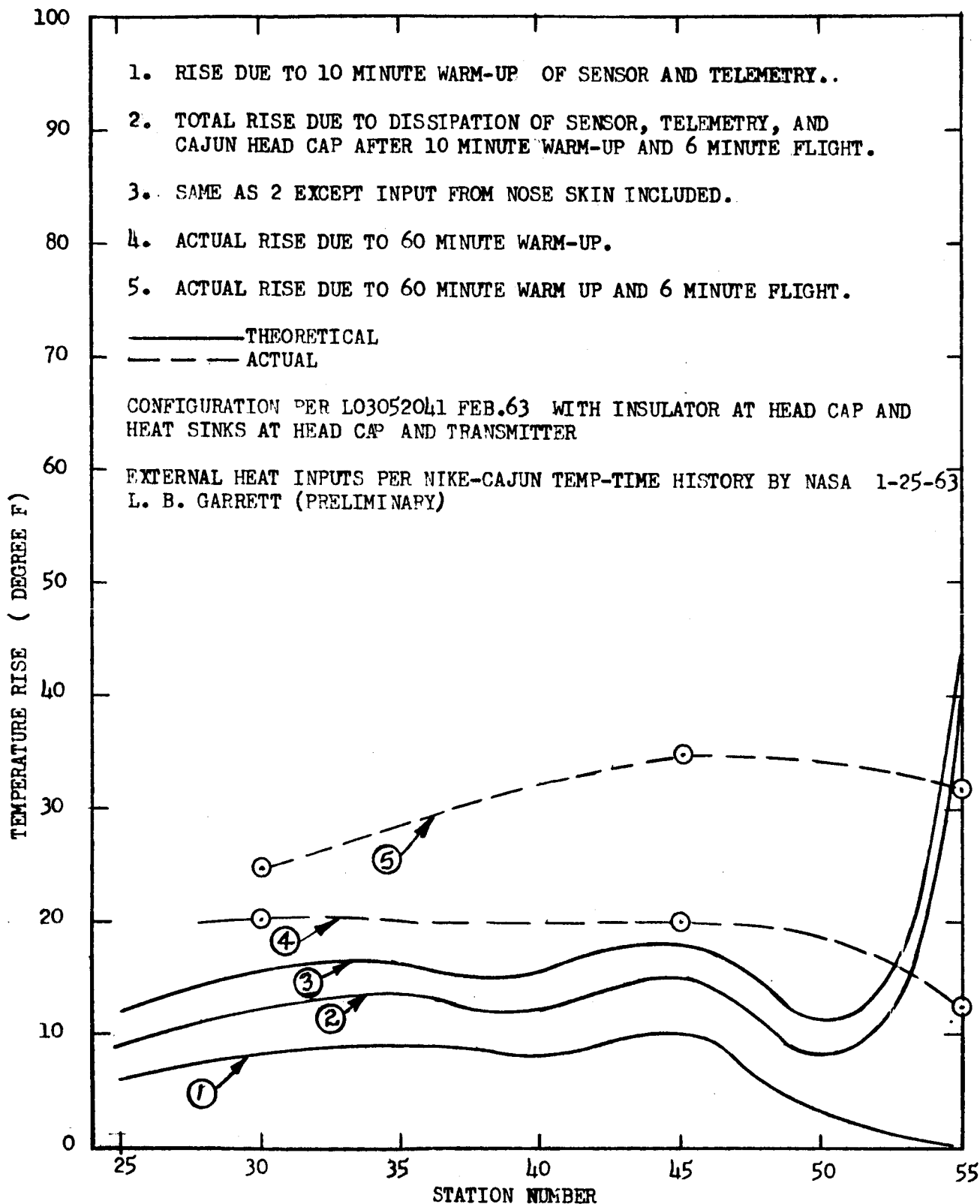
3.5 Calibration Procedure. The unit is calibrated prior to flight test following generally the outline below.

3.5.1 DC-DC Converter. Regulation resistors are selected to provide -1,000 volts high voltage output. The sum of the two resistances should be approximately 3.4 k ohms. Typical values are 3.3 k ohms and 360 ohms.

3.5.2 Pulse Shapers. Capacitor and resistor values are selected to provide the proper pulse widths out of the pulse shapers. Typical values are given below.

7.5 k ohms	.01 μ fd	50 μ s pulse
7.5 k ohms	.015 μ fd	100 μ s pulse
7.5 k ohms	.06 μ fd	500 μ s pulse

3.5.3 Discriminators. Trimming resistors are selected to provide the desired base level and window width of the discriminators. These values are selected by monitoring the count rates out of the system in response to a carefully located calibration source. With the Cerium-144 calibration source (10 μ curies, 1 January 1963) placed in the calibration position on the top face of each detector, the levels should be adjusted to provide the count rates equivalent to a 90 Kev base level and 150 Kev inhibit level. With the inhibit signal disabled the base level is adjusted to give the upper count rate, then the inhibit level is adjusted to reduce the count rate to the final level.



ANTICIPATED AND ACTUAL TEMPERATURE RISE OF
INTERNAL PAYLOAD AT VARIOUS STATIONS

FIGURE 24

3.5.4 Telemetry. The transmitter and subcarrier oscillator assembly are checked out through a telemetry test box. The subcarrier frequencies are adjusted individually with a 0, + 2.5, and +5 volt input in accordance with Table I. The output amplitudes of the subcarrier oscillators are adjusted to modulate the transmitter carrier frequency in accordance with a 6 db pre-emphasis taper.

4.0 PERFORMANCE

This section describes the performance characteristics of the Air Density Sensor ADS-102 flight test unit No. 1. Calibration data, environmental test data, flight test data, and a system accuracy analysis are presented.

4.1 Calibration. The calibrations performed on the flight unit were done in the following sequence with intermediate modifications of the payload made when necessary.

1. Discriminator level setting (8/30/63)
2. Inverse square calibration of sensor (9/11/63)
3. Calibration of telemeter (10/14/63)
4. Calibration of temperature sensors (10/17/63)
5. Calibration of test signal (10/18/63)
6. Readjustment of discriminator level setting after detector revision (10/25/63)
7. Density calibration of sensor in altitude sphere (10/26/63)
8. Final adjustment of discriminator level setting after revision of RF shielding and grounding (11/12/63)

After the first adjustments of the discriminator levels were made, an inverse square calibration of the sensor detectors and electronics was made using the 500 millicurie test source. This calibration data is shown plotted in Figure 26. The output of detector #1 is shown scaled by a factor of 4 and 512 and the output of detector #2 scaled by a factor of 4. These curves follow the proper inverse square relation until the output count rate becomes limited by coincidence loss dictated by the pulse width of the output pulse shapers. If desired, adjustment may be applied to the flight data in regions of very high count rate to correct for these coincidence losses using this data as the correction.

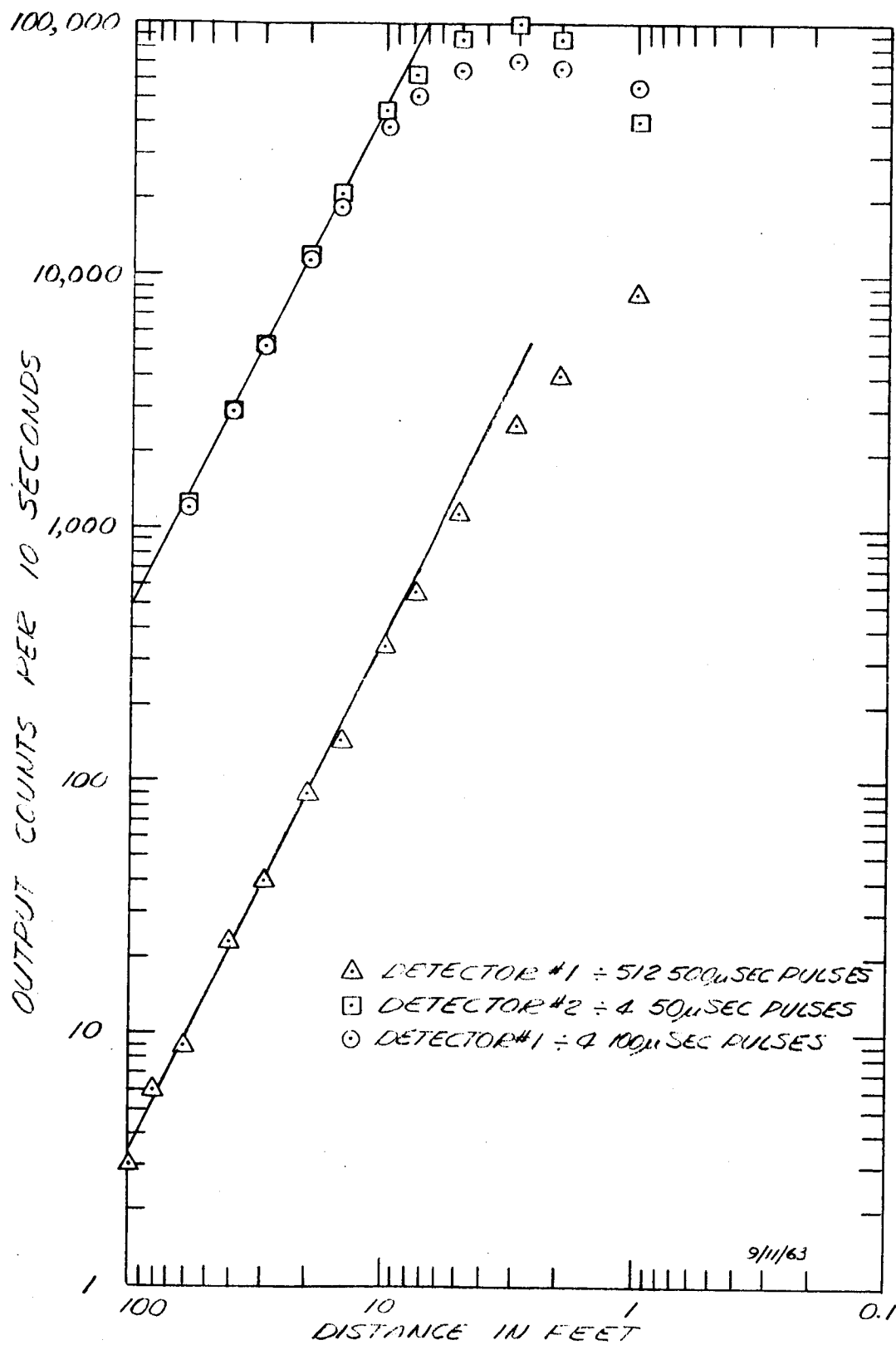


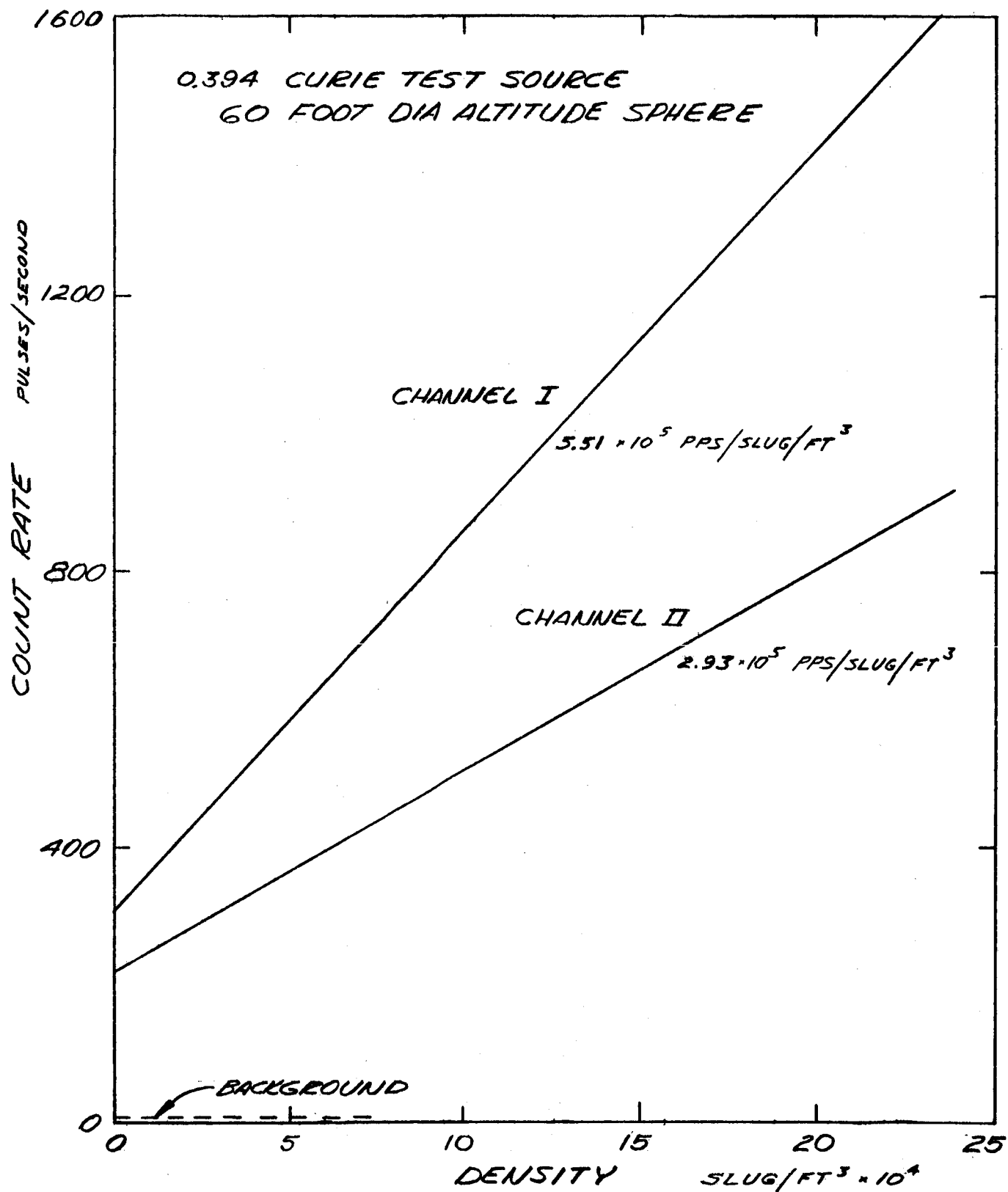
Figure 26. SENSOR RESPONSE TO DIRECT TRANSMISSION
0.438 CURIES CERIU 144 SOURCE

After the first calibration the detector design was altered to reduce a vibration resonance thus requiring re-adjustment of the discriminator settings. This was accomplished and the unit was suspended in the center of the NASA, LRC, 60-foot diameter altitude sphere. Then the 500 millicurie test source was installed and the scattered radiation monitored by detectors 1 and 2. The outputs of these detectors were monitored through the umbilical cable.

The count rate versus density relationship of the sensor was measured at several values of pressure and temperature as the air was being evacuated from the chamber. This relation is shown in Figure 27 as the output of detector 1 and 2 each scaled by a factor of 4. The slopes of these curves gives the scale factor of count rate to density. The intersection of these curves with the ordinate at zero density gives the scatter from the chamber walls plus direct transmission and background.

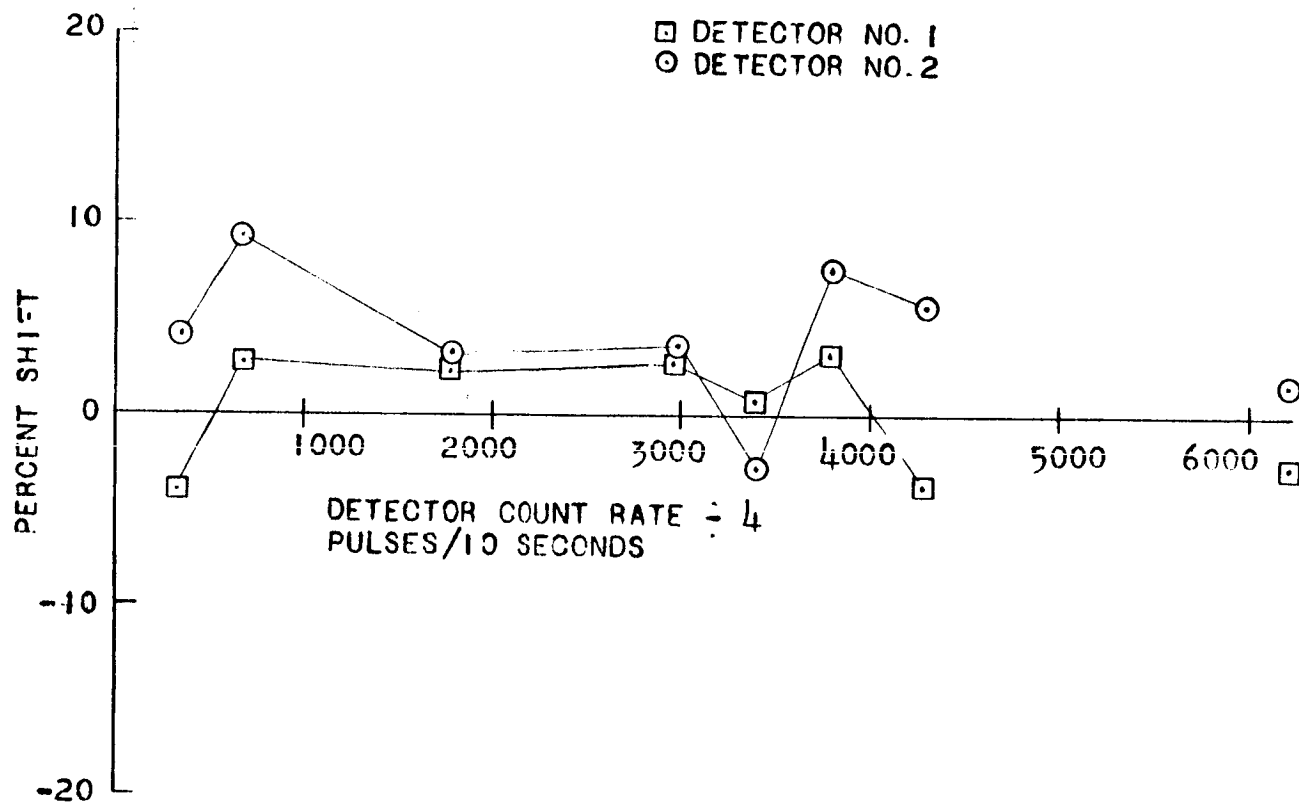
It was noted during these tests in the altitude sphere that the detector calibrations shifted when the telemeter transmitter was turned on and off. Additional RF shielding was introduced in the umbilical wiring and phototube high voltage supply wiring, and the ground points for the wire shields were moved from station 44 to station 37. These modifications reduced the detector sensitivity to RF from the telemeter to an acceptable value. Figure 28 shows the detector sensitivity to this RF as a function of count rate. The data shows the deviation from the calibration condition with the telemeter off and the sensor on external power; to the flight condition with the telemeter on, sensor on battery power, and umbilical disconnected.

Final adjustment of the discriminator level settings was performed to provide the same window that was used in the altitude sphere calibration (90 to 150 Kev). Adjustments were made to give the same base level and inhibit count rates with the calibration source in the calibration position. A correction for half life also was applied. The base level and inhibit level were related to the energy spectrum of the calibration source subsequent to the flight test of the unit. Using an identical crystal, photomultiplier tube, housing, and pre-amplifier a detector was mocked up and the spectrum of the calibration source in the calibration position analyzed. This spectrum is shown in Figure 29. The base level and inhibit level of the flight detectors were determined to be at 90 Kev and 155



SENSOR DENSITY CALIBRATION IN ALTITUDE
SPHERE

FIGURE 27



SENSOR SCALE FACTOR SHIFT DUE TO
TELEMETER RF.

FIGURE 28

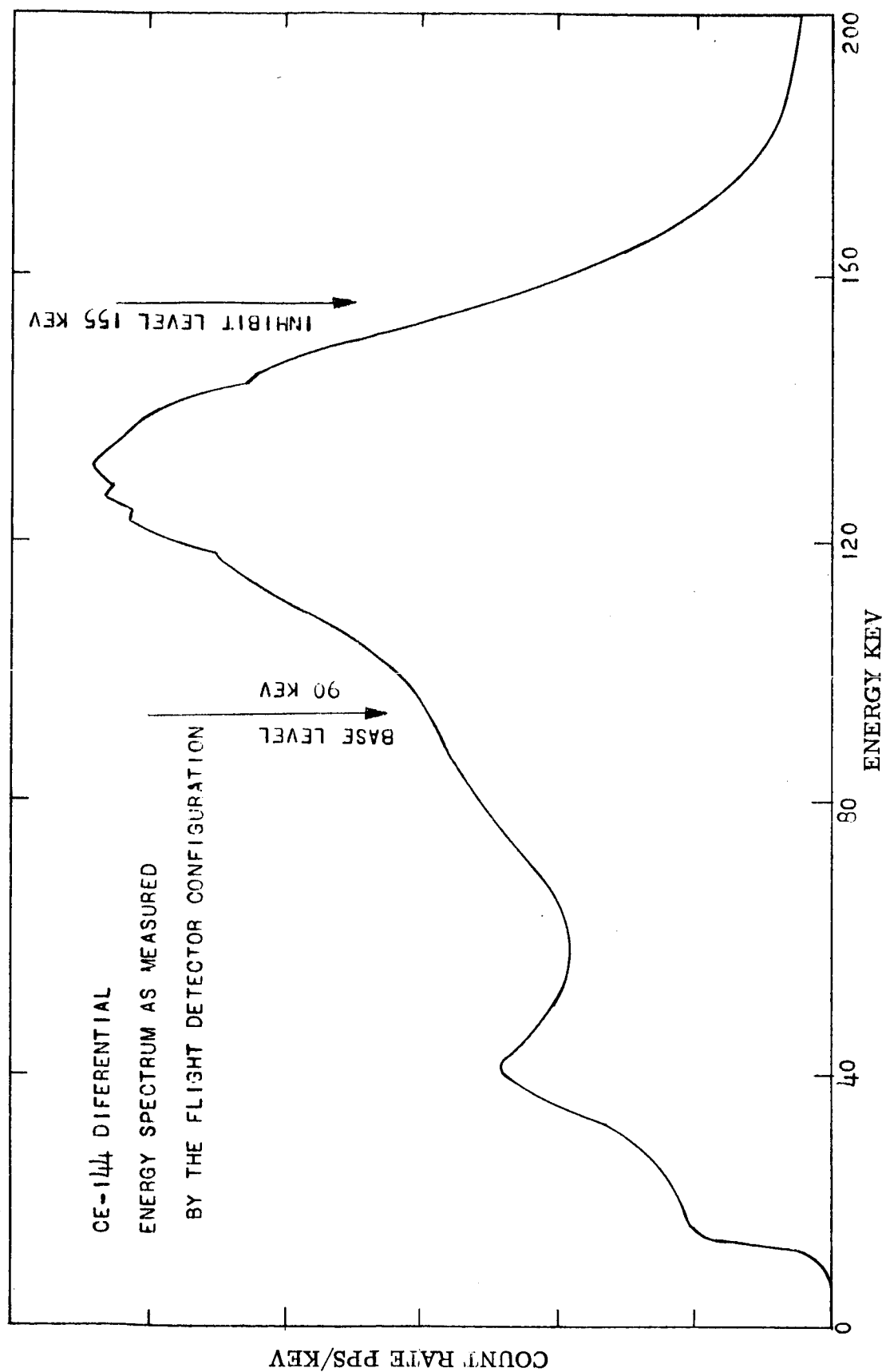


Figure 29. CE-144 DIFFERENTIAL ENERGY SPECTRUM AS MEASURED BY THE FLIGHT DETECTOR CONFIGURATION

Kev respectively.

Calibration of the thermistor temperature sensors located in the payload was accomplished by attaching thermocouples near each thermistor and correlating the two measurements as the temperature was varied. The calibration curves of these thermistors is shown in Figure 30.

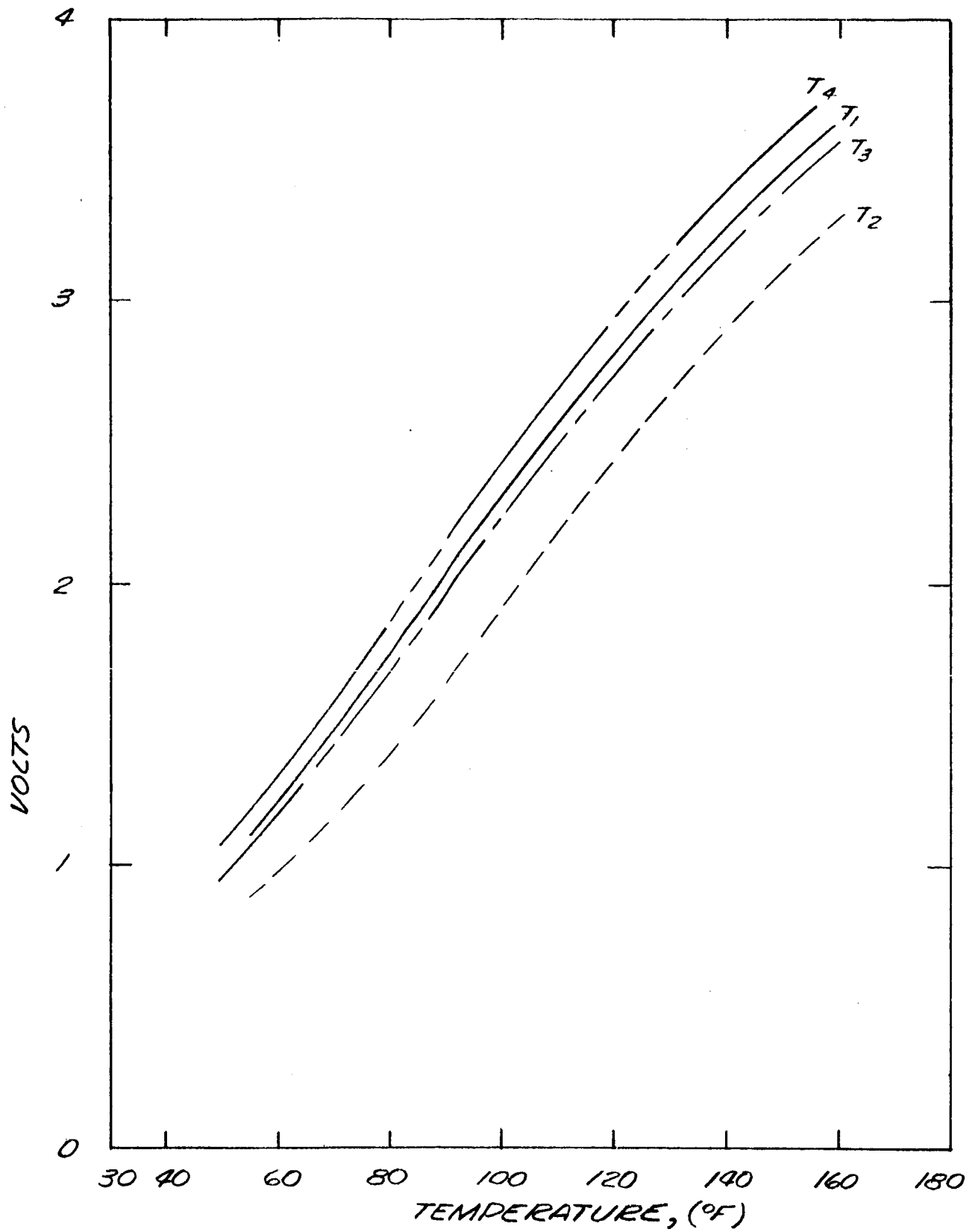
Calibration of the test voltage as a function of battery run-down is shown in Figure 31. All of these calibrations were performed through the telemetry link.

4.2 Environmental Testing. Extensive environmental testing was performed during this program, both on the components and on the entire assembled payload. Table II summarizes the tests run and the levels of severity. The problems encountered in this program of testing and their solutions are summarized below.

1. Flip-flops. Several flip-flops failed at high temperature because they were manufactured with an incorrect resistor value. The resistors were replaced with their proper values and the flip-flop modules were retested and accepted.

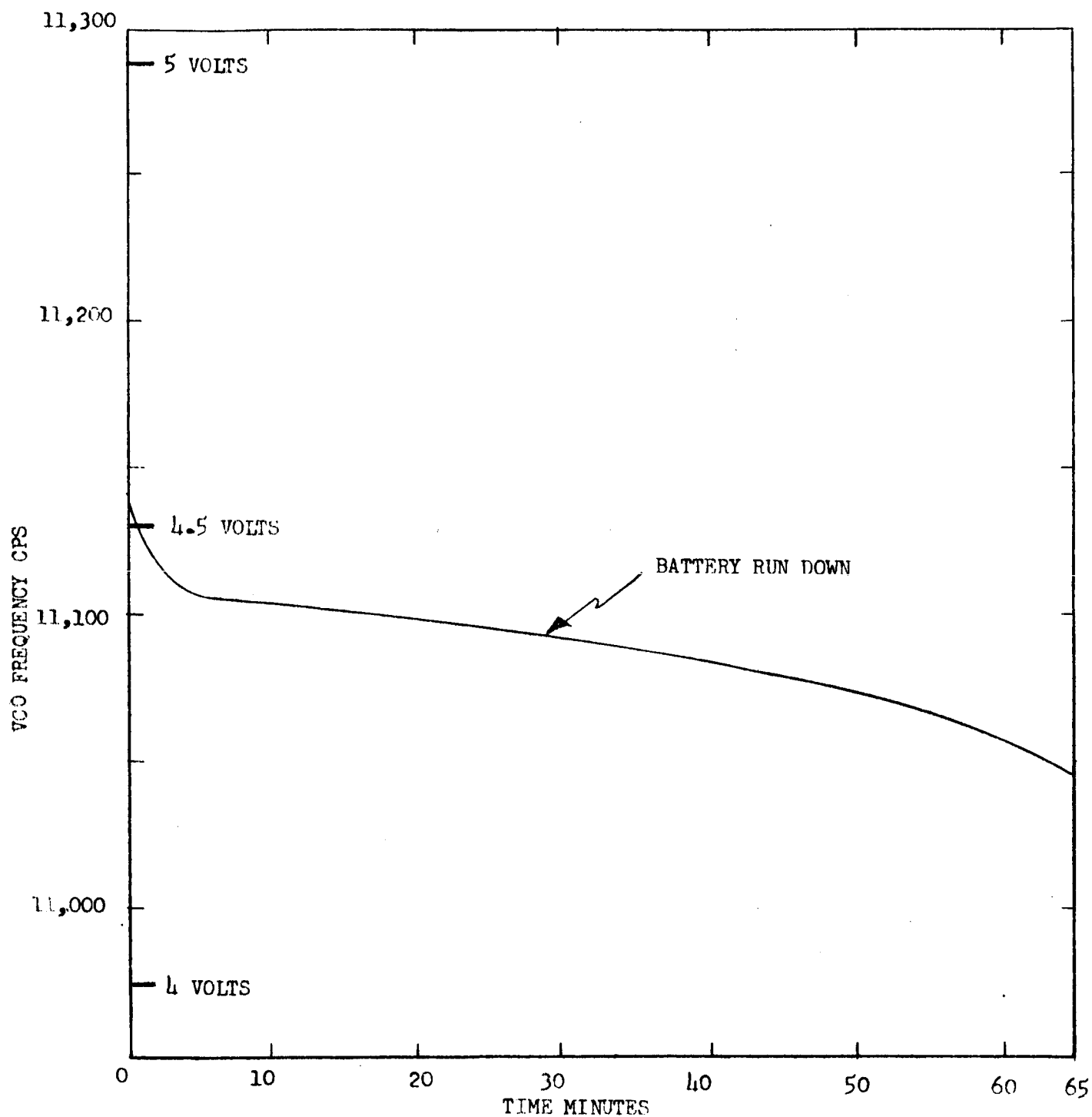
2. Photomultiplier tubes. Two photomultiplier tubes failed during vibration testing of detectors. The cause of failure was fatigue and fracture of poorly welded connections. The correction of this problem was to minimize the duration of vibration testing and inspect welds visually and reject those tubes which appear substandard.

3. Scintillation crystal. The scintillation crystals fractured when the detector was subjected to vibration testing. The cause of this was inadequate ruggedness of the crystal assembly and a severe resonance in the detector housing. The solution to this problem was accomplished by purchasing a more rugged crystal assembly from a different vendor and by strengthening and increasing the damping of the detector housing by redesigning with fiberglass. The detector housing redesign was accomplished by NASA, LRC, personnel.



THERMISTOR TEMPERATURE SENSOR
CALIBRATION

FIGURE 30



TEST VOLTAGE CALIBRATION
TELEMETER CHANNEL 12

FIGURE 31

TABLE II
ENVIRONMENTAL TESTING SUMMARY

ITEM	Temp. Deg. C	Accel g's	Vibration ± g Peak	Shock g's 11ms	Vacuum Feet Alt.	NOTES
<u>Qualification Testing</u>						
Detector Assy #1	0° + 60°	95	20	60	---	Failure of PM Tube in vibration.
Detector Assy #2	0° + 60°	95	20	60	---	Success with PM Tube. Failure of crystal under vibration.
Signal Conditioning Electronics	-55° + 70°	95	20	60	---	
Power Supply	-55° + 70°	95	20	60	---	
Battery Pack	0° + 60°	95	20	60	---	Failed in vibration. Changed potting and repeated successfully.
Accelerometer	---	95	20	60	---	
Relays	---	95	20	60	---	
<u>Flight Component Testing</u>						
Transmitter	---	65	14	60	---	
SCO's	0° + 60°	---	14	---	---	
Signal Conditioning Electronics	-55° + 70°	95*	20*	60*	---	* Selected
Battery Pack	0° + 60°	---	---	---	---	
Power Supply	-55° + 70°	95	20	60	---	
<u>Flight Assurance Testing</u>						
Complete Flight Payload	0° + 60°	---	5	30	375,000	Appendix III

4. Transmitter. Both the flight transmitter and spare transmitter failed during vibration testing. Repairs were effected by the vendor and the transmitters passed all tests. Evaluation of the transmitters was done at NASA, LRC.

5. Structure. A prototype payload internal structure was tested under vibration and found to have a severe resonance having a very high amplification at the detector. Bakelite blocks were installed to strengthen and damp some flanges. Also the forward end of the internal structure was supported by the external structure through a preloaded pad of damping material. This structural testing and modification was done at NASA, LRC. These changes along with a reduction in the required vibration test levels to more realistic values allowed the completed payload to survive flight readiness tests.

The final payload flight readiness test data is contained in Appendix III.

4.3 Flight test. Upon completion of flight readiness testing the payload was transferred to Wallops Island, Virginia, for spin balancing, launcher checkout, and flight tests. The payload was assembled to the Apache booster and spun in roll at the dynamic balance facility. The required balance weights were determined and installed in the payload.

The payload and umbilical cable were checked out in the launch area and data examined as received by the Wallops telemetry station. Proper operation of the payload and interfaces was verified. The payload was illuminated by the FSP-16, SPANDAR, and MIT tracking radars in turn to determine payload susceptibility to the high radiation field. The SPANDAR radar caused RF noise trouble and was subsequently held off of the payload during the first 50K feet of flight.

Figure 32 is a photograph of the vehicle on the launcher. Figures 33, and 34 show the payload in its flight configuration prior to assembly with the Apache and skin sections. Figure 35 shows a dummy source and nose piece.

Flight test of the Air Density Sensor payload was accomplished on December 17, 1963, from Wallops Island, Virginia. The Nike-Apache boost system carried the payload to an altitude of 422,000 feet and subsequent impact at a range of 431,000 feet.

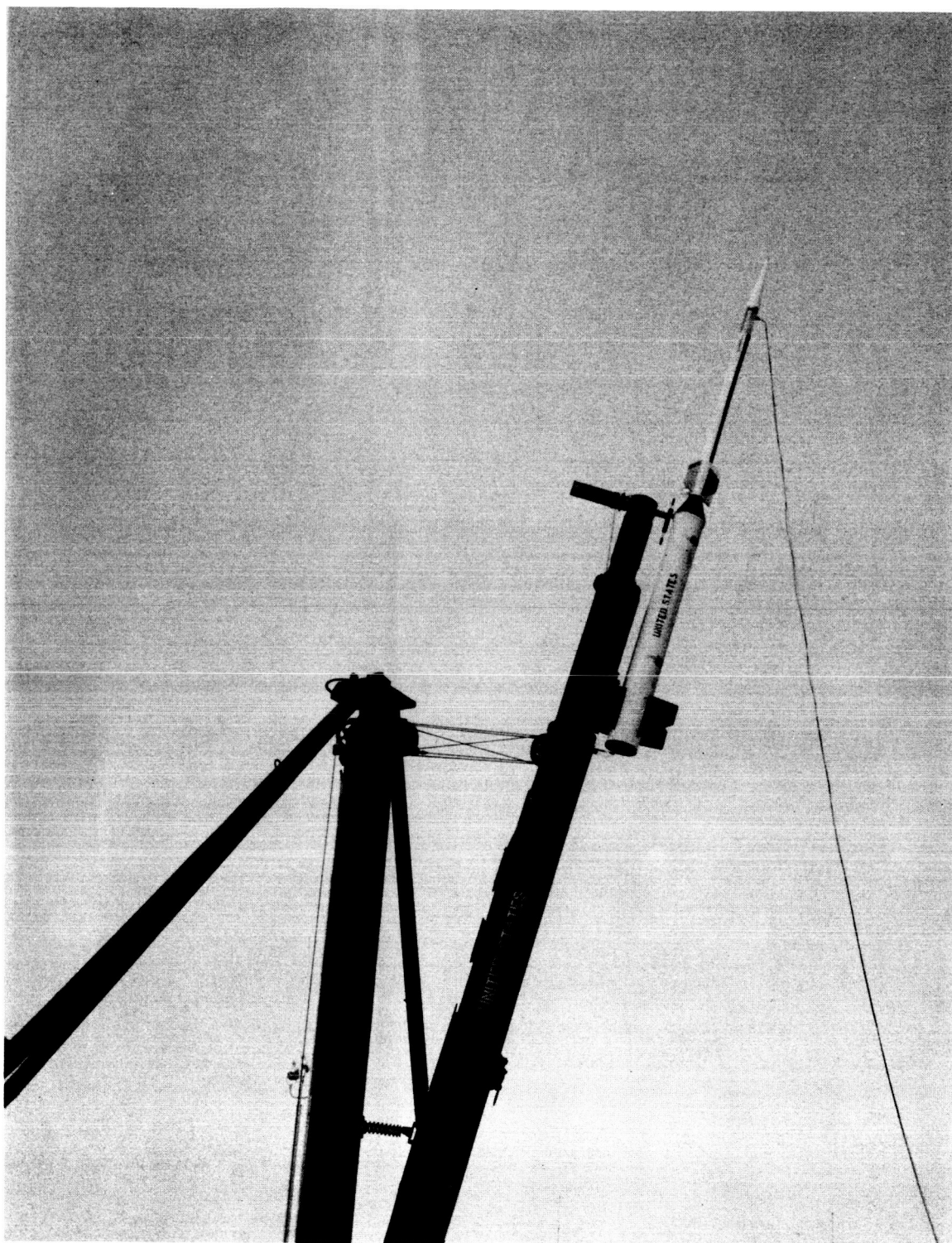


FIGURE 32
NIKE-APACHE ON LAUNCHER

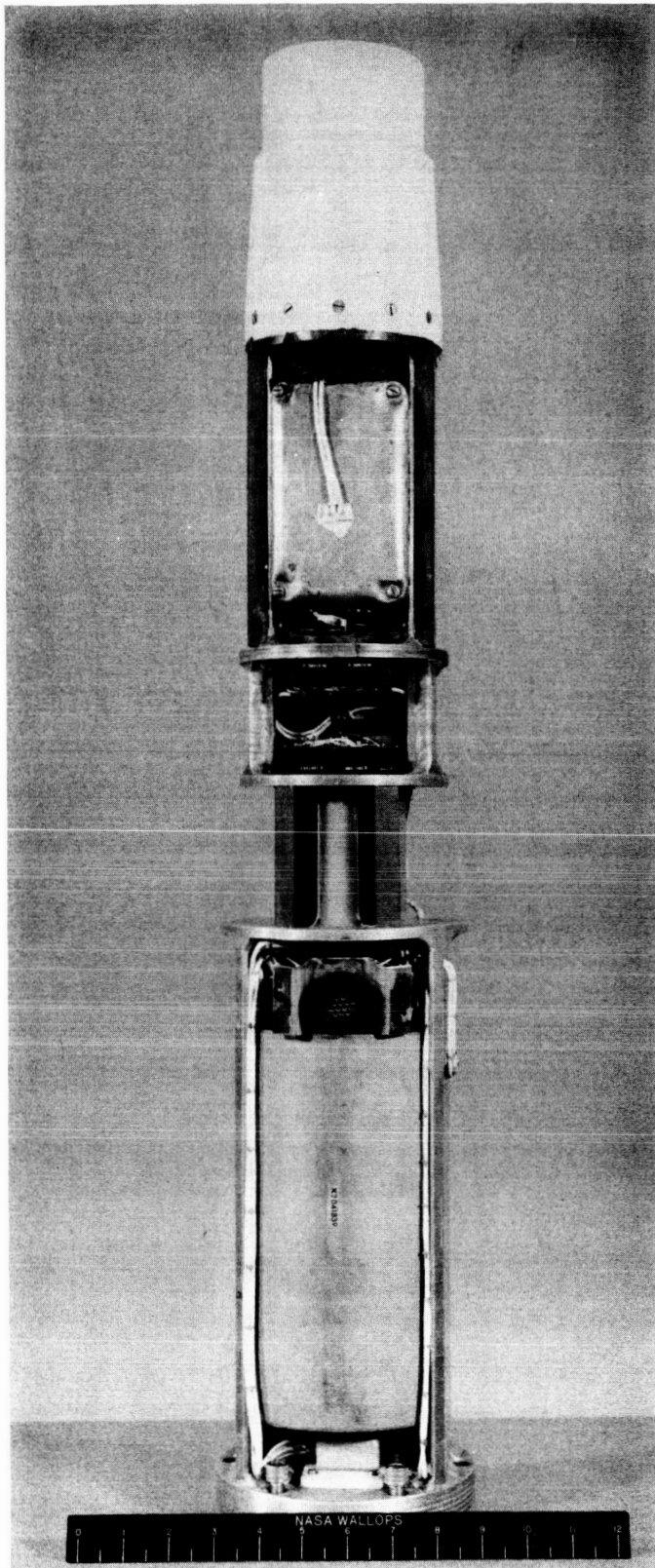


FIGURE 33
AIR DENSITY SENSOR FLIGHT UNIT

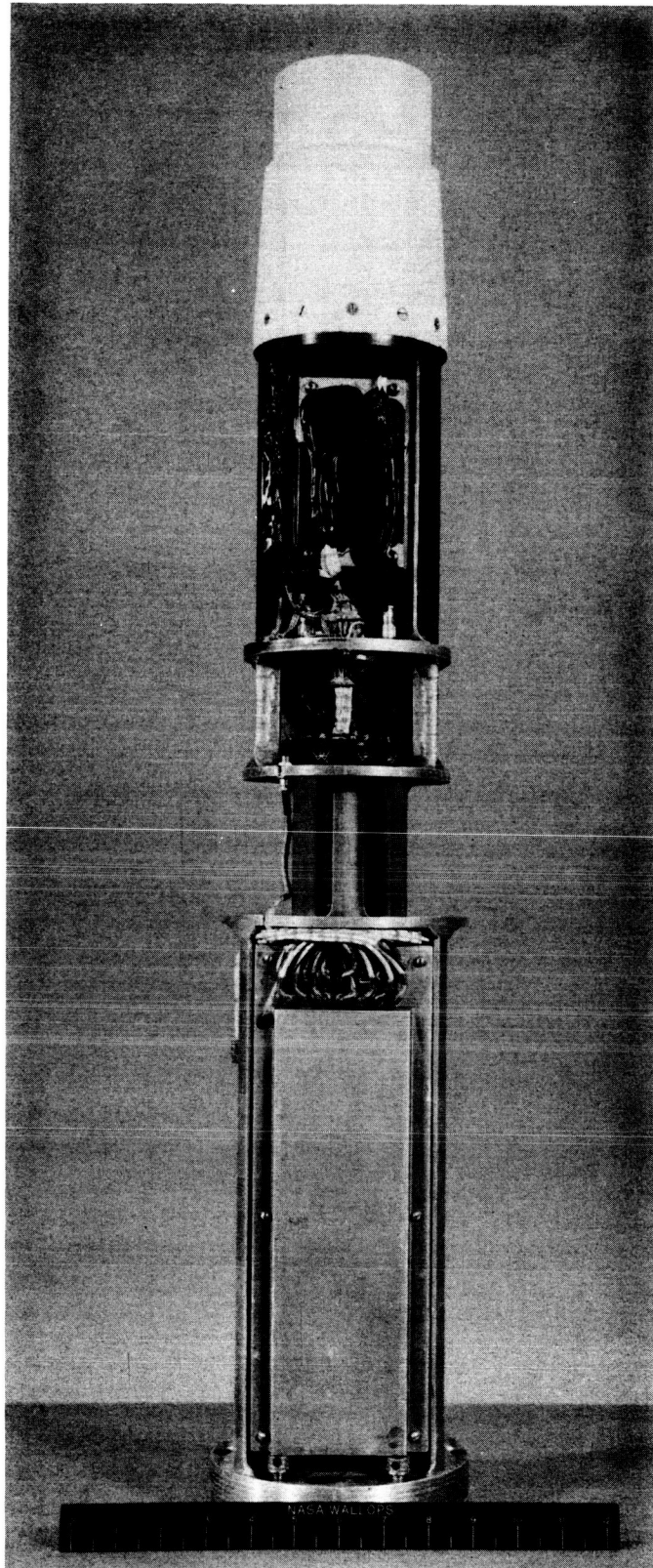


FIGURE 34
AIR DENSITY SENSOR FLIGHT UNIT

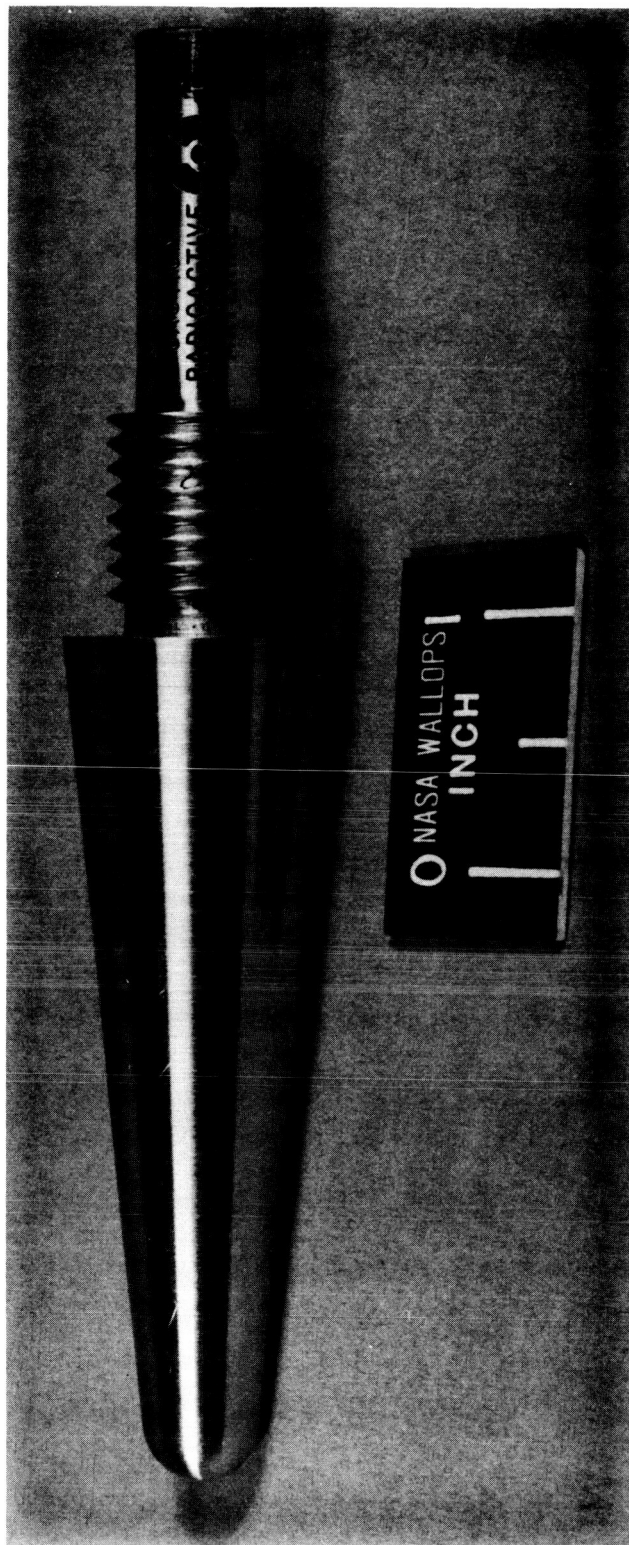


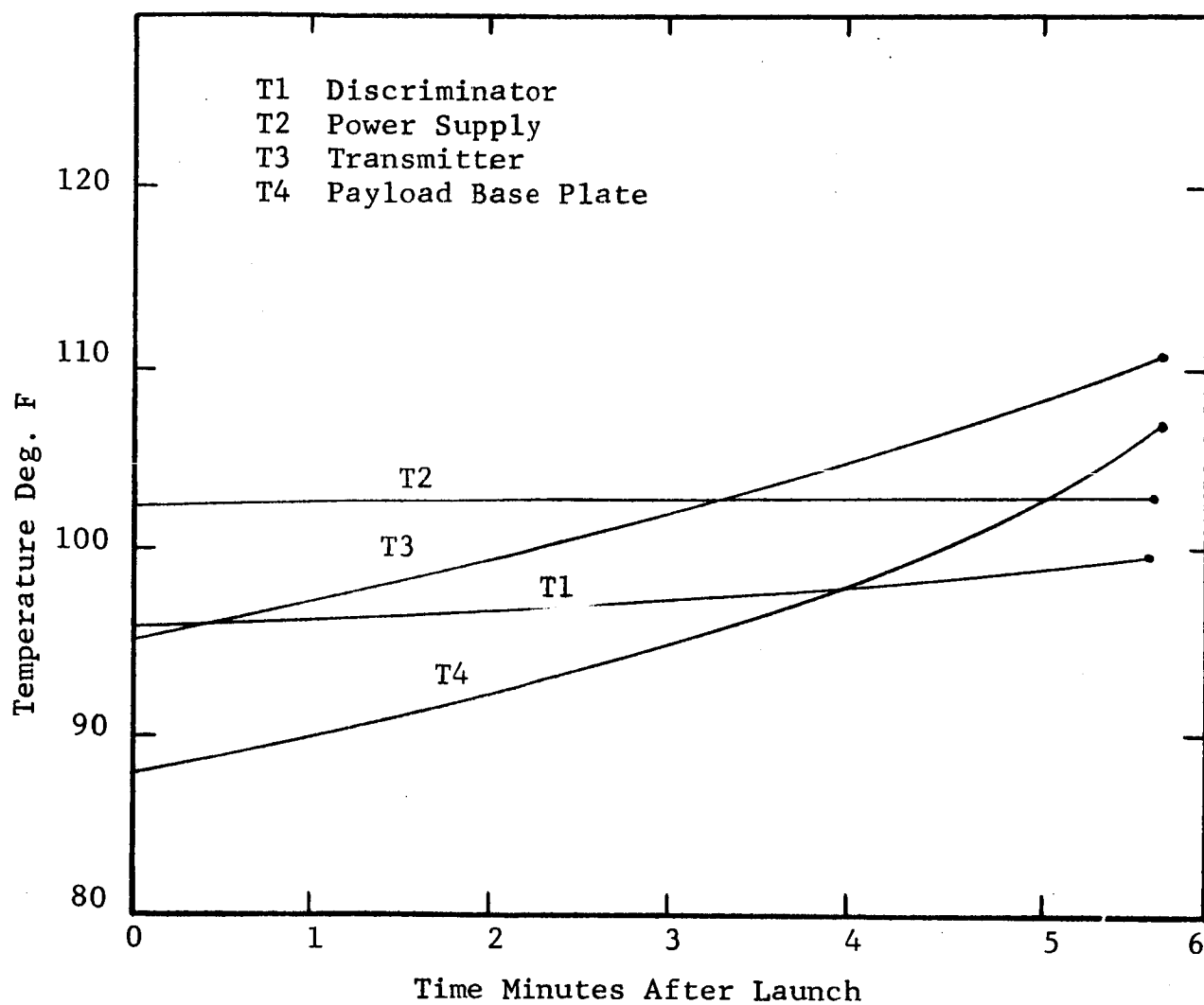
FIGURE 35
DUMMY SOURCE

The impact coordinates are $37^{\circ}22'N$ latitude and $74^{\circ}5'W$ longitude. At this point the water depth was 5,500 feet insuring no accidental recovery of the radioisotope source. Telemeter data was received from launch until impact, a total flight duration of 345 seconds. From the telemeter signal strength records it was determined that the Apache attained the proper spin rate without instability and maintained an adequate spin rate throughout the flight (approximately 5 rps).

The telemetered temperature data is shown plotted in Figure 36. The temperature measurements showed proper warm-up and stabilization of the sensor electronics and little temperature rise throughout the flight. The largest heat input was through the Apache head cap resulting in a $19^{\circ}F$ temperature rise at this point. The detector and discriminator temperature rise throughout the flight was only $4^{\circ}F$. Acceleration measurements indicated a proper boost profile. The test signal indicated proper battery voltage throughout the flight, showing adequate power with no intermittent fluctuations.

The density sensor data is tabulated in Appendix IV. Listed in Section A are the number of pulses received in each one-second averaging interval throughout the flight from telemeter channels E, C, and 14. The elapsed time is given to the end of each averaging period. The altitude as measured by tracking radar is tabulated for each time. Also given is the altitude at the mid-point of each averaging interval. This data, count rate versus altitude, is shown plotted in Figure 37. The channel 14 ascent data shows a region where the output of detector #1 contained a large noise component or maintained a large sensitivity shift. This malfunction occurred for the first 60 seconds of flight to an altitude of about 200 K feet, whereupon the malfunction disappeared and proper data was obtained throughout the remainder of the flight.

The other curves show good data relating to density fading into a constant background level at the higher altitudes. Notice that the background levels reached differ in channels C and E or detectors 1 and 2. This is not correct indicating possibly that the channel E inhibit circuitry was not operating properly.



AUXILIARY TELEMETER DATA

FIGURE 36

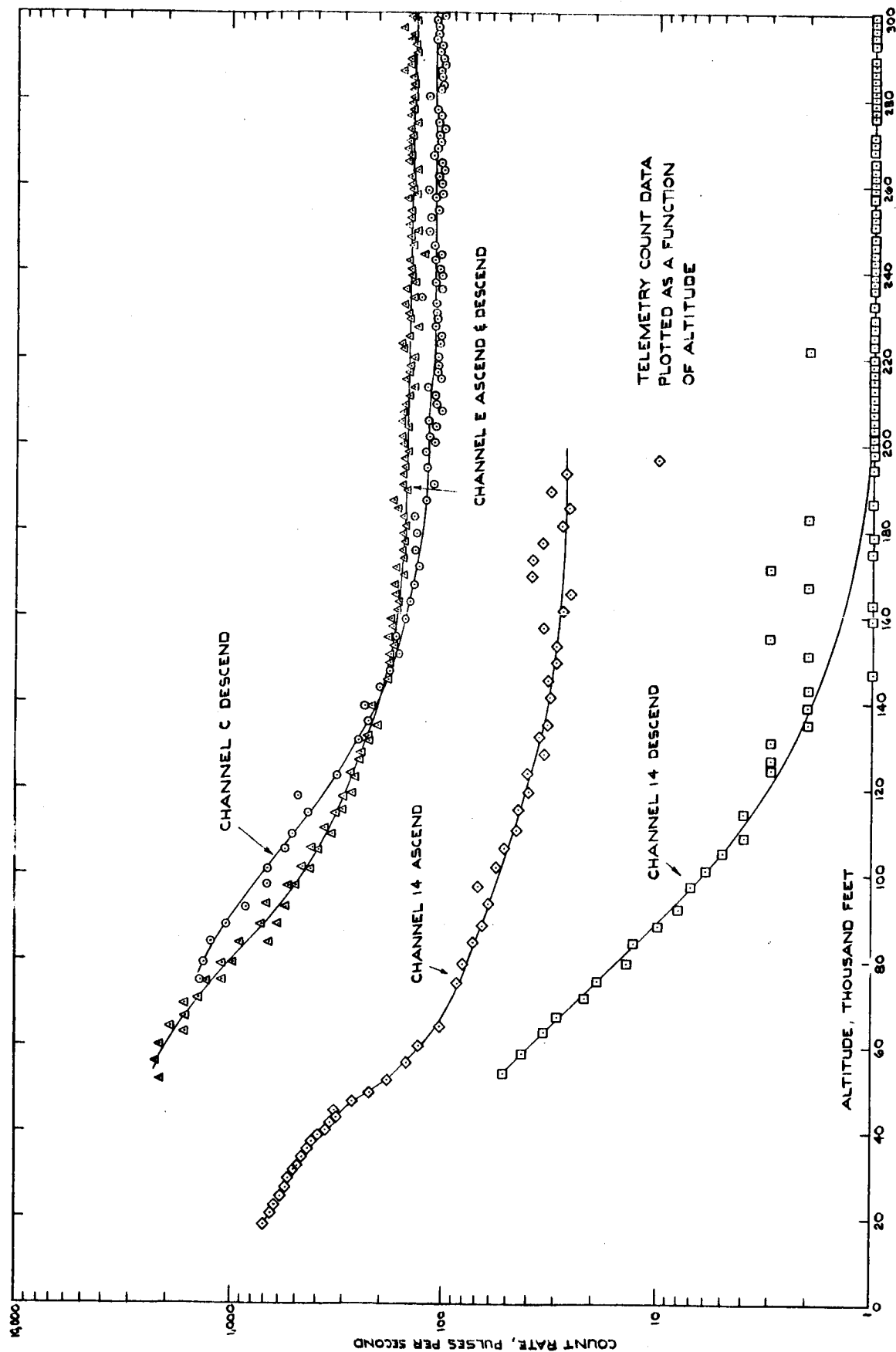


FIGURE 37. TELEMETRY COUNT DATA PLOTTED AS A FUNCTION OF ALTITUDE

Listed in Section B of Appendix IV is the number of pulses in each one-second averaging interval related back to the detectors. Subtracted from this data is the nominal background level as determined by averaging the count rate over the long constant periods at apogee. This data is shown plotted in Figures 38 and 39. The solid line superimposed over the data points is the density profile from the 1962 standard atmospheric tables adjusted by the sensor calibration data.

Listed in Section C of Appendix IV are the number of pulses detected in 10 second averaging intervals. Again the background has been subtracted from each data point. The time listed with each point is the time at the end of the averaging interval. The altitude listed at each point is the altitude at the center of the averaging interval. This data is plotted in Figures 40 and 41.

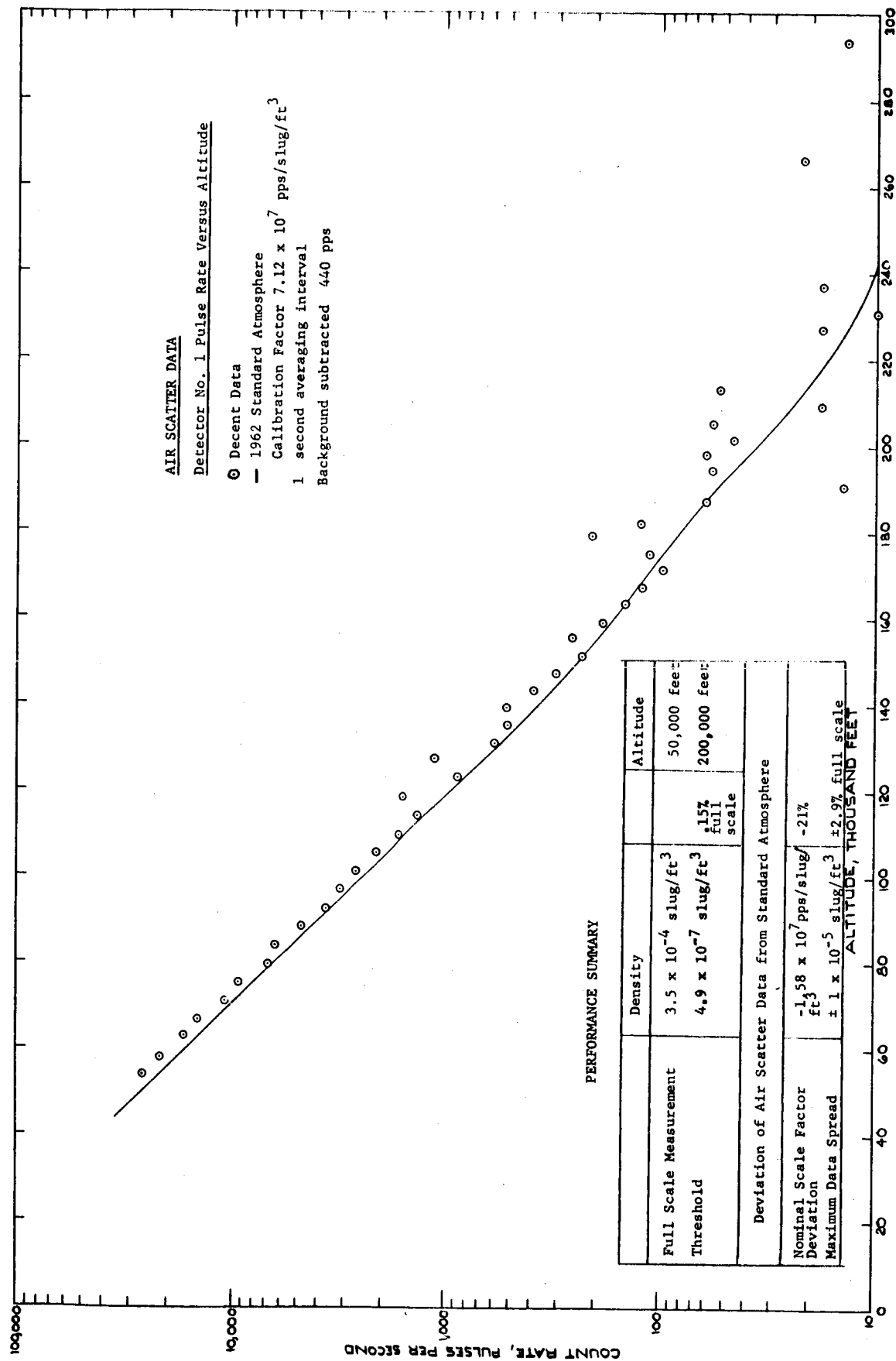


FIGURE 38. AIR SCATTER DATA, DETECTOR #1

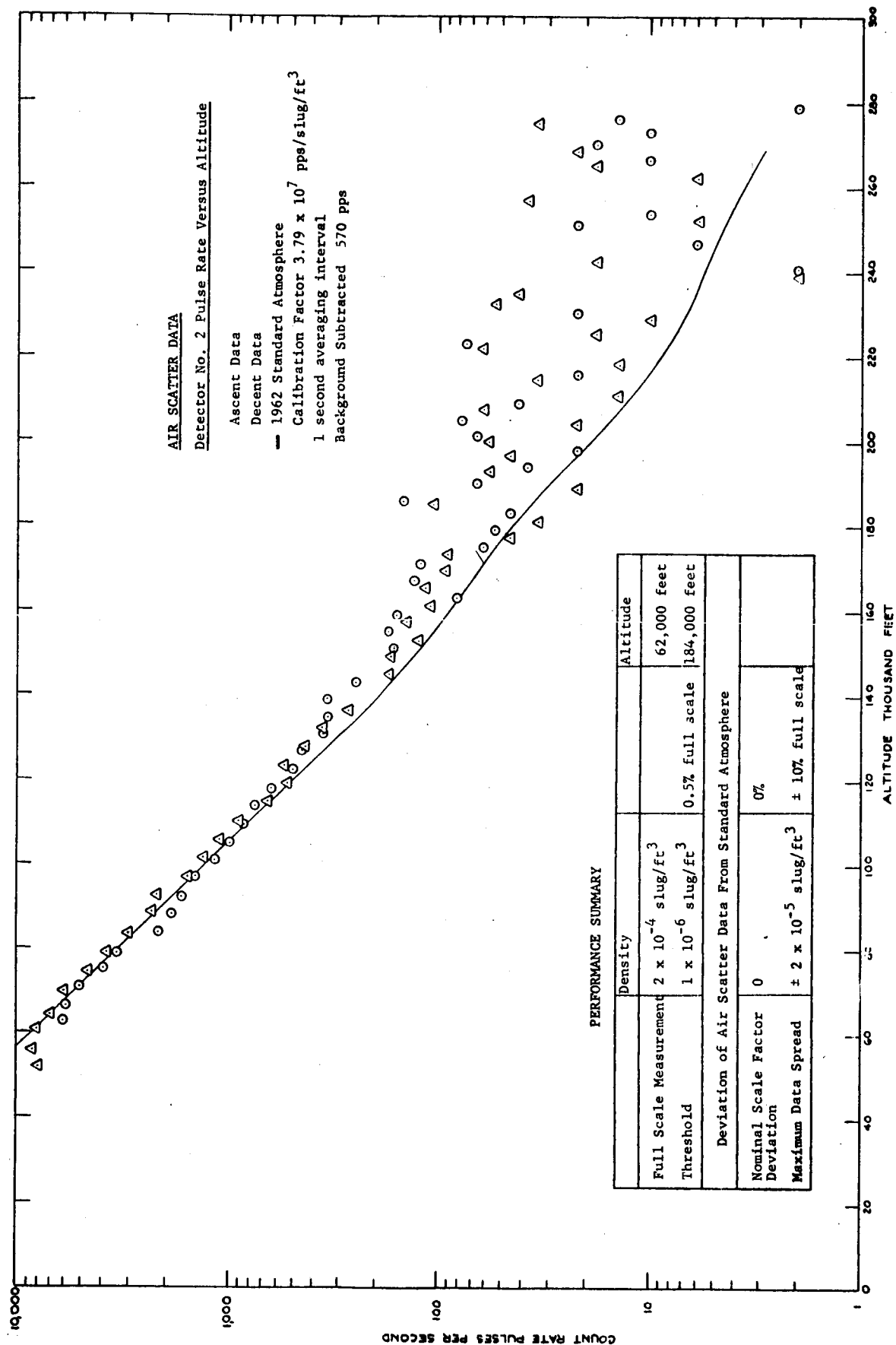


FIGURE 39. AIR SCATTER DATA, DETECTOR #2

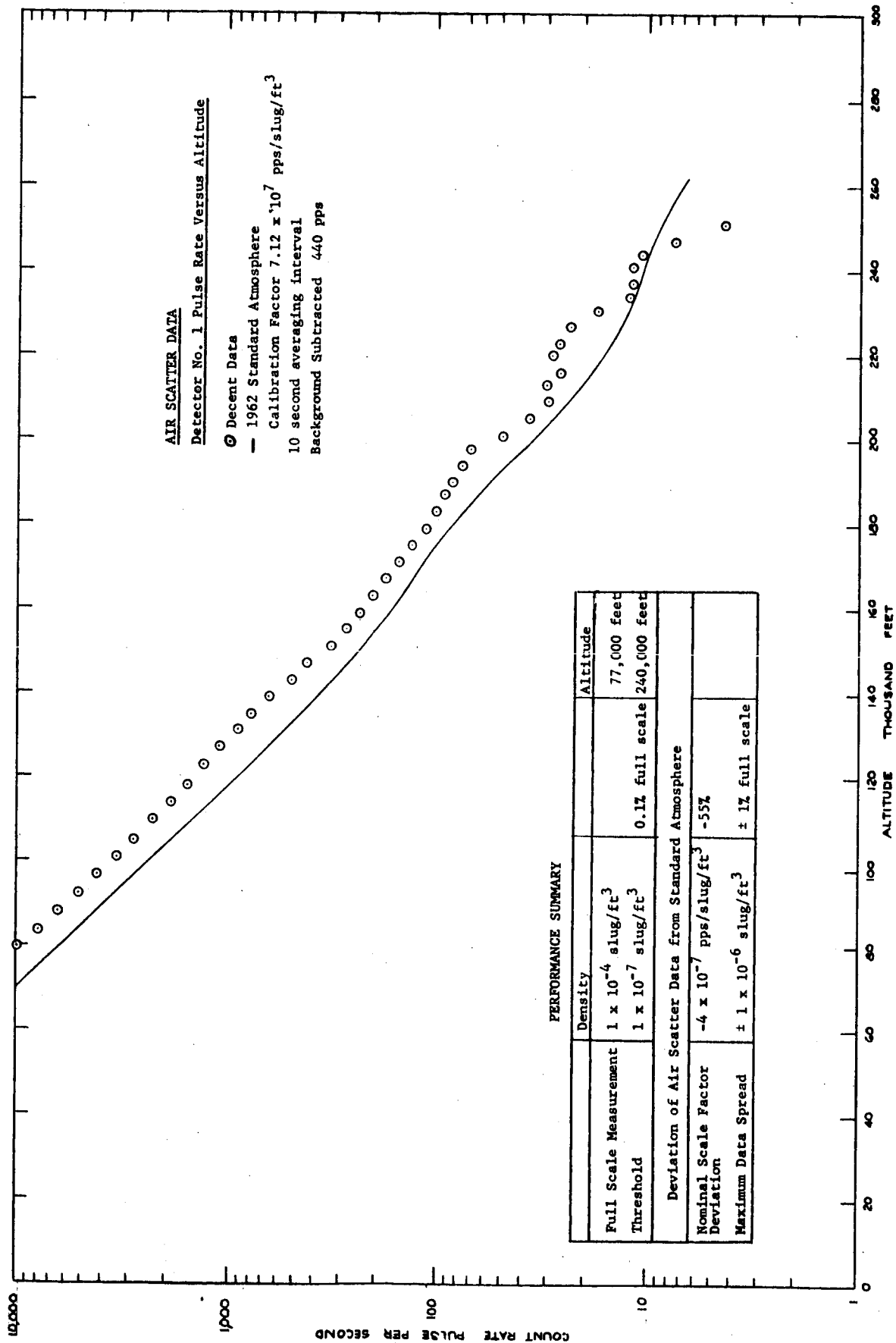


FIGURE 40. AIR SCATTER DATA, DETECTOR #1

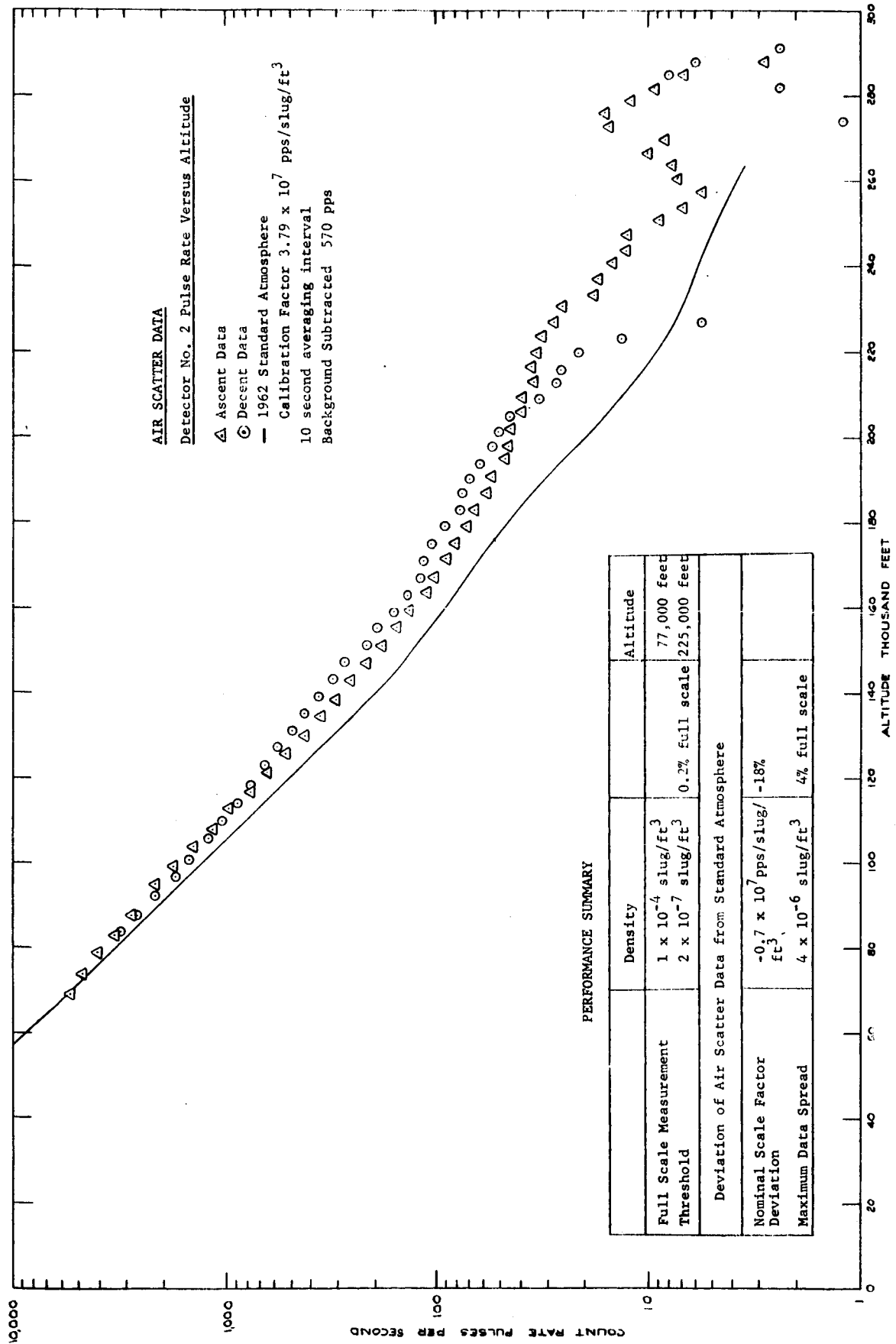


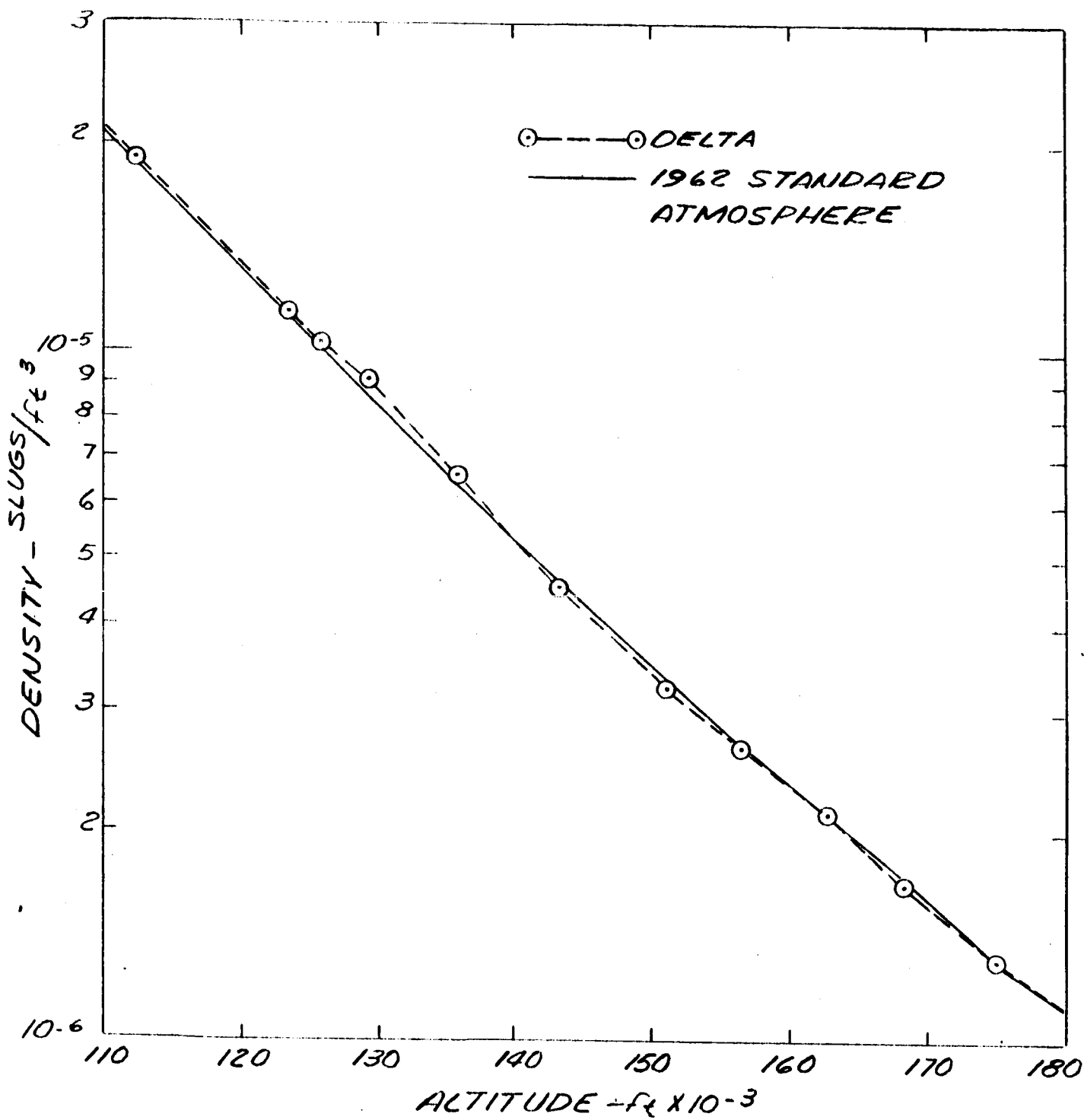
FIGURE 41. AIR SCATTER DATA, DETECTOR #2

4.4 System Accuracy - The accuracy of the air density measurement is discussed in this section by comparison with the 1962 standard atmosphere profile and meteorological measurements taken before and after the experiment. The meteorological data is shown in Figures 42 and 43. These measurements cover a range of altitude from 40,000 to 180,000 feet and indicate that the atmospheric density over this range was within $\pm 5\%$ of the standard. Since the meteorological measurement accuracy is of this order the standard atmospheric profile can be considered the best reference available for comparison of the experimental data. Figures 38, 39, 40 and 41 show that the flight data compares favorably with the standard atmospheric density profile throughout a significant portion of the measurement range.

4.4.1 Measurement Range - The measurement range attained by the sensor was limited at the high density low altitude end by the telemetry bandwidth associated with the data channel for detector #2 and a region of discrepant data at low altitudes from detector #1. As is indicated by the pulse rate versus altitude data of Figure 38, the high density limit of the measurement occurred at about 50,000 feet or a density of 3.5×10^{-4} slugs/ft³. The low density limit or threshold of the sensor is established by the background radiation level. Figure 37 illustrates the air scattered radiation level dropping into the background radiation level. The measured background is subtracted from total signal plus background giving a valid measure of air scattered radiation until the statistical validity of this difference becomes questionable. The data shown in Figure 38 becomes uncertain at about 200,000 feet altitude where the density is about 4.9×10^{-7} slug/ft³. With the one second averaging interval the number of air scattered counts expected at this altitude is about 35 and the background 440 for a total signal of 475 ± 22 pulses. Subtracting the measured background from this total signal gives 35 ± 22 pulses. This is the expected 1 sigma spread of data at this altitude agreeing quite well with the actual spread shown in Figure 38. The most probable error, $.675\sigma$, at this altitude is

$$P.E. = .675 \times 22 = 15 \text{ pulses}$$

This is about 50% of the expected reading. At higher altitudes, lower densities, the data of Figure 38 spreads rapidly. Although information relating to density is apparent at these lower densities its uncertainty is high. It is this point



METEOROLOGICAL SOUNDING DATA

FIG. 42.

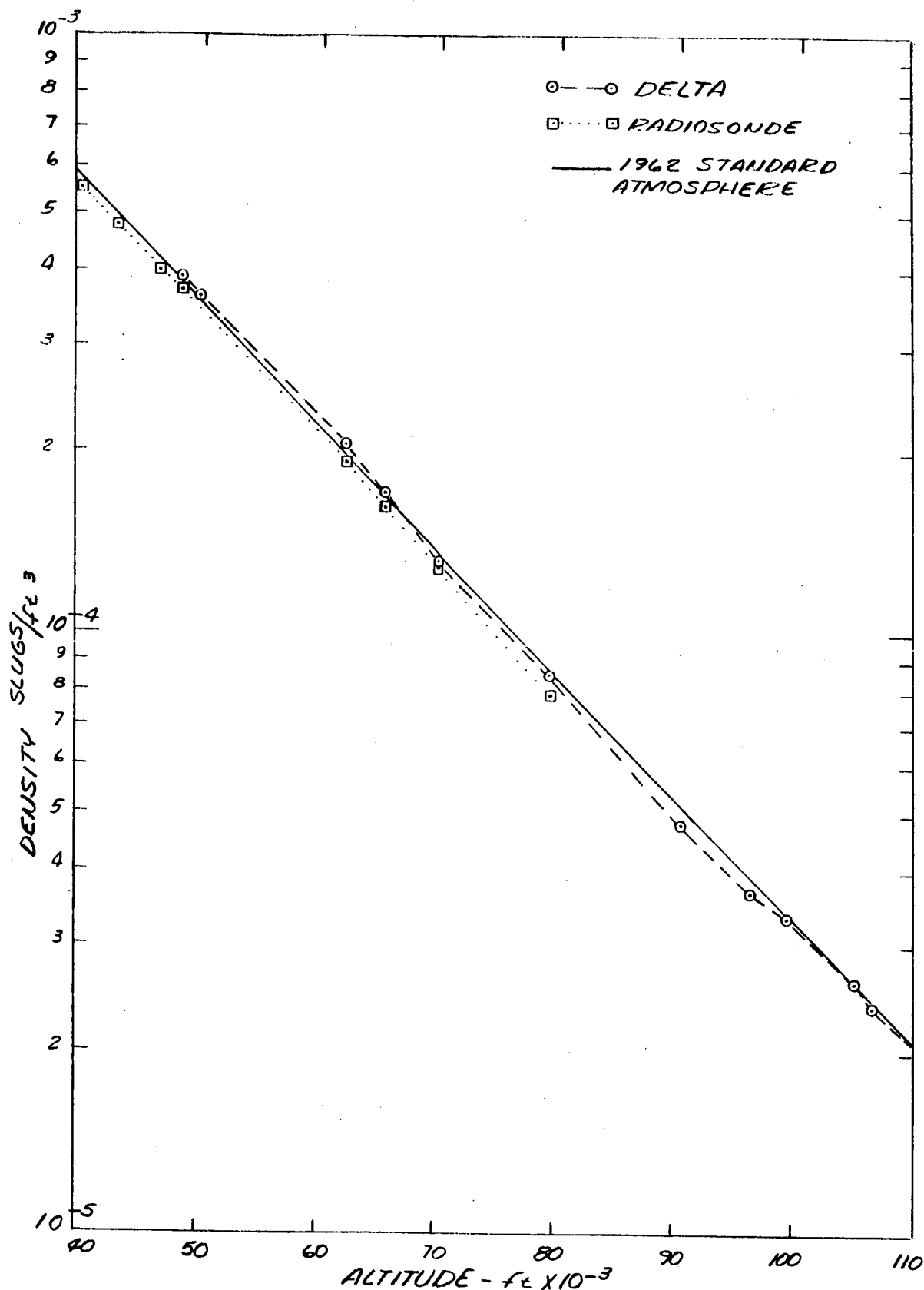


Figure 43. METEOROLOGICAL SOUNDING DATA

where the most probable error is 50% of the reading that will be considered the "threshold" of the measurement. For the data of Figure 38 this threshold is about 0.15% of the full scale measurement.

The data measured by detector #2 shown in Figure 39 has a full scale range of 2×10^{-4} slug/ft³ at 62,000 feet altitude and a threshold of 1×10^{-6} slug/ft³ at 184,000 feet or about 0.5% of full scale. The air scatter sensitivity of this detector is half that of detector #1 while the background level measured was higher. These factors contributed to an increased threshold in this measurement. Again the threshold is the point where the most probable error is about 50% of the reading. With the one second averaging interval the number of air scattered counts expected at 184,000 feet is 40 and the background 570 for a total of 610 ± 25 pulses. Subtracting the expected background gives 40 ± 25 pulses. The probable error is thus

$$P.E. = \frac{.675 \times 25 \times 100}{40} = 42\%$$

By increasing the averaging interval from 1 to 10 seconds the uncertainty due to randomness of the photon emission is reduced. This is illustrated in Figures 40 and 41, where the 10 second averages of count rate are plotted every second.

The measurement range is increased to lower densities and higher altitudes. The data from detector #1 shown in Figure 40 has a threshold of about 1×10^{-7} slug/ft³ and detector #2 in Figure 41 a threshold of about 2×10^{-7} slug/ft³ at about 240,000 feet and 225,000 feet altitudes respectively. At these altitudes the most probable error for the 10 second averaging interval is again approximately 50% of reading and 0.2% of full scale.

These altitude limits are somewhat lower than was anticipated due to a large cosmic background level. The anticipated background level for a 2 inch diameter, 2 inch long NaI (Tl) detector is shown in Figure 44. In the 90 to 150 Kev window this is 30 pulses per second. For the 4 inch diameter flight detector this would be approximately 60 pulses per second. The actual level detected was 440 pulses per second, about 7.5 times greater. This possibly was the result of the large mass of lead located near the detector degrading a portion of the high energy primary radiation into secondary radiation in the energy vicinity of the

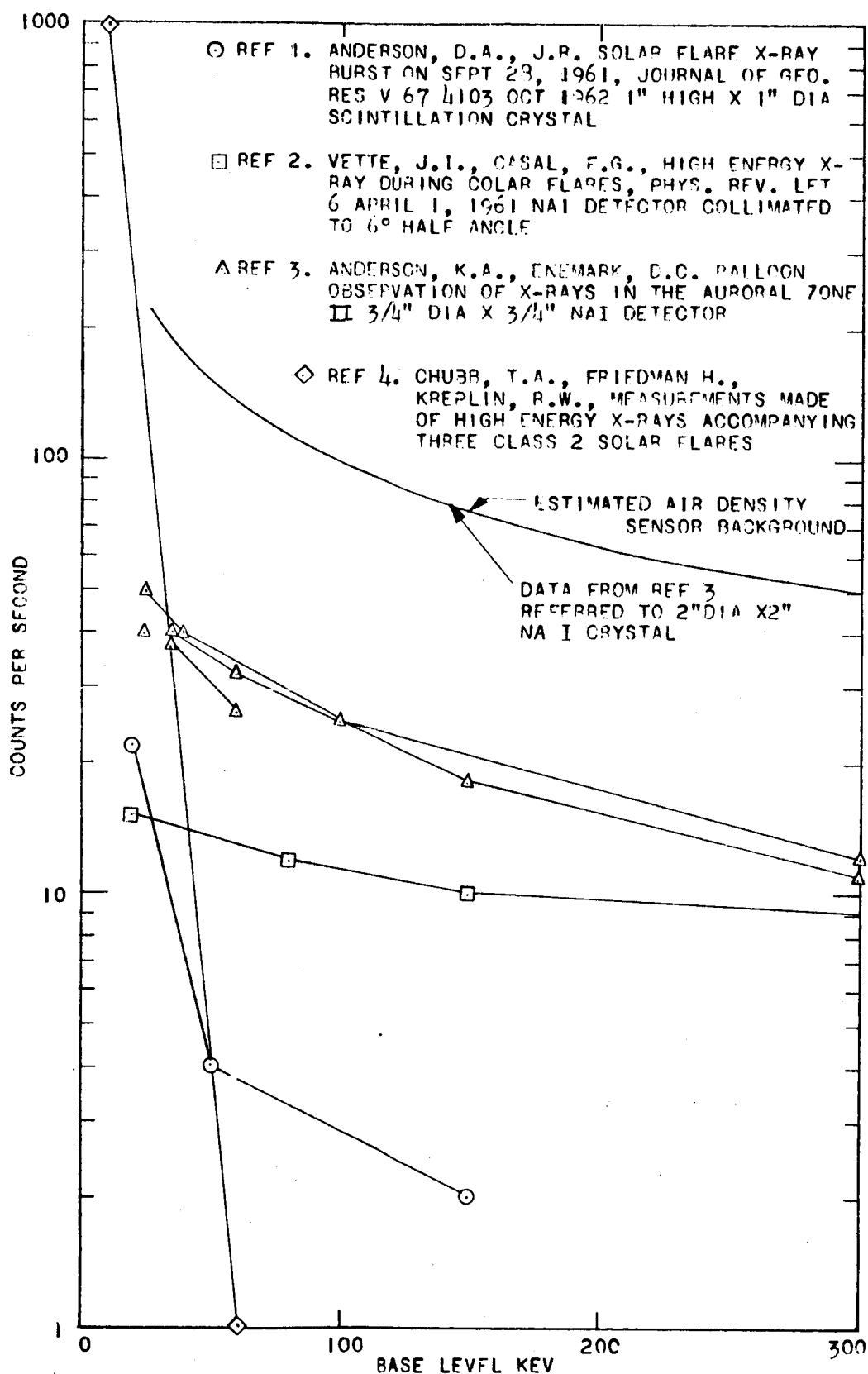


Figure 44. INTEGRAL SPECTRUM, COSMIC BACKGROUND DATA

discriminator window. Another possibility, however unlikely, is that a portion of the measured background is direct transmission of the source radiation through the 15 inches of lead shielding.

4.4.2 Altitude Correlation - The altitude correlation of this data is obtained from tracking radar. The actual radar accuracies are of the order of 0.2% and resolution of the read-out points 500 feet. For a one second data averaging interval the altitude change over the interval is about 5,000 feet. At 200,000 feet altitude this corresponds to a 20% change in density. By plotting the density data at the altitude corresponding to the center of the averaging interval this change in altitude is averaged out. The overall uncertainty is then only due to the non-linear variation of density with altitude and change in vertical velocity over the interval. This amounts to a density error of 1.25%.

The 10 second data is seen to deviate more from the nominal scale factor since the deviation from a linear change in density is greater over 10 seconds than one.

4.4.3 Flow Fields - The effect of variations of the aerodynamic flow fields on the measurement appear to be small. No gross errors are apparent in the decending data where the Apache booster and payload turned over and tumbled for several seconds. The telemeter signal strength plot indicated turn over to occur at about 255,000 feet altitude and tumbling and irregular flight occurred down to about 110,000 feet. The effect of a shock layer in normal flight was determined analytically to be small. Referring to equation 10 of section 3.1 the detected air scattered radiation from a differential conical section with the apex at the nose piece and with a half angle θ is given as

$$I_{D1} = \frac{3I_o A_D K \rho}{16r} \int (1 + \cos \theta) \sin \theta d\theta \quad (20)$$

This expression was integrated from 0 to π radians giving the total scatter from the air surrounding the vehicle. For the purpose of determining effects of the shock layer this expression can be integrated from 0 to θ_M the expected Mach angle giving the portion of air scatter within the shock layer. This expression computed with the density within the shock layer gives the expected error. At Mach 5 the shock makes an angle of 8 degrees with the skin and the density ratio across the shock is $\frac{\rho}{\rho_\infty} = 1.25$.

Integrating Equation 20 from 0 to 8° gives the increment:

$$\Delta I_{D1} = \frac{3I_o A_D K \rho \cdot .017}{16r}$$

from Equation 11 the total scatter is

$$I_{D1} = \frac{3I_o A_D K \rho_\infty^2}{16r}$$

The fractional error is thus

$$\frac{\Delta I_{D1}}{I_{D1}} = \frac{\rho}{\rho_\infty} \times \frac{.017}{2} = 1.25 \times \frac{.017}{2} = .0106$$

or about 1% error. At lower Mach numbers more of the scattering volume is within the shock layer but the density rise is less significant. The resultant error is less at lower Mach numbers.

4.4.4 Calibration - The density calibration of the sensor as measured in the altitude sphere is shown in Figure 28. For detector #1 the scale factor is 5.51×10^5 pps/slug/ft³. For detector #2 the scale factor is 2.93×10^5 pps/slug/ft³. These scale factors are determined with the test source of 0.394 curie strength.

The flight source on the day of the launch was 21.4 curies. The scale factors are thus increased by the ratio of source strengths to 2.99×10^7 pps/slug/ft³ and 1.59×10^7 pps/slug/ft³ for detectors 1 and 2 respectively. The source strengths given above were determined from manufacturers data. The flight test results show considerable disagreement with these scale factors and looking back at some of the source and detector calibration data it is evident that the test source was not up to strength. From the inverse square calibration data of Figure 26 and applying absorption and abundance corrections as in section 3.2.1 the measured strength of the test source was found to be only 42% of the expected strength.

Using the measured value of strength for the test source increases the scale factor calibration on the launch day to 7.12×10^7 pps/slug/ft³ and 3.79×10^7 pps/slug/ft³ for detectors 1 and 2 respectively. These are the calibration factors used to show data correlation with the standard atmosphere profile. Referring to Figures 38 and 39 the flight data from detector #1 appears to be 21% high and that of detector #2 falls closely about the nominal calibrations referred to the standard atmosphere. This agreement is better than might be expected but certainly within the realm of probability considering the tentative nature of the calibration procedure.

4.4.5 Accuracy Summary - The total data of detectors 1 and 2 is summed together and plotted in Figure 45 for the decent portion of the flight. The one second data is shown at low altitudes and the 10 second data is shown at the high altitudes. A good measure of density is shown from 62,000 feet to 225,000 feet altitude over a density range of 2×10^{-4} to 2×10^{-7} slug/ft³ or three orders of magnitude. Over this range the measured density correlated with the meteorological sounding data and with the 1962 standard atmosphere showing a scale factor 8% high and a maximum data spread of $\pm 2.5\%$ of full scale.

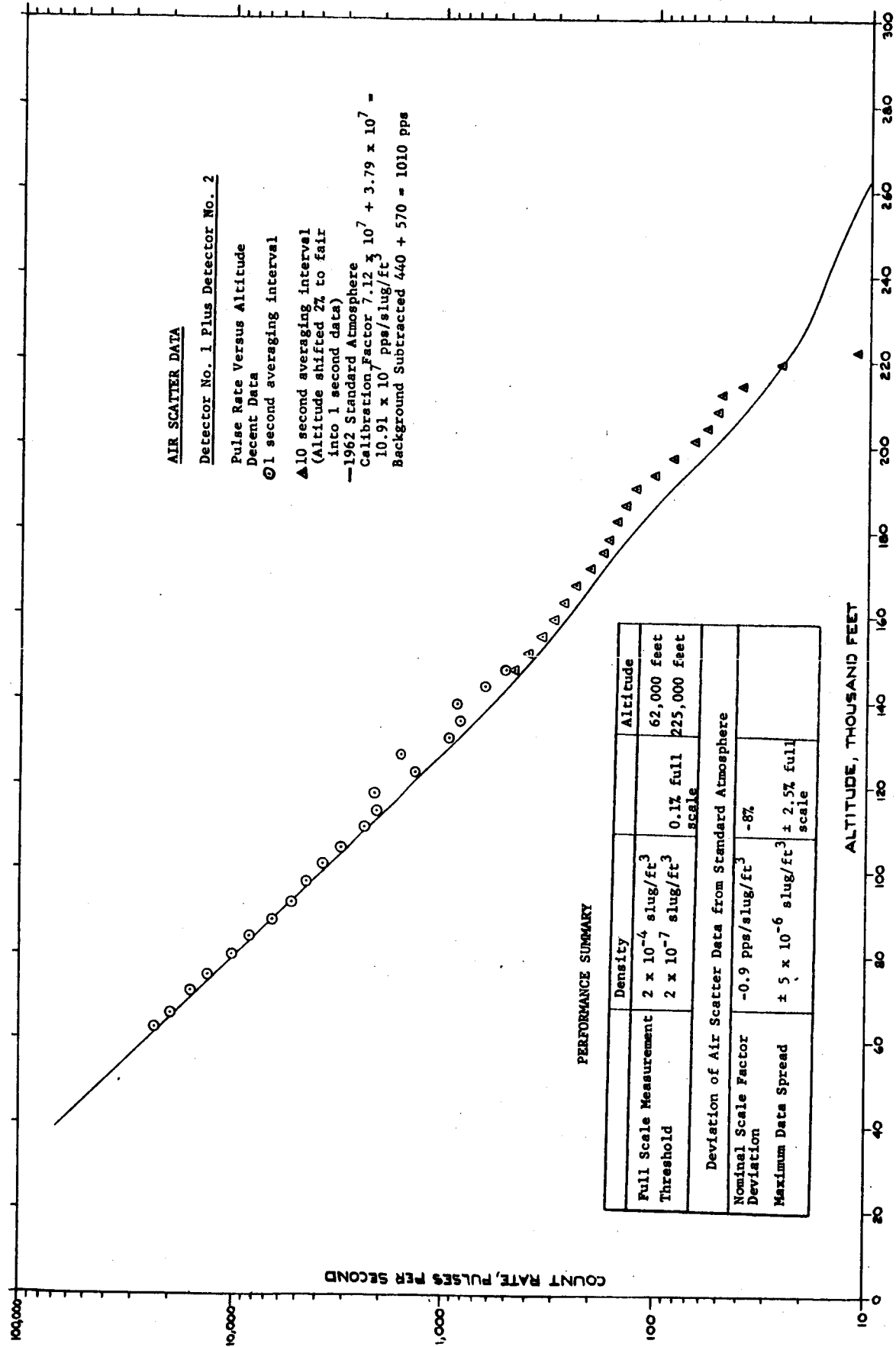


FIGURE 45. AIR SCATTER DATA

5.0 SOURCE HANDLING ASPECTS

The radioactive source used in this density measurement experiment was 25 curies of Cerium 144. This source is of such a level as to require care in its handling and storage. Personnel at Giannini Controls Corporation were licensed by the U.S. Atomic Energy Commission to possess and bear the responsibility for its proper and safe use. Procedures for safe handling and storage were established by Giannini Controls Corporation and approved by the AEC. Additional precautions were exercised by the Wallops Island range safety office to minimize the possibility of occurrence of any dangerous incident. A brief summary of the major procedures followed is given below.

The Cerium-144 was doubly encapsulated in welded stainless steel capsules and leak tested by Oak Ridge National Laboratories. This source was mounted in the nose piece and shipped to Wallops Station in an approved shipping container for storage in a remote bunker.

On the launch date the source in its shielding container was trucked to the launch site. After all preliminary checks of the payload were complete the launch area was cleared to a distance of 100 feet. Two radioisotope technicians performed the installation procedure. The first technician unlocked and opened the shielded container and removed the source and nose tip with a pair of 6 foot niptongs. The second technician gripped the nose tip with a specially designed 8 foot long pair of tongs and carried it a few steps to the nose of the rocket. The Nike-Apache rocket was mounted on the launcher in a horizontal position 6 feet above the ground. The second technician mounted a step ladder and lowered the source and handling tool into a V shaped locating box propped at the nose of the rocket. This box contained a lead liner providing some additional shielding. The source and nose piece were then inserted in the nose and screwed tight. The handling tool was released and the two technicians left the area. Motion picture coverage provides a record of this operation. Pocket dosimeters and film badges monitored the dose received during the operation. The first technician received a dose of 20 mr and the second 10 mr, well within the desired limits of 100 mr per week.

The launcher was then elevated remotely and the count down proceeded to launch. The rocket with source intact impacted at the desired range previously determined to have sufficient depth

to prevent accidental recovery and where the currents are such as to preclude the possibility of the source washing ashore.

In case of rocket malfunction causing the payload to impact in the launch area or in shallow water several recovery teams were available. Skin divers equipped with special sonar equipment and water resistant geiger counters were located off the coast in recovery vessels. Several proven recovery methods were possible. Two helicopters were available to locate and guard the area of a possible land impact until the source could be recovered. None of these recovery operations were needed since the Nike-Apache boost system operated satisfactorily.

6.0 GROWTH POTENTIAL

The experiment described in this report was the first of a series of experiments aimed at developing a technique for measuring free air density at high altitudes from high performance vehicles using an X-ray backscatter technique. This first experiment utilized a radioisotope as the source of radiation. Later tests are planned using an X-ray tube as the source of radiation.

6.1 Further Radioisotope Flights - Additional rocket flights using the radioisotope are presently being planned to further verify the technique and determine what the practical altitude limit would be. An improved source configuration is being considered using a material of higher specific activity. This new configuration is intended to reduce the self absorption within the source and increase the ratio of sensitivities of the two detectors. The strength of the source will also be increased from 25 to about 40 curies. These changes all will enable accurate density data to be obtained at higher altitudes. Additional minor modifications to the sensor design are expected to improve overall performance.

6.2 Flights Using X-Ray Tube as Source - An Air Density Sensor using an X-ray tube as a source of radiation has many advantages over such a sensor using a radioisotope source. Several of these advantages are listed below:

(1) The X-ray tube does not constitute a hazard to personnel when not in operation.

(2) Higher flux outputs can be obtained from an X-ray tube as compared with a practical radioisotope source. This has been verified with X-ray equipment at Giannini Controls Corporation. A 90 Kev commercial X-ray source operating at 5 ma peak anode current emits radiation equivalent for scattering purposes to 1000 curies of Cerium-144 (a prohibitive amount). Air density information was obtained to 200,000 feet (the limit of the altitude chamber used). By using a constant 90 KV rather than an alternating voltage, at least 10 times the radiation can be produced. By pulsing the X-ray tube, much greater emission can be obtained for short durations.

(3) An X-ray tube can be interrupted to monitor background periodically.

(4) Since the maximum energy emitted by the X-ray source is limited by the voltage on the X-ray tube, no high energy radiation is present as is the case for most radioisotopes. Therefore, lead shielding between source and detector can be limited to approximately one-eighth of an inch thickness rather than several inches greatly cutting down on system weight.

Ruggedized X-ray tubes and small rugged high voltage power supplies are presently being developed for flight environments. Further work is planned to tailor these developments into an air density sensor package for flight test in sounding rockets and high performance vehicles.

7.0 APPLICABLE DOCUMENTS

Proposal No. GSDP-255 19 February 1962
High Altitude X-Ray Air Density Measurement System
Giannini Controls Corporation.

Progress Reports #1-17 Contract Number NAS1-2306
Giannini Controls Corporation.

ER-80078 1 February 1963
Demonstration of the Gamma Scattering Air Density Sensor
Concept in the Sixty Foot Diameter Altitude Sphere
Giannini Controls Corporation.

ER-80118 19 November 1963
Air Density Sensor ADS-102 Design and Operation
Giannini Controls Corporation.

Flight Plan, Model F20-3517, October 15, 1964
X-Ray Backscatter Air Density Sensor
NASA, Langley Research Center

Test Directive for Wallops Model L2-1447
(Langley Model NIKE-APACHE F20-3751)
NASA, Wallops Station

ASD-TDR-62-880 30 November 1962
Investigation of the use of Radioisotopes for Extremely
High Altitude Measurement
Giannini Controls Corporation

FDL-TDR-64-29 1 February 1964
X-Ray Air Density Determination
Giannini Controls Corporation

APPENDIX I
STRUCTURAL AND ENVIRONMENTAL
DESIGN REQUIREMENTS

The following structural and environmental design requirements are abstracted from a NASA-Langley memorandum for Mr. Henry G. Reichle, Jr. - IRD, Sensor Development by Joseph D. Pride, Jr. - FVSD dated January 28, 1963.

"Subject: Critical Design Load Conditions for Nike-Cajun
Internal Payload Structure

1. The enclosure contains the information necessary for the contractor to initiate design of the Nike-Cajun internal payload structure. The following load conditions have been investigated and are considered the critical design conditions:

- a. Launcher condition - 200# man on nose tip + 1"G" weight distribution.
- b. Flight condition - maximum dynamic pressure ($q = 11,300\#/ft^2$) + transverse "G" - Nike burnout.
- c. Flight condition - maximum longitudinal acceleration + transverse "G" - Cajun burnout.

2. The payload airframe structure must be designed to obtain positive margins of safety for design yield loads and design ultimate loads including applicable temperature effects. The following applies:

- a. Design Limit Load = anticipated load on structure
- b. Design Yield Load = 1.15 X design limit load
- c. Design Ultimate Load = 1.50 X design limit load

3. Failure under combined loading shall be investigated considering the case of bending and compression where the following form shall apply:

$$\frac{f_b}{F_b} + \frac{f_c}{F_c} \leq 1.0$$

and

Ref. MIL-Hdbk. 5
March 1959

$$M.S. = \frac{1}{R_b + R_c} - 1$$

where:

f_b = maximum bending stress, including effects of secondary rupture

F_b = bending modulus of rupture or secondary crippling effects

f_c = axial compressive stress

F_c = allowable compressive stress

In no case shall the axial compressive stress, f_c , exceed the allowable, F_c , for a simple column.

4. A recommended flight acceptance test schedule for vibration and shock is as follows:

a. Vibration

<u>Axis</u>	<u>Frequency range cps</u>	<u>Sinusoidal</u>	<u>Acceleration amplitude g vector</u>
		<u>Sweep rate octaves/min.</u>	
Thrust	20-2000	4	5
Transverse (one axis)	20-200	4	2
Transverse (one axis)	200-2000	4	3
<u>Axis</u>	<u>Frequency bandwidth</u>	<u>Random</u>	<u>Acceleration amplitude g rms</u>
		<u>$\frac{psa}{g^2/cps}$</u>	
Thrust	20-2000	0.05	10
Transverse (one axis)	20-2000	0.025	5

b. Records - During the sinusoidal tests, the structure should be instrumented with accelerometers to monitor response and determine major resonant frequencies. All major structural resonances should be determined and recorded.

c. Shock - Along the positive thrust axis:

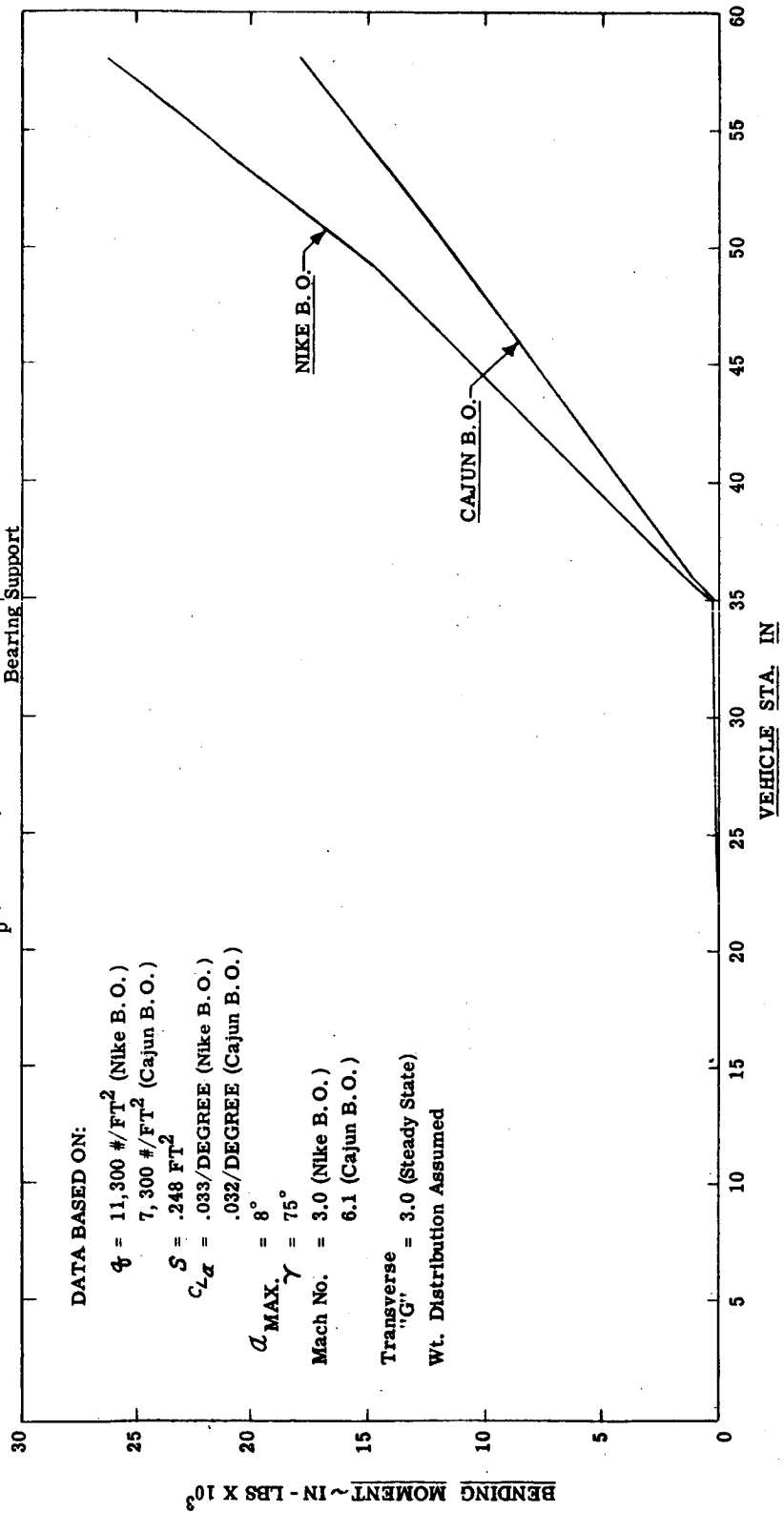
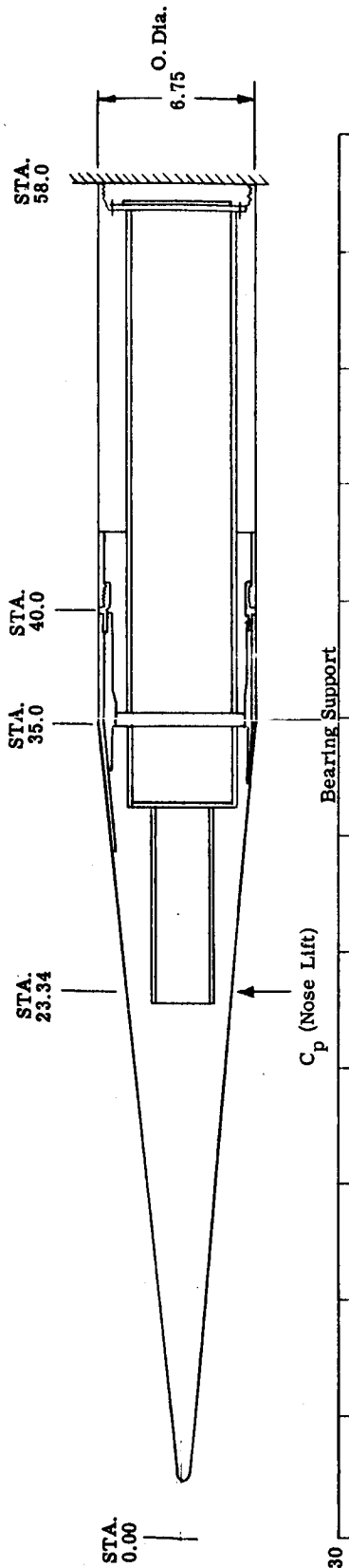
One shock at 50 g peak amplitude, half sine wave pulse shape, 8 milliseconds duration.

One shock at 30 g peak amplitude, half sine wave pulse shape, 15 milliseconds duration.

5. The internal payload structure is considered a body fixed at the Cajun headcap and cantilevered forward. The basic design ground-rules for the internal payload structure is as follows:

- a. Transverse steady state "G" = 3.0_{max} (Ref: Flight Data from TN-D-1699).
- b. Shall sustain nose lift at $\alpha = 8^\circ$ (at Nike burnout) and in combination with 3.0 "G" transverse loading.
- c. Shall be designed for longitudinal acceleration of 60 "G" and in combination with a and b above.
- d. Shall be designed for a ground handling condition of a 200# man plus 1 "G" weight distribution."

I-2. These load requirements are summarized in Figures I-1 and



CRITICAL FLIGHT CONDITIONS

FIGURE I-1

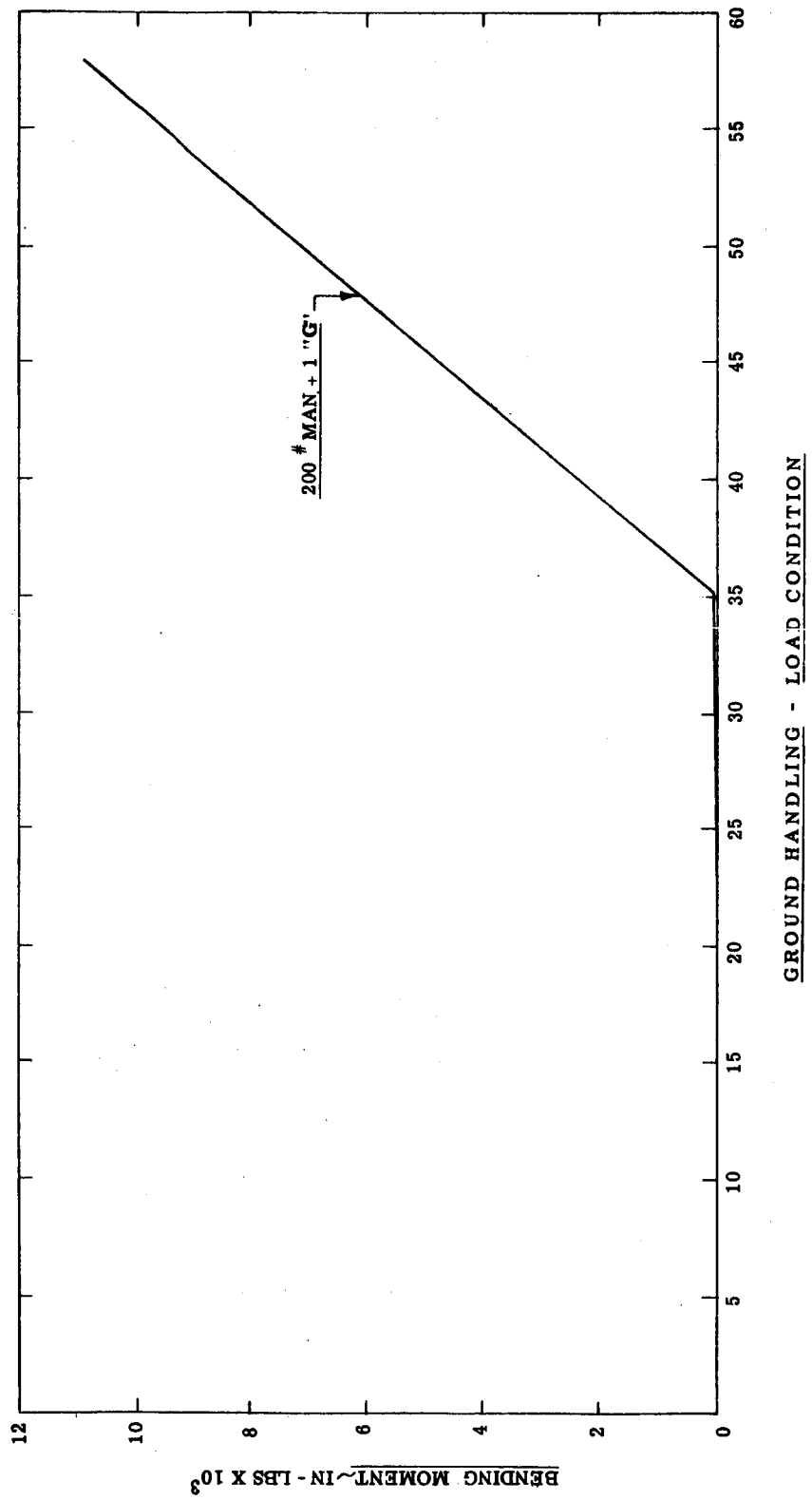
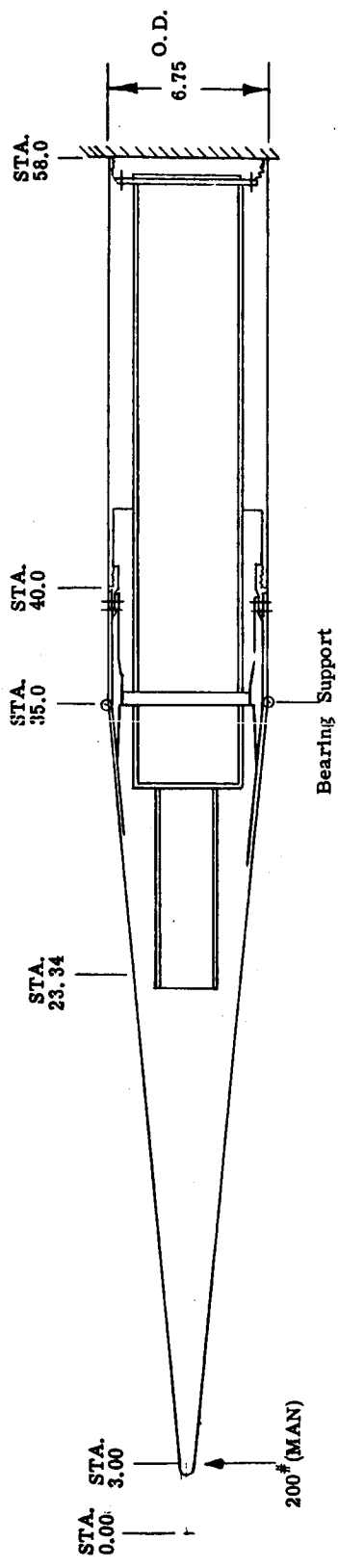


FIGURE I-2

APPENDIX II
GAMMA SCATTERING
CLASSICAL THEORY

Gamma Scattering. Gamma radiation is electromagnetic radiation of short wave length ($\sim 10^{-2}$ A) emitted by nuclei in the course of radioactive decay. Radioisotopes emit gamma radiation in one or more lines of homogeneous energy. Common gamma radioisotopes emit gammas at characteristic energies of a few Kev to several Mev.

The scattering of gamma radiation is predominately from the electrons of a material. It is most easily described by Thompson's classical theory relating the fraction of energy scattered by an electron as:

$$\frac{d\sigma_e}{d\Omega} = \frac{e^4}{32\pi^2 \epsilon_0^2 (M_0 C^2)^2} (1 + \cos^2 \theta) \quad (1)$$

Where:

$\frac{d\sigma_e}{d\Omega}$ = fraction of incident energy scattered per electron into unit solid angle, $d\Omega$, at angle θ .

e = electronic charge

M_0 = electron mass

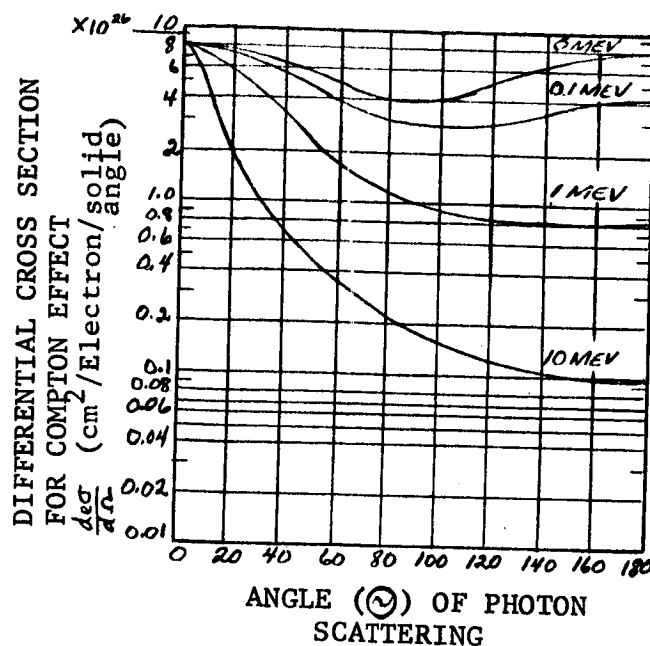
C = velocity of light.

Equation 1 is valid for very low energy gammas where the electron acquires no energy. This may not be the case, however, and equation 1 must be modified in accordance with the Klein and Nishina equations which give

$$\frac{d\sigma_e}{d\Omega} = \frac{e^4}{32\pi^2 \epsilon_0^2 (M_0 C^2)^2} \left(\frac{1}{1 + \alpha \text{vers } \theta} \right)^2 \left(1 + \cos^2 \theta + \frac{\alpha^2 \text{vers}^2 \theta}{1 + \alpha \text{vers } \theta} \right) \quad (2)$$

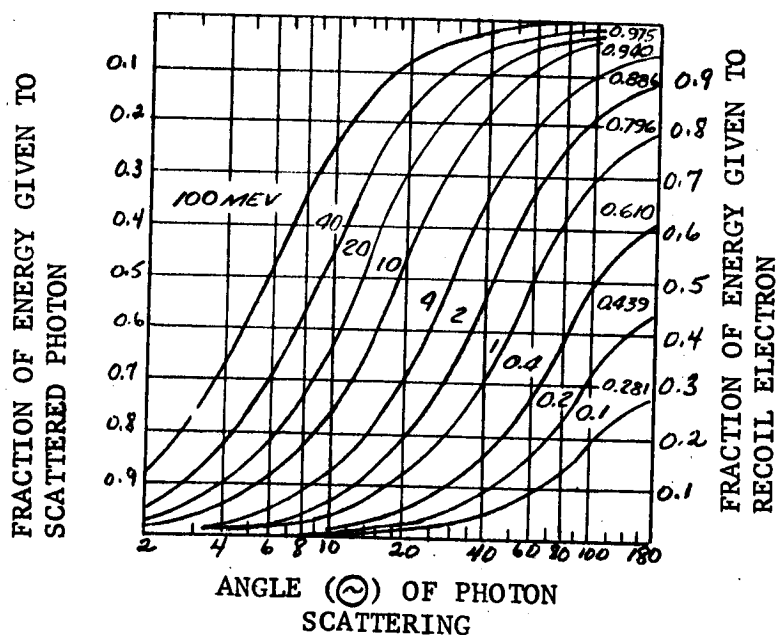
where: α = ratio of gamma energy to the energy equivalent of electron mass, $\frac{h\nu}{M_0 C^2}$

Equation 2 is plotted for various incident gamma energies in Figure II-1.



Graphs showing $d\sigma_t/d\Omega$ as a function of the angle of Photon scattering, θ , for Photon energies of 0.1, 1.0, and 10 Mev. $d\sigma_t/d\Omega$ is the differential cross section per electron per unit solid angle for the number of Photons scattered.

FIGURE II-1



Fraction of the total Photon energy given the scattered Photon (left scale) and fraction given the recoil electron (right scale) as a function of the angle of Photon scattering, θ , in a Compton collision.

FIGURE II-2

Notice that for low energy gammas the probability of an interaction resulting in a gamma backscattered, (scattered through 180°) is almost as high as for forward scattering. For a density measurement in which the majority of information results from the backscattered radiation, it is desirable to use a source of low energy gammas.

Figure II-2 illustrates the amount of energy retained by the gamma photon as a function of scattering angle and initial energy of the incident radiation. It is the low energy incident photons that tend to retain a large portion of their initial energy when scattered through large angles. 100 Kev photons retain about 70% of their initial energy when scattered through a 180° angle while 1 Mev photon only retain about 20% of their initial energy.

To show the variation of scattering with density, equation 2 must be multiplied by the number of electron per unit volume of air at density ρ .

$$d\sigma = \frac{NZ}{A} \rho d\sigma_e \quad (3)$$

where,

N = Avagadros number

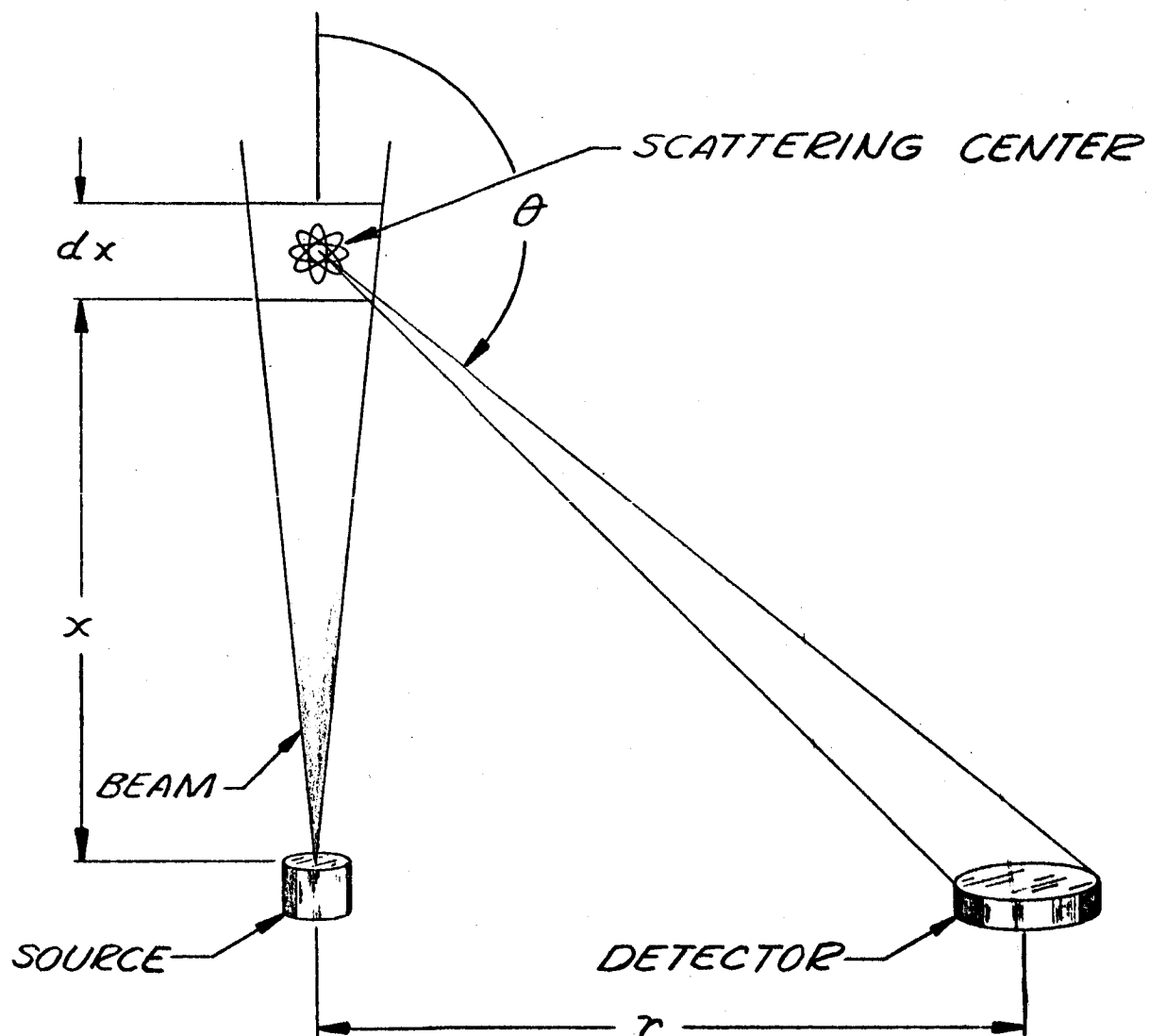
Z = Atomic number of scattering medium.

A = Atomic weight of scattering medium.

ρ = Density of scattering medium.

Equation 2 can be applied to the particular geometry considered and the number of photon scattered into a detector predicted. Referring to Figure II-3 showing the scattering geometry

$$d_n = \left(\frac{A x}{x^2 + r^2} \right)^{1/2} \quad (4)$$



SCATTERING GEOMETRY

FIGURE II-3

where

A_D = detector area

x = distance from source to the particular scattering center dx

r = source to detector separation

also:

$$\theta = \pi - \tan^{-1} \frac{r}{x} \quad (5)$$

Combining equations (2), (3), (4), and (5) and letting

$$K = \frac{e^4 NZ}{32 \pi^2 \epsilon_0^2 (M_0 C^2)^2 A} \quad (6)$$

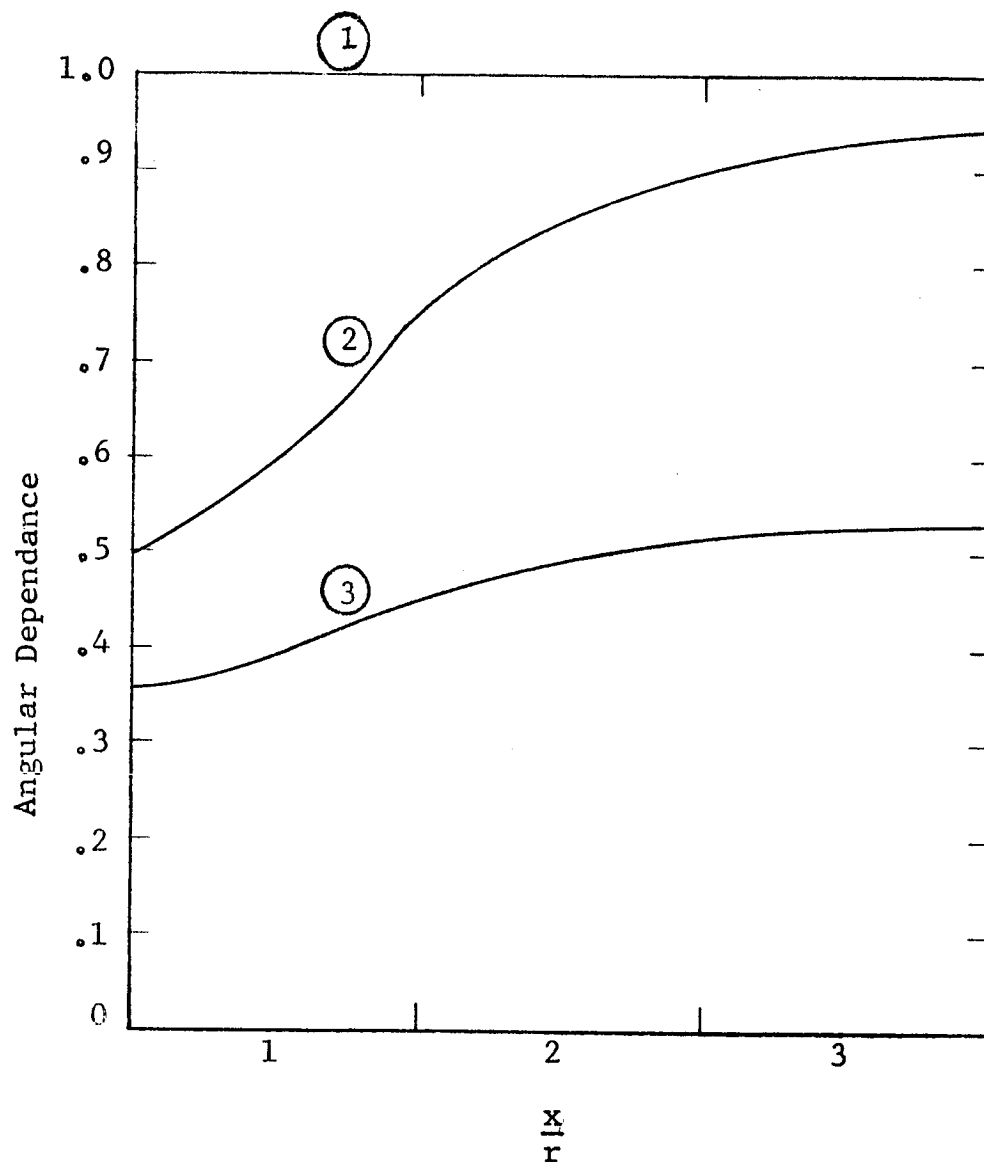
$$\frac{d\sigma}{dx} = \frac{2K\rho A_D}{r^2} \left\{ \left[\frac{x/r}{\left(\frac{x}{r}\right)^2 + 1} \right]^{3/2} \right\} \left\{ 1/2 \left(\frac{1}{1 + \alpha \text{vers } \theta} \right)^2 \left(1 + \cos \theta \frac{\alpha^2 \text{vers}^2 \theta}{1 + \alpha \text{vers } \theta} \right) \right\} \quad (7)$$

The contents of the first brace relate the differential return to the range to the scattering center; the contents of the second brace relate the differential return to the angular dependence of scattering. The angular dependence of this equation is plotted as a function of x/r in Figure II-4 for 100 Kev incident photons. Also plotted are the angular dependence curves for Thompson's classical theory, equation 1, and for the assumption that there is an equal probability of scattering occurring in any direction. The Klein and Nishina angular dependence for this particular geometry can be very simply approximated by the constant $1/2$ reducing the complexity of equation 7 significantly to:

$$\frac{d\sigma}{dx} = \frac{2K\rho A_D}{r^2} \left\{ \frac{x/r}{\left[\left(\frac{x}{r}\right)^2 + 1\right]^{3/2}} \right\} \left\{ 1/2 \right\} \quad (8)$$

Integration of equation 8 through x from zero to infinity yields:

$$\sigma = \frac{K\rho A_D}{r} \quad (9)$$



1 Equal Angular Dependence

2 Thompsons Angular Dependence $1/2 (1 + \cos^2 \sigma)$

3 Klein & Nishina Angular Dependence (100 Kev γ 's)

$$1/2 \left(\frac{1}{1 + \alpha \text{vers } \theta} \right)^2 \left(1 + \cos \theta + \alpha \frac{\text{vers}^2 \theta}{1 + \alpha \text{vers } \theta} \right)$$

Angular Dependence of Gamma Scattering

Vs

Distance to Scattering Center

FIGURE II-4

Rewriting equation 6 and evaluating K

$$K = \frac{NZ_2^2 e^4}{32A\pi^2 \epsilon_o^2 (M_o C^2)^2} \quad (10)$$

where, $N = 6.03 \times 10^{23}$ molecules per gram mole

$Z_2 = 7$ for air (Nitrogen)

$e = 4.8 \times 10^{-10}$ statcoulombs

$A = 14$ for air (Nitrogen)

$\epsilon_o = \frac{1}{4\pi}$ statcoulombs²/dyne cm²

$M_o = 9.108 \times 10^{-28}$ grams

$C = 2.998 \times 10^{10}$ cm/sec.

Thus, $K = 1.2 \times 10^{-2}$ cm²/gram

It is interesting to note that this value is very close to the scattering cross section of air as computed from the Klein and Nishina formula integrated over 4π rather than the particular geometry considered. For 100 Kev photons the cross section is 0.13 cm²/gm. Dividing this by 4π to get the probability of scattering interaction into a unit solid angle gives $\frac{0.13}{4\pi} = 1.03 \times 10^{-2}$ cm²/gm which is very close to the value of K, 1.2×10^{-2} cm²/gm. The consequence of this is that for the geometry considered the simple approximation using the equal angular probability assumption along with the total probability of a scattering event occurring results in an expression very close to one derived taking the angular distribution into account.

It is also interesting to note that for most gases the ratio of atomic number to atomic weight, $\frac{Z}{A}$, is close to the constant 1/2. Referring to equation 6 it is seen, therefore, that K is independent of the constituents of the gas. This scattering technique then gives a true measure of the gas density even through regions of variable composition.

APPENDIX III
PAYLOAD FLIGHT READINESS
TEST DATA

The following vibration and shock test data are abstracted from a NASA-Langley memorandum for RQCS files by Harold E. Poole dated November 29, 1963.

"Subject: Report of Flight Assurance Vibration and Shock Tests of the Air Density Sensor Payload, November 15, 1963

Summary

The Air Density Sensor Payload was subjected to flight assurance vibration and shock tests approximately equivalent to one flight. For the vibration tests accelerometers were mounted on the payload in order to determine transmissibility. However, due to noise from the payload transmitter, no acceleration data were taken while the transmitter was operating. A one "g" test was made with the telemetry system off in order to obtain enough data for a transmissibility plot. The highest transmissibility noted was 28.8 at 420 cps from an accelerometer mounted on the tip of the nose cone in the direction of force. The accelerometers were removed to reduce the noise level which was interfering with the shaker control system. The shock test was monitored to determine the input to the base of the payload. The shock input averaged 30g for 12 milliseconds.

At the completion of the tests, no visible evidence of failure was found. Telemetry performance monitoring was carried out by the personnel of the Telemeter Instrument Section and Giannini Controls. The project manager, Mr. Henry Reichle, stated that all systems performed satisfactorily before, during, and after the tests. Performance data taken during the test program are available from Mr. Reichle.

Introduction

The purpose of the Air Density Sensor flight is to determine the feasibility of utilizing backscattered X-rays to measure atmospheric density.

The payload consists of a radioactive source, shielding, scintillation counters, and telemetry apparatus. The vehicle will be a Nike-Apache boost system.

A prototype payload, with dummy instruments, was qualified at 150 percent of expected flight levels and twice the duration. Specific flight components were flight assurance tested at 100 percent of expected flight levels.

The flight payload, with all flight components (except the radioactive source), was then vibration and shock tested to levels that represent 100 percent of expected flight conditions. The conditions are caused mainly by the Nike (M5-E1) boost phase. Data indicate that there are no significant vibrations transmitted to the payload during the Apache boost. The specifications for the flight assurance tests were written from data taken from the "NIKE-APACHE PERFORMANCE HANDBOOK" published by GSFC.

Test Conclusions

From the test data it may be concluded that the Air Density Sensor payload passed the flight assurance vibration and shock tests without failure or malfunction of the test specimen.

AIR DENSITY SENSOR PAYLOAD FLIGHT ASSURANCE VIBRATION & SHOCK TEST

Test No.	Axis	Type Test	Level (Grms)	Frequency Limits (cps)	Test Duration (sec)	Sweep Speed (oct/min)	Data Ref. (Fig)	Remarks
1	AL	Sinusoidal	.7	20-2000	72	5.8	I	See Note 1
2			.1"DA	20-31	6		None	No failures or malfunctions noted.
3			3.5	31-2500	66			
4		Random	5	20-2000	65	NA		
5	AT	Sinusoidal	.02"DA	20-70	19	5.8	None	No failures or malfunctions noted.
6			3.5	70-2500	53			
7		Random	5	20-2000	65	NA		
8	AN	Sinusoidal	.02"DA	20-70	19	5.8	None	No failures or malfunctions noted.
9			3.5	70-2500	53			
10		Random	5	20-2000	65	NA		
11	AL	Shock	21.2	NA	11ms	NA	II	Input to base of payload was 30.2 g at 12 ms. No failures or malfunctions noted.

NOTE 1: Noise appeared in the vibration control system due to payload transmitter feeding into accelerometer cables. Decided to make Test No. 1 without the transmitter on in order to obtain transmissibility data. Removed all monitor accelerometers after Test No. 1 to eliminate noise.

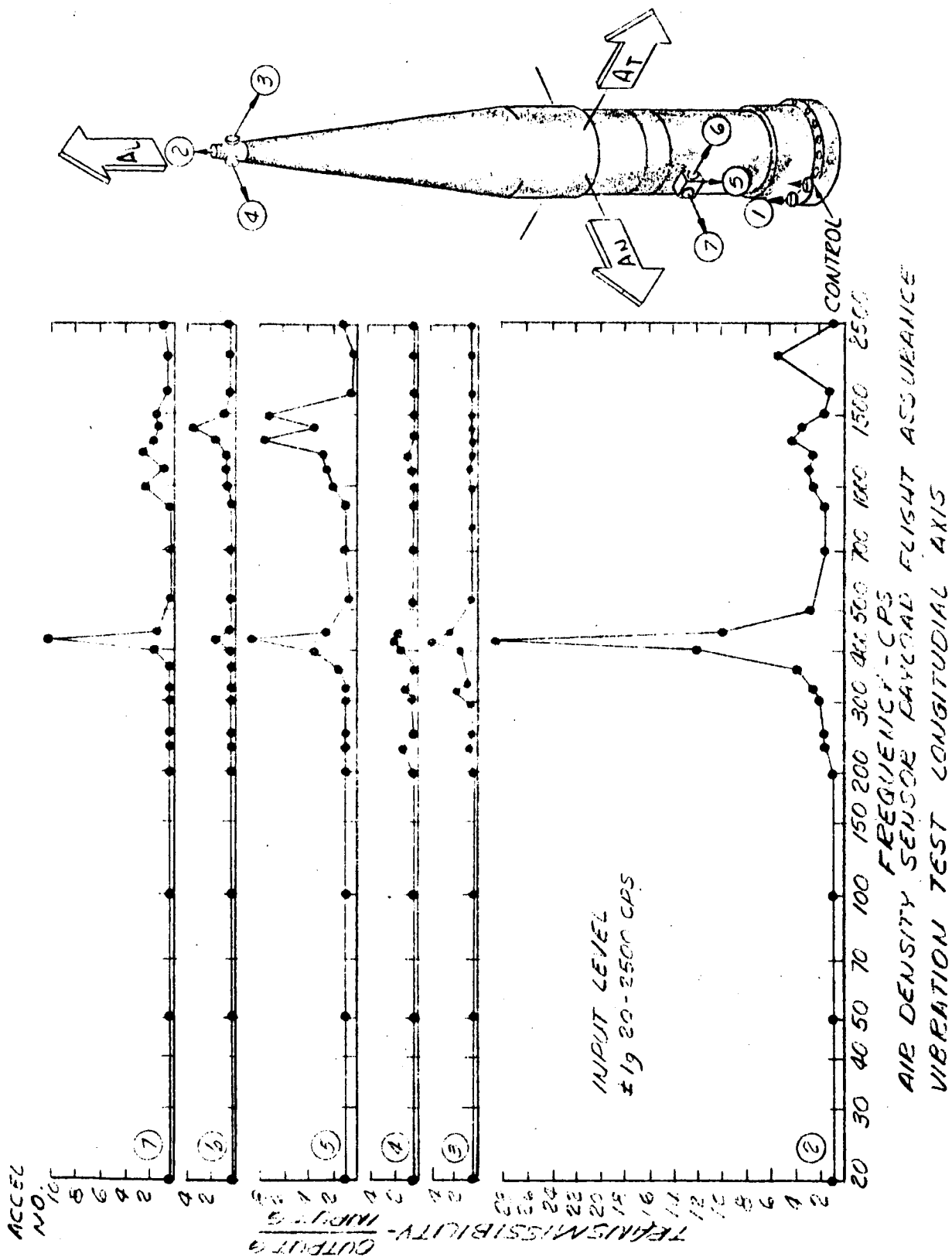
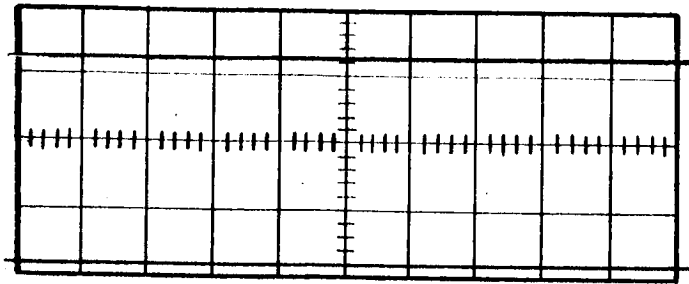
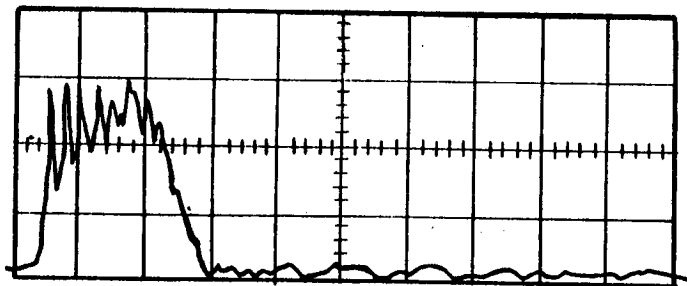


Figure III-1



CALIBRATE SIGNAL
37.039 2.45/DIVISION




SHOCK SIGNAL
1 MS/DIVISION


FLIGHT ASSURANCE SHOCK TEST

FIGURE III-2


APPENDIX IV
FLIGHT DATA

		NAME	DATE	TEST DATA A			PAGE 1 OF 6	
OPERATOR		12/17/63		SUBJECT AIR DENSITY SENSOR ADS-102			TEST NO.	
ASST. OPER				ORIGINAL 1 SECOND DATA			SPEC. NO.	
DATA:								
ELAPSED TIME SEC	CH. E	CH. C	CH. 14	ALT. K FT.	ALT. K FT.			
8			769	17.4				
9			701	19.7	18.5			
10			657	21.9	20.8			
11			631	24.0	22.9			
12			592	26.1	25.0			
13			564	28.0	27.0			
14			556	29.9	28.9			
15			516	31.7	30.8			
16			492	33.4	32.3			
17			466	35.1	34.2			
18			440	36.7	35.9			
19			422	38.3	37.5			
20			395	39.8	39.0			
21			366	41.2	40.5			
22			344	42.7	41.9			
23			321	44.0	43.3			
24			330	45.7	44.8			
25			272	47.9	46.8			
26			227	50.7	49.3			
27	2156		186	54.0	52.3			
28	2274		148	57.8	55.9			
29	2200		130	62.2	60.0			
30	1929		104	67.1	64.6			
31	1657		193	71.9	69.5			
32	1312		86	76.7	74.3			
33	1101		81	81.4	79.0			
34	902		73	86.1	83.7			
35	732		66	90.7	88.3			
REMARKS:								




		NAME	DATE	TEST DATA A			PAGE 2 OF 6	
OPERATOR		12/17/63		SUBJECT AIR DENSITY SENSOR ADS-102			TEST NO.	
ASST. OPER				ORIGINAL 1 SECOND DATA			SPEC. NO.	
DATA:								
ELAPSED TIME SEC	CH. E	CH. C	CH. 14	ALT. K FT.	ALT. K FT.			
36	694		62	94.7	92.7			
37	541		69	99.3	97.0			
38	472		57	103.8	101.5			
39	420		52	108.3	106.0			
40	368		46	112.7	110.5			
41	307		45	117.1	114.9			
42	275		40	121.5	119.3			
43	279		41	125.8	123.6			
44	251		34	130.1	127.9			
45	232		36	134.4	132.2			
46	210		33	138.6	136.5			
47	292		32	142.8	140.7			
48	188		33	147.0	144.9			
49	185		30	151.2	149.1			
50	174		30	155.3	153.2			
51	178		35	159.3	157.3			
52	170		28	163.4	161.3			
53	171		26	167.4	165.4			
54	156		39	171.4	169.4			
55	155		39	175.3	173.3			
56	154		35	179.2	177.2			
57	151		28	183.1	181.1			
58	169		26	187.0	185.0			
59	148		32	190.8	188.9			
60	157		27	194.6	192.7			
61	154		10	198.3	196.4			
62	157	113	1	202.0	200.1			
63	148	111	1	205.7	203.8			
64	158	104	1	209.4	207.5			
REMARKS:								
<div style="text-align: right;">  </div>								

		NAME	DATE	TEST DATA A			PAGE 3 OF 6	
OPERATOR			12/17/63	SUBJECT AIR DENSITY SENSOR ADS-102 ORIGINAL 1 SECOND DATA			TEST NO.	
ASST. OPER.							SPEC. NO.	
DATA:								
ELAPSED TIME SEC	CH. E	CH. C	CH. 14	ALT. K FT.	ALT. K FT.			
65	146	112	1	213.0	211.2			
66	152	105	1	216.6	214.8			
67	146	108	1	220.3	218.4			
68	158	195	2	223.7	222.0			
69	147	104	1	227.2	225.4			
70	145	108	1	230.7	228.9			
71	156	110	1	234.2	232.4			
72	153	103	1	237.6	235.9			
73	143	104	1	240.9	239.2			
74	147	113	1	244.3	242.6			
75	141	113	1	247.6	245.9			
76	134	119	0	250.9	249.2			
77	144	119	1	254.2	252.5			
78	152	112	1	257.4	256.8			
79	142	120	1	260.6	259.0			
80	144	102	1	263.7	262.1			
81	147	104	1	266.9	265.3			
82	148	109	1	270.0	268.4			
83	140	106	1	273.0	271.5			
84	134	108	0	276.1	274.5			
85	142	109	1	279.1	277.6			
86	140	119	1	282.1	280.6			
87	137	103	1	285.0	283.5			
88	159	105	1	287.9	286.4			
89	146	103	1	290.8	289.3			
90	137	105	0	293.7	292.2			
91	141	107	1	296.5	295.1			
92	134	110	1	299.3	297.9			
93	141	107	1	302.0	300.6			
REMARKS:								



		NAME	DATE	TEST DATA A			PAGE 4 OF 6	
OPERATOR			12/17/63	SUBJECT	AIR DENSITY SENSOR ADS-102 ORIGINAL 1 SECOND DATA			TEST NO.
ASST. OPER.								SPEC. NO.
DATA:								
ELAPSED TIME SEC	CH. E	CH. C	CH. 14	ALT. K FT.	ALT. K FT.			
268	149	117	1	311.4				
269	132	108	1	308.8	310.1			
270	144	117	1	306.1	307.5			
271	133	110	1	303.4	304.8			
272	136	110	1	300.6	302.0			
273	142	101	1	297.8	299.2			
274	159	108	1	295.0	296.4			
275	145	111	1	292.2	293.6			
276	134	106	0	289.3	290.7			
277	146	101	1	286.4	287.8			
278	140	105	1	283.4	284.9			
279	140	105	1	280.5	281.9			
280	143	196	1	277.5	279.0			
281	146	106	1	274.4	275.9			
282	145	101	0	271.4	272.9			
283	147	105	1	268.3	269.8			
284	145	113	3	265.2	266.7			
285	134	102	1	262.0	263.6			
286	142	104	1	258.8	260.4			
287	136	103	1	255.6	257.2			
288	145	108	1	252.3	253.9			
289	148	196	1	249.0	250.6			
290	144	196	1	245.7	247.3			
291	124	106	1	242.4	244.0			
292	143	107	1	239.0	240.7			
293	138	112	1	235.6	237.3			
294	138	129	0	232.2	233.9			
295	148	110	0	228.7	230.4			
REMARKS:								




	NAME	DATE	TEST DATA A			PAGE 5 OF 6	
OPERATOR		12/17/63	SUBJECT AIR DENSITY SENSOR ADS-102			TEST NO.	
ASST. OPER			ORIGINAL 1 SECOND DATA			SPEC. NO.	

DATA:								
ELAPSED TIME SEC	CH. E	CH. C	CH. 14	ALT. K FT.	ALT. K FT.			
296	134	112	1	225.2	226.9			
297	161	106	1	221.7	223.4			
298	138	107	1	218.1	219.9			
299	148	108	1	214.6	216.3			
300	138	121	1	210.9	212.7			
301	153	112	1	207.3	209.1			
302	162	122	1	203.4	205.3			
303	159	119	1	199.9	201.6			
304	148	123	1	196.2	198.1			
305	152	122	1	192.4	194.3			
306	159	111	0	188.6	190.5			
307	179	123	1	184.8	186.7			
308	154	139	2	181.0	182.9			
309	156	135	1	177.1	179.0			
310	158	136	1	173.2	175.1			
311	173	132	3	169.2	171.2			
312	175	138	2	165.3	167.2			
313	163	144	1	161.4	163.3			
314	182	154	1	157.4	159.4			
315	186	172	3	153.4	155.4			
316	183	166	2	149.3	151.3			
317	293	184	1	145.2	147.2			
318	205	205	2	141.2	143.2			
319	229	239	2	137.0	139.1			
320	227	233	2	132.9	134.9			
321	231	256	2	128.8	130.8			
322	255	393	3	124.6	126.7			
323	267	325	3	120.4	122.6			
324	300	498	3	116.1	118.2			

REMARKS:

Giannini

[illegible]

		NAME	DATE	TEST DATA B				PAGE 1 OF 6	
OPERATOR			12/17/63	SUBJECT				TEST NO.	
ASST. OPER				AIR DENSITY SENSOR ADS-102 1 SECOND DATA LESS BG.				SPEC. NO.	
DATA:									
ELAPSED TIME SEC	DET. 2	DET. 1	DET. 1	DET. 2 -570	DET. 1 -440	DET. 1 -440	ALT. K FT	DET. 1 + 2	
8									
9							18.5		
10							20.8		
11							22.9		
12							25.0		
13							27.0		
14							28.9		
15							30.8		
16							32.3		
17							34.2		
18							35.9		
19							37.5		
20							39.0		
21							40.5		
22							41.9		
23							43.3		
24							44.8		
25							46.8		
26							49.3		
27	8620			8050			52.3		
28	9096			8526			55.9		
29	8800			8230			60.8		
30	7716			7016			64.6		
31	6628			6058			69.5		
32	5248			4678			74.3		
33	4404			3834			79.0		
34	3608			3038			83.7		
35	2928			2358			88.3		
REMARKS:									
<div style="text-align: right; margin-top: 100px;">  </div>									


	NAME	DATE	TEST DATA B				PAGE 2 OF 6
OPERATOR		12/17/63	SUBJECT AIR DENSITY SENSOR ADS-102				TEST NO.
ASST. OPER			1 SECOND DATA LESS BG.				SPEC. NO.

DATA:								
ELAPSED TIME SEC	DET. 2	DET. 1	DET. 1	DET. 2	DET. 1	DET. 1	ALT. K FT.	DET. 1 + 2
36	2776			2206			92.7	
37	2164			1594			97.0	
38	1888			1318			101.5	
39	1680			1110			106.0	
40	1472			900			110.5	
41	1228			658			114.9	
42	1100			530			117.3	
43	1116			546			123.6	
44	1004			434			127.9	
45	928			358			132.2	
46	840			270			136.5	
47				200			140.7	
48	742			172			144.9	
49	740			170			149.1	
50	696			126			153.2	
51	712			142			157.3	
52	680			110			161.3	
53	684			114			165.4	
54	624			94			169.4	
55	620			90			173.3	
56	616			46			177.2	
57	604			34			181.1	
58	676			106			185.0	
59	592			22			188.9	
60	628			58			192.7	
61	616			46			196.4	
62	628	452		58	22		200.1	
63	592	444		22	14		203.8	
64	632	416		62	-14		207.5	

REMARKS:

Giannini

		NAME	DATE	TEST DATA B			PAGE 3 OF 6	
OPERATOR		2/17/63		SUBJECT AIR DENSITY SENSOR ADS-102 1 SECOND DATA LESS BG.			TEST NO.	
ASST. OPER.							SPEC. NO.	
DATA:								
ELAPSED TIME SEC	DET. 2	DET. 1	DET. 1	DET. 2	DET. 1	DET. 1	ALT. K FT.	DET. 1 + 2
				-570	-440	-440		
65	584	448	512	14	18		211.2	
66	608	420	512	38	-10		214.8	
67	584	432	512	14	2		218.4	
68	632	780	1028	62	0		222.0	
69	588	416	512	18	-14		225.4	
70	580	432	512	10	2		228.9	
71	624	440	512	54	0		232.4	
72	612	412	512	42	-18		235.9	
73	572	416	512	2	-14		239.2	
74	588	452	512	18	22		242.6	
75	564	452	512	-6	22		245.9	
76	536	476	0	-34	46		249.2	
77	576	476	512	6	46		252.5	
78	608	448	512	38	18		256.8	
79	568	480	512	-2	50		259.0	
80	576	432	512	6	2		262.1	
81	588	416	512	18	-14		265.3	
82	592	436	512	22	6		268.4	
83	560	424	512	-10	-6		271.5	
84	536	432	0	34	2		274.5	
85	568	436	512	-2	6		277.6	
86	560	476	512	-10	46		280.6	
87	548	412	512	22	-18		283.5	
88	636	420	512	66	-10		286.4	
89	584	412	512	14	-28		289.3	
90	548	420	0	-22	-10		292.2	
91	564	428	512	-6	-2		295.1	
92	536	440	512	-34	+10		297.9	
93	564	428	512	-6	-2		300.6	
REMARKS: 20 11380 8796 8704 569 439.8 435.2								



NAME		DATE	TEST DATA B				PAGE 4 OF 6	
OPERATOR	12/17/63		SUBJECT AIR DENSITY SENSOR ADS-102				TEST NO.	
ASST. OPER			1 SECOND DATA LESS BG.				SPEC. NO.	

DATA:								
ELAPSED TIME	DET. 2	DET. 1	DET. 1	DET. 2	DET. 1	DET. 1	ALT.	DET. 1 + 2
SEC				-570	-440	-440	K FT.	
268	596	468	512	26	38			
269	528	432	512	-42	2		310.1	
270	576	468	512	6	38		307.5	
271	532	440	512	-38	10		304.8	
272	544	440	512	-26	10		302.0	
273	568	404	512	-2	26		299.2	
274	636	432	512	66	2		296.4	
275	580	444	512	10	14		293.6	
276	536	424	0	-34	-6		290.7	
277	584	404	512	14	-26		287.8	
278	560	420	512	-10	-10		284.9	
279	560	420	512	-10	-10		281.9	
280	572		512	2	0		279.0	
281	584	424	512	14	-6		275.9	
282	580	404	0	10	-26		272.9	
283	588	420	512	18	-10		269.8	
284	580	452	1536	10	22		266.7	
285	536	408	512	-34	-22		263.6	
286	568	416	512	-2	-14		260.4	
287	544	412	512	-26	-18		257.2	
288	580	432	512	10	2		253.9	
289	592		512	22	0		250.6	
290	576		512	6	0		247.3	
291	496	424	512	-74	-6		244.0	
292	572	428	512	2	-2		240.7	
293	552	448	512	-18	18		237.3	
294	552	516	0	-18	86		233.9	
295	592	440	0	22	10		230.4	

REMARKS:


2) 11392 8516
569.6 425.8 435.2
569 439.8
2) 11386 8656
569.3 432.8

Giannini

		NAME	DATE	TEST DATA B				PAGE 5 OF 6	
OPERATOR		12/17/63		SUBJECT AIR DENSITY SENSOR ADS-102 1 SECOND DATA LESS BG.				TEST NO.	
ASST. OPER								SPEC. NO.	
DATA:									
ELAPSED TIME SEC	DET. 2	DET. 1	DET. 1	DET. 2 -570	DET. 1 -440	DET. 1 -440	ALT. K FT.	DET. 1 + 2	
296	536	448	512	-34✓	18		226.9		
297	644	424	512	74✓	-6		223.4		
298	552	428	512	-18✓	-2		219.9		
299	592	432	512	22✓	2		216.3		
300	552	484	512	-18✓	54		212.7		
301	612	448	512	42	18		209.1		
302	648	488	512	78	58		205.3		
303	636	476	512	66	46		201.6		
304	592	492	512	22	62		198.1		
305	608	498	512	38	58		194.3		
306	636	444	0	66	14		190.5		
307	716	492	512	146	62	82	186.7		
308	616	556	1024	46	126	594	182.9		
309	624	640	512	54	210	82	179.0		
310	632	544	512	62	114	82	175.1		
311	692	528	1536	122	98	1106	171.2		
312	700	552	1024	130	122	594	167.2		
313	652	576	512	82	146	82	163.3		
314	728	616	512	158	186	82	159.4		
315	744	688	1536	174	258	1106	155.4		
316	732	664	1024	162	234	594	151.3	396	
317		736	512	200	306	82	147.2	506	
318	820	820	1024	250	390	594	143.2	540	
319	916	956	1024	346	526	594	139.1	872	
320	908	932	1024	338	502	594	134.9	840	
321	924	1024	1024	354	594	594	130.8	948	
322	1020	1572	1536	450	1142	1106	126.7	1592	
323	1068	1300	1536	498	870	1106	122.6	1368	
324	1200	1992	1536	630	1562	1106	118.2	2192	
REMARKS:									
3402 6364									
<div style="text-align: right; border: 1px solid black; padding: 5px; display: inline-block;"> Giannini </div>									


[illegible]

		NAME	DATE	TEST DATA C			PAGE 1 OF 5	
OPERATOR		12/17/63		SUBJECT AIR DENSITY SENSOR ADS-102 10 SECOND DATA LESS BG.			TEST NO.	
ASST. OPER							SPEC. NO.	
DATA:								
ELAPSED TIME	DET. 2	DET. 1	DET. 1	ALT. K FT.	ALT. K FT.	DET. 1 + 2		
36	53994			94.7	69.5			
37	47538			99.3	74.3			
38	40330			103.8	79.0			
39	33210			108.3	83.7			
40	27094			112.7	88.3			
41	21694			117.1	94.7			
42	17546			121.5	99.3			
43	14258			125.8	103.8			
44	11654			130.1	108.3			
45	9594			134.4	112.7			
46	7718			138.6	117.1			
47	6394			142.8	121.5			
48	5248			147.0	125.8			
49	4308			151.2	130.1			
50	3534			155.3	134.4			
51	3018			159.3	138.6			
52	2598			163.4	142.8			
53	2166			167.4	147.0			
54	1826			171.4	151.2			
55	1558			175.4	155.3			
56	1334			179.2	159.3			
57	1098			183.1	163.4			
58	1032			187.0	167.4			
59	884			190.8	171.4			
60	816			194.6	175.3			
61	720			198.3	179.2			
62	668			202.0	183.1			
63	576			205.7	187.0			
64	544			209.4	190.8			
REMARKS:								




GCC-1F-4

		NAME	DATE	TEST DATA C			PAGE 2 OF 5	
OPERATOR			12/17/63	SUBJECT AIR DENSITY SENSOR ADS-102 10 SECOND DATA LESS BG.			TEST NO.	
ASST. OPER							SPEC. NO.	
DATA:								
ELAPSED TIME	DET. 2	DET. 1	DET. 1	ALT. K FT.	ALT. K FT.	DET. 1 + 2		
65	468			213	194.6			
66	460			216.6	198.3			
67	440			220.3	202.0			
68	396			223.7	205.7			
69	392			227.2	209.4			
70	344			230.7	213			
71	352		20	234.2	216.6			
72	336		-20	237.6	220.3			
73	316		-48	240.9	223.7			
74	272		-12	244.3	227.2			
75	252		-8	247.6	230.7			
76	180		42	250.9	234.2			
77	172		72	254.2	237.6			
78	148		110	257.4	240.9			
79	128		174	260.6	244.3			
80	124		174	263.7	247.6			
81	88		160	266.9	250.9			
82	68		184	270	254.2			
83	56		192	273	257.4			
84	72		172	276.1	260.6			
85	76		156	279.1	263.7			
86	100		156	282.1	266.9			
87	84		92	285.0	270			
88	152		64	287.9	273			
89	160		-14	290.8	276.1			
90	120		-26	293.7	279.1			
91	92		-14	296.5	282.1			
92	68		-10	299.3	285			
93	28		-6	302.0	287.9			
REMARKS:								




GCC-17-4

		NAME	DATE	TEST DATA ^C			PAGE 3 OF 5	
OPERATOR			12/17/63	SUBJECT AIR DENSITY SENSOR ADS-102			TEST NO.	
ASST. OPER				10 SECOND DATA LESS BG.			SPEC. NO.	
DATA:								
ELAPSED TIME	DET. 2	DET. 1	DET. 1	ALT. K Ft.	ALT. K FT.	DET. 1 + 2		
268								
269								
270								
271								
272								
273								
274								
275								
276								
277	-20	108			302	88		
278	-56	60			299.2	16		
279	-24	48			296.4	24		
280	-28	10			293.6	-18		
281	24	-6			290.7	18		
282	60	-42			287.8	22		
283	80	-78			284.9	2		
284	24	-58			281.9	-34		
285	-20	-94			279	-74		
286	12	-102			275.9	-90		
287	-28	-94			272.9	-122		
288	8	-82			269.8	-74		
289	24	-72			266.7	-48		
290	28	-72			263.6	-44		
291	-60	-72			260.4	-132		
292	-68	-48			257.2	-116		
293	-104	-20			253.9	-124		
294	-132	44			250.6	-176		
295	-156	76			247.3	-80		
REMARKS:								



		NAME	DATE	TEST DATA C			PAGE 4 OF 5	
OPERATOR			12/17/63	SUBJECT AIR DENSITY SENSOR ADS-102			TEST NO.	
ASST. OPER				10 SECOND DATA LESS BG.			SPEC. NO.	
DATA:								
ELAPSED TIME	DET. 2	DET. 1	DET. 1	ALT. K FT.	ALT. K FT.	DET. 1 + 2		
296	-108	108			244.0	0		
297	-8	120			240.7	112		
298	-36	120			237.3	84		
299	-36	122			233.9	86		
300	-60	176			230.4	116		
301	56	236			226.9	256		
302	132	256			223.4	392		
303	216	284			219.9	504		
304	256	260			216.3	520		
305	272	308			212.7	580		
306	372	301			209.1	673		
307	444	369			205.3	813		
308	508	477			201.6	1005		
309	540	705			198.1	1247		
310	620	765			194.3	1385		
311	700	845			190.5	1545		
312	752	909			186.7	1661		
313	768	1009			182.9	1777		
314	904	1133			179.0	2037		
315	1040	1333			175.1	2373		
316	1136	1553	4404		171.2	2689		
317	1190	1797	4404		167.2	2987		
318	1394	2061	4404		163.3	3455		
319	1686	2377	4916		159.4	4063		
320	1962	2765	5428		155.4	4727		
321	2194	3261	4916		151.3	5455		
322	2774	4281	5428		147.2	7055		
323	3190	5005	6452		143.2	8195		
324	3652	6381	7476		139.1	10043		
REMARKS:								



DCC-1F-4

